# Optimisation of the selection capability of the H1 Fast Track Trigger

**Diplomarbeit**

**Kristin Lohwasser**
**Fachbereich Physik**

**Universität Dortmund**

**July 2006**

# Optimisation of the selection capability of the H1 Fast Track Trigger

**Diplomarbeit**

**Kristin Lohwasser**
**Fachbereich Physik**

**Universität Dortmund**

**July 2006**

# Abstract

The Fast Track Trigger (FTT) uses information from the central jet chambers of the H1 experiment to reconstruct track parameters. Its purpose is to contribute to the online selection of events on three levels within the H1 multi-stage trigger system. In this thesis a general analysis of the resolution of the track parameters obtained on the second trigger level is presented. These resolutions yield 4.11±0.01 mrad for $\phi$, 118.7±0.2 mrad for $\theta$ and 3.968±0.002% for $\kappa$ relative to the resolution achieved in the offline reconstruction. Furthermore the selection capability of the FTT with regard to events with $D^*$ mesons is investigated on all three trigger levels. These studies cover the kinematic regions of deep inelastic scattering ($2 < Q^2 < 100\text{GeV}^2$) and photoproduction ($Q^2 \approx 0$).

# Contents

# 1 Introduction

The object of particle physics is to explain the fundamental properties of nature and to derive a model, which describes consistently and comprehensively the development of our cosmos from its beginning down to the present day as well as the existence of the smallest to the largest structures. The approach which up to now satisfies these requirements best is the **s**tandard **m**odel (**SM**) [1], which identifies the building blocks of nature to be excitations of quantum fields [2]. It traces the various macroscopic phenomena back to interactions between twelve different fundamental particles, six quarks and six leptons, and their respective antiparticles. All of them are grouped into three generations or families of fermions, spin 1/2 particles [3] (see fig. 1.1). They interact via the exchange of gauge bosons, which have spin 1. These are divided into four subgroups, namely the gauge boson of the electromagnetic force, the photon $\gamma$, those of the weak force, $Z^0$, $W^+$ and $W^-$, as well as the gauge bosons of the strong force, the gluons [4]. Still unproven is the existence of the gravitino, the potential carrier of the fourth fundamental force, the gravitation force. The electromagnetic and the weak force can be unified in the framework of electroweak theory. This theory postulates the existence of another electroweak boson, the Higgs boson. It is supposedly responsible for the origin of particle masses and for electroweak symmetry breaking, i.e. its existence explains why the electroweak force falls apart into electromagnetic and weak force at lower energies. The Higgs boson has, however, not been found yet, but it is hoped to be detected at the **L**arge **H**ardon **C**ollider (**LHC**), which is to start its operation in 2007.

The quantum field theories which underpin the standard model are the gauge theory of **q**uantum **e**lectro**d**ynamics (**QED**) for the electromagnetic interactions, **q**uantum **c**hromo**d**ynamics (**QCD**) describing the strong interaction and **q**uantum **f**lavour **d**ynamics (**QFD**) for the weak interactions. In the framework of the Glashow-Weinberg-Salam model, electromagnetic and weak interactions can be unified in the gauge theory of electroweak interactions.

The standard model was developed mainly with the help of $e^+e^-$ annihilation as well as hadron scattering experiments. The former offer the possibility of measuring the characteristics of elementary particles and their interactions in a very clean environment with unambiguous signals and high presicion, the latter exhibit higher centre of mass energies and thus serve as discovery machines. Either way, they investigate the number of particles and the couplings of the different interactions as well as the properties of bound states of quarks, baryon and meson. These bound states follow a common symmetry which was first described at the beginning of the sixties by Gell-Mann [5], [6], who grouped the baryons and mesons in decuplets and octets respectively. Almost at the same time, the **q**uark **p**arton **m**odel (**QPM**) emerged. First introduced in 1969 [7], it took another point of view and focused on the the dynamical behaviour of the bound states by describing hadron scattering as the scattering of partons, i.e. pointlike particles forming a bound state. Today, scattering experiments cast a light on the compositeness of the proton.

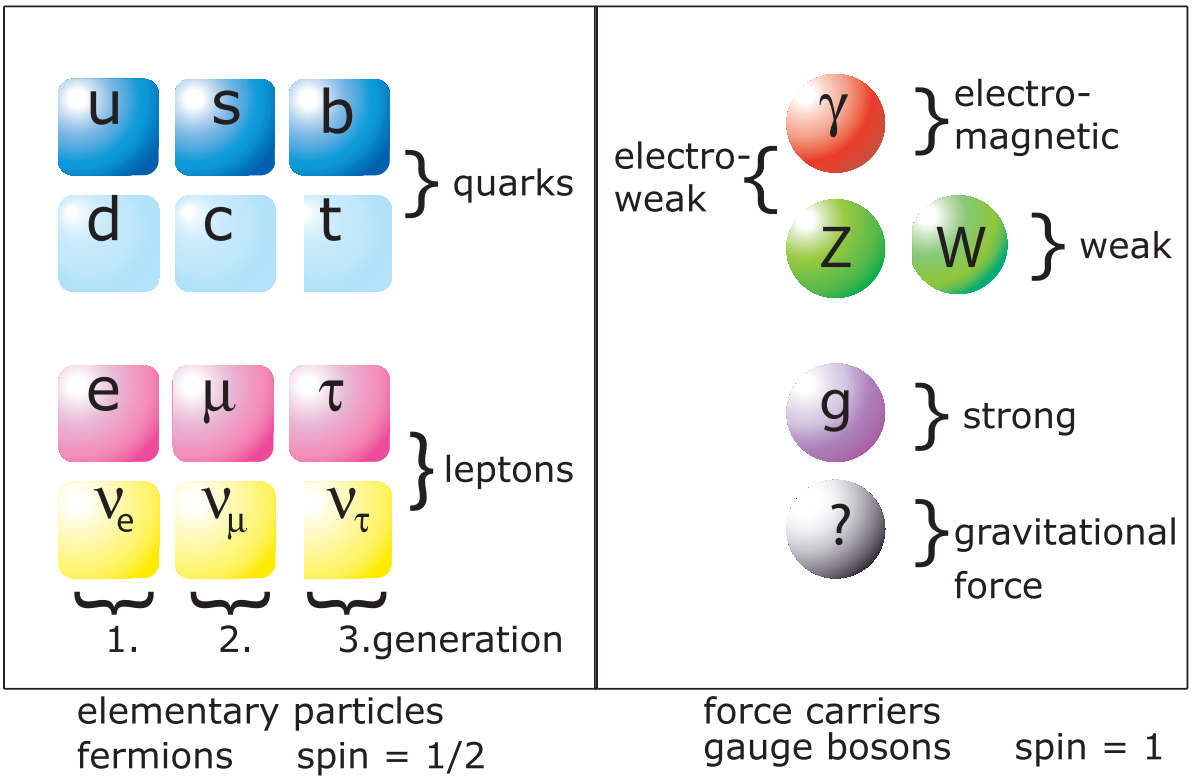


Figure 1.1: The standard model describes the building blocks of nature in terms of fundamental interactions between fundamental particles.

One of the accelerators used to probe the structure of the proton is the **H**adron **E**lektron **R**ing **A**nlage (**HERA**) in Hamburg, where the H1 Experiment is built around one of the interaction regions. HERA collides protons and electron or positrons[1]. The outcome of these scatterings are then analysed making use of two complementary strategies, the first one being inclusive measurements, where the cross section[2] is measured depending on kinematic variables only, but regardless of the final state. The other strategy is to measure exclusive or semi-inclusive cross sections, which means that only certain types of final states are taken into account in the analysis. An example of processes, which are investigated in semi-inclusive analysis, is the production of heavy mesons, bound states of a quark-antiquark pair, whose production mechanism is sensitive to the gluon density of the proton as well as to properties of fragmentation, the process of the transition of free quarks into bound states.

It is very crucial for later analysis to make sure, that during data acquisition interesting processes, such as the production of heavy mesons, are selected for recording and storage, even though they might be hard to distinguish from background in the time available during data taking. A part of the subsystems of the H1 detector is dedicated to deliver fast signals, which trigger the readout of the detector, as will be explained in detail later on. This trigger system employs selection mechanisms, that have to be on one hand effi-

[1] Henceforth, when not stated otherwise, only the term electrons is used for both, electrons and positrons.
[2] A cross section $\sigma$ is a normalised measure that expresses the probability of a certain process. It is defined as $\sigma \sim \frac{N_{events}}{\mathcal{L}}$ and is process dependent.

cient while on the other hand they also have to be very selective in order to reduce the readout rate of the detector. It is designed as multi-level trigger system with an increasing decision time, but with decreasing capability regarding the maximal input rate. The aim is to restrict data taking on genuine electron proton scattering events, while rejecting background events such as beam-gas interactions.

## 1.1 The aim of this thesis

In this thesis a detailed study of trigger mechanism to select processes where a charged $D^*$ meson is produced and detected via its decay into a $D^0$ and a low momentum pion[3] and the subsequent decay of the $D^0$ meson into a kaon and a pion ($D^{*\pm} \to D^0\pi^{\pm}_{slow} \to K^{\mp}\pi^{\pm}\pi^{\pm}_{slow}$) mesons in the final state in different kinematic regions at the H1 Experiment is presented. This decay channel has the advantage of having three charged particles in the final state, easing the full reconstruction of the $D^*$ meson as well as the benefit of the small mass difference between the $D^*$ and the $D^0$ meson, restricting the phase space for the slow pion and allowing the usage of this mass difference for the reconstruction of a very clear signal. However, on trigger level it is difficult to distinguish the production of heavy from light mesons, where the latter have to be suppressed due to rate limitations in the data acquisition.

All of the analysed trigger mechanisms to select $D^*$ mesons make use of the newly commissionened **F**ast **T**rack **T**rigger (**FTT**), which delivers track information based on data from the central drift chambers of the experiment to the first three levels of the H1 trigger system. Presented herein are findings on the general performance of the FTT in terms of track resolutions of the Level 2 system and its stability throughout the data taking periods 2005 and 2006. Also, the performance of the FTT relevant for the selection of $D^*$ mesons is investigated, results on rate reductions and selection efficiencies are presented. Both, the kinematic regime of deep inelastic scattering and of photoproduction, are considered, spanning a large range in the momentum transfer squared of $0 \lesssim Q^2 < 100$ GeV$^2$. A proposal to implement a photoproduction trigger using FTT Level 1 to 3 is made.

This thesis is organised as follows: Chapter 2 gives an introduction into *ep* scattering at HERA, presents the most important kinematic variables from the different kinematic regions, namely deep inelastic scattering and photoproduction. Also, the detection of $D^*$ mesons as well as their main production mechanisms are explained and the relevance of the investigation of these processes is outlined. In chapter 3 the HERA storage ring facility as well as the design of the H1 Experiment and its trigger system are presented in detail. The technical design of the FTT is described in chapter 4, while its performance concerning track resolutions is presented in chapter 5. In chapter 6 the results of the analysis of the efficiency and the rate reduction power of trigger mechanisms to select $D^*$ mesons are presented. All findings are briefly summarised in chapter 7, where also an outlook is given.

[3] Often referred to as slow pion in order to distinguish it from the high momentum pion from the $D^0$ decay.

# 2 Theoretical background

In this chapter the mechanism of electron proton scattering is explained and the most important kinematic variables are introduced. Furthermore the two different kinematic regions at HERA are described. These are deep inelastic scattering and photoproduction, where the momentum transfer squared is $Q^2 >> m_p^2$ or $Q^2 \approx 0$ respectively. Subsequently, the structure functions of the proton are considered, followed by an overview of techniques to measure them experimentally.

Finally the production of heavy quarks in DIS and in photoproduction is discussed along with experimental methods to detect these processes. As an example open charm production is presented, where one of the charm quarks can fragment into a $D^*$ meson. The detection of these mesons in the decay channel $D^* \rightarrow D^0\pi_{slow} \rightarrow K\pi\pi_{slow}$ is then explained.

## 2.1 Electron Proton Scattering

At HERA electrons are collided head on with protons. The basic properties of these collisions can be described using Lorentz invariant variables, that can be calculated from the four vectors of the incoming and outgoing particles. In electron proton scattering the incoming electron interacts with a parton inside the proton either by the exchange of a neutral gauge boson, i.e. $\gamma$ or $Z^0$, and is only scattered off the struck parton (**neutral current exchange process (NC)** (see fig. 2.1a) or it exchanges a charged gauge boson ($W^{\pm}$) and is transformed into a (anti)neutrino (**charged current exchange process (CC)** (see fig. 2.1b). Due to the large mass of the weak gauge bosons, m($Z^0$)=91.19 GeV and m($W^{\pm}$)=80.43 GeV [8], the exchange of photons clearly dominates at not too large values of $Q^2$. Henceforth only photon exchange is considered.

*ep* scattering is described using Lorentz invariant quantities, which are calculated from the four vectors of particles taking part in the interaction. These particles are the incoming electron (with its four vector denoted as $\mathbf{k}$) and the incoming proton ($\mathbf{P}$) as well as the scattered electron ($\mathbf{k'}$). The Lorentz invariant quantities that are used to describe *ep* scattering are:

- **The centre of mass energy squared** $s$, which is defined by four vectors of the incoming particles and thus by the beam energies. At HERA this quantity amounts to $\sqrt{s} = 318$ GeV.
$$s = (\mathbf{k} + \mathbf{P})^2 \approx 4E_eE_P \tag{2.1}$$
- **The four-momentum transfer squared** $Q^2$, which is also called the virtuality of the exchanged gauge boson and defines its (virtual) mass $q$.
$$Q^2 = -q^2 = -(\mathbf{k} - \mathbf{k'})^2 \tag{2.2}$$

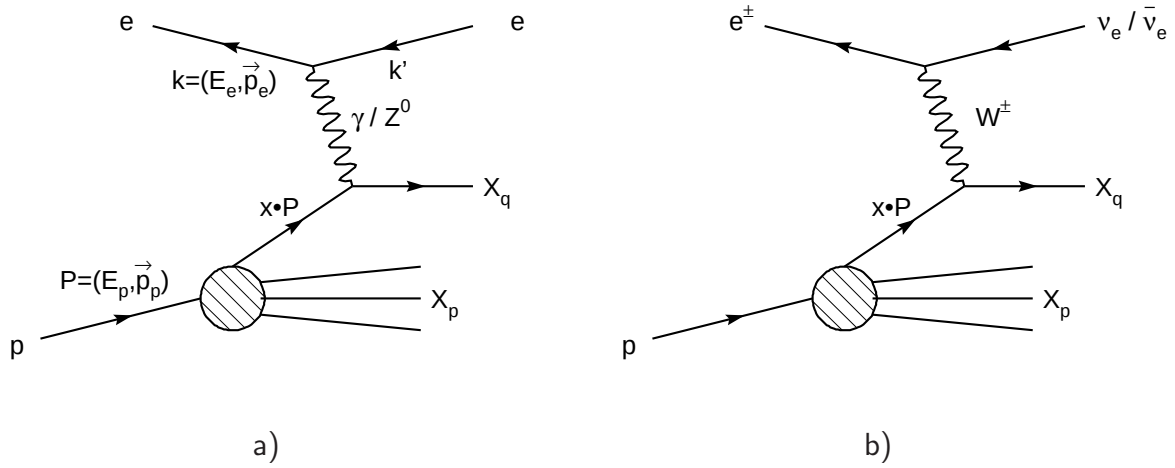


Figure 2.1: Neutral current (a) and charged current (b) exchange processes can be described using the same kinematic variables, which can be calculated using the four vectors of the incoming electron ($\mathbf{k}$), the incoming proton ($\mathbf{P}$), the outgoing lepton ($\mathbf{k}'$) and the struck parton inside the proton ($x \cdot \mathbf{P}$).

- **Bjørken** $x$, the relative momentum fraction of the total momentum of the proton, that was carried by the struck quark. $x$ ranges from 0 to 1 and is given by the following equation.

$$x = \frac{Q^2}{2(\mathbf{Pq})} \tag{2.3}$$

- **The inelasticity** $y$, that equals the relative energy loss of the electron in the proton rest frame and is thus a measure of the energy, which is fed into the hadronic final state and is available during the fragmentation process. Like $x$, the inelasticity is restricted to values between 0 and 1.

$$y = \frac{\mathbf{Pq}}{\mathbf{Pk}} = \frac{E^*_\gamma}{E_e} \tag{2.4}$$

  Here, $E^*_\gamma$ is the photon energy in the proton rest frame.

- **The squared centre of mass energy of the photon-proton system** $W^2_{\gamma p}$ is defined analogue to $s$ by the four-vectors of the incoming proton and the exchanged photon. The centre of mass energy of the photon-proton system determines, how much energy is available for the production of particles.

$$W^2_{\gamma p} = (\mathbf{P} + \mathbf{q})^2 \tag{2.5}$$

  The multiplicity of an $ep$ event depends on the centre of mass energy of the photon-proton system, $\langle n \rangle \sim \ln W^2_{\gamma p}$.

Neglecting the masses of the electron and the proton, the following relations between these quantities can be derived:

$$Q^2 = sxy \tag{2.6}$$
$$W^2_{\gamma p} = ys - Q^2 \tag{2.7}$$

In this approximation it becomes obvious, that in *ep* scattering the number of independent variables is limited. As the centre of mass energy is fixed by the beam parameters, only two of the five quantities introduced above have to be measured in order to obtain full information on the kinematics of an *ep* scattering event. Besides, equation 2.7 reveals that also the inelasticity $y$ is related to the multiplicity of an event. As $s$ is fixed, and $Q^2$ negligible compared to $s$, $y$ is proportional to $W^2_{\gamma p}$: The higher the centre of mass energy of the photon-proton system and the higher $y$, the more particles can be produced in the hadronisation process, and the higher is the multiplicity.

### 2.1.1 Deep Inelastic Scattering (DIS)

In *ep* scattering two kinematic regimes are distinguished. DIS denotes the case, where the four-momentum transfer squared is larger than zero, that is the exchanged virtual photon has a mass $q^2 < 0$. It can resolve the structures within the proton. The resolution power is equivalent to the de Broglie wave length of the virtual photon, given by $\lambda = h/|q_T|$, with the transverse momentum of the exchanged photon $q_T \sim \sqrt{Q^2}$. The smallest structures that can be resolved at HERA are of the size of $\sim 10^{-18}$ m.

In order to make use of the photon as a probe of the proton structure, the full kinematics of the scattering process, that is, all of the kinematic variables introduced in eq. 2.1 to 2.5 have to be reconstructed. As the centre of mass energy $s$ is apriori known, it is fully sufficient to determine $Q^2$ and $y$ to be able to assess $x$ and thus reconstruct the full kinematics (see 2.6). This is done making use of the measured scattering angle and energy of the electron according to following relations:

$$Q^2 = 4\, E_e\, E_{e'}\, \cos^2\left(\frac{\theta_{e'}}{2}\right) \tag{2.8}$$
$$y = 1 - \frac{E'_e}{E_e}\, \sin^2\left(\frac{\theta_{e'}}{2}\right) \tag{2.9}$$

The scattering angle $\theta_{e'}$ is defined as the angle between the outgoing electron and the proton forward direction. Larger values of $Q^2$ thus correspond to smaller values of $\theta_{e'}$ (and vice versa). Due to the limited detector acceptance, only electrons with an scattering angle of $\theta_{e'} < 177°$ can be measured.

### 2.1.2 Photoproduction

Scattering events with a small squared momentum transfer of $Q^2 \approx 0$ are denoted photoproduction events. Here, the electron is scattered at small angles and escapes undetected, therefore photoproduction events are characterised by having no scattered electron in the main detector. This limits $Q^2$ experimentally to $Q^2 \lesssim 1.5$ GeV$^2$ at the H1 detector. The rate with which *ep* scattering events can be observed decreases strongly with increasing

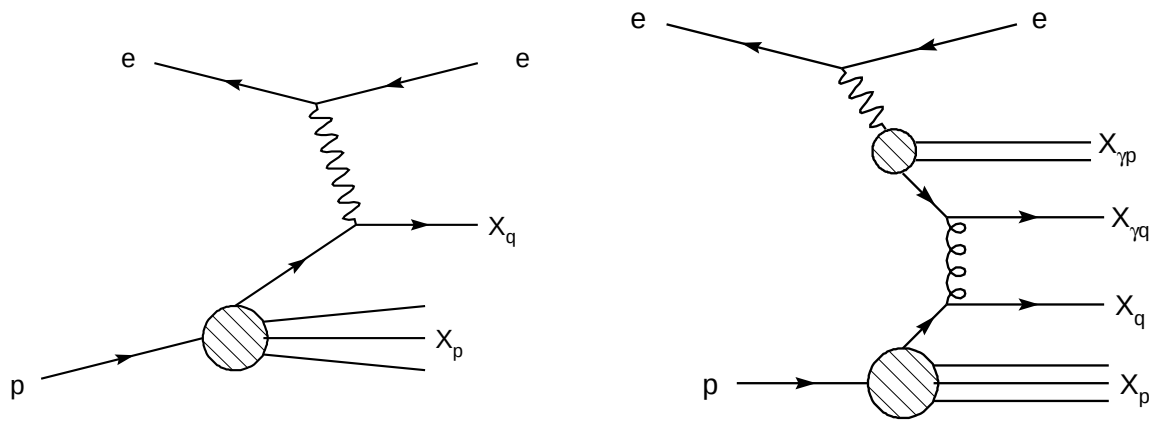


a) DIS and direct photoproduction

b) resolved photoproduction

Figure 2.2: Schematic sketch of DIS ($Q^2 > 0$, a) and photoproduction ($Q^2 \approx 0$) processes. In the later case the photon can either interact *directly* with parton inside the proton (DIS-like, a) or it can resolve into a hadronic state (b). This distinction holds only in lowest order.

momentum transfer; the rate is proportional to $\frac{1}{Q^4}$. Photoproduction events occur therefore significantly more often than DIS events.

In photoproduction, the photon has a mass of $q^2 \approx 0$ and is quasi-real. Therefore it can also fluctuate into hadronic states, e.g. a quark-antiquark pair, on short time scales. However these fluctuations exist still long enough for interactions to take place. Naturally, these interactions then happen between the partons of the photon and the partons inside the proton, so that in photoproduction $ep$ scattering is indeed rather $\gamma p$ or, in the case of photon fluctuations, hadron hadron scattering. While the former, dominantly occurring case, where the photon interacts directly with the partons, is called direct, in the latter case the photon and the processes alike are referred to as resolved (see fig. 2.2).

## 2.2 The quark parton model and the struture of the proton

There is one model that underpins both DIS and photoproduction: An incoming pointlike particle interacts with a parton inside the proton. The fundamental picture underlying this description is known as the naïve **q**uark **p**arton **m**odel (**QPM**). This model states, that the proton consists of pointlike partons, which can be identified as quarks [7]. In DIS as well as in photoproduction, the time scales on which the hard scattering takes place are so short, that during the interaction no information between the struck parton and the other constituents of the protons is being exchanged. Therefore the parton that takes part in the interaction can be regarded as a free, pointlike particle. However, before and after the interaction the constituents of the proton interact with one another and exchange momentum. This is why the single quark flavours do not possess a well defined fraction of the momentum of the proton, but can rather be attributed with a certain probability of possessing a certain momentum fraction $x$. This fraction is also dependent on $Q^2$ due to the dynamics of the interactions between the partons. The dynamics of the partons

are encoded in the parton distribution functions, $q_{flavour}(x, Q^2)$ and $\bar{q}_{flavour}(x, Q^2)$, which describe the probability to find a certain (anti)quark flavour with a certain momentum fraction $x$ inside the proton at a given scale $Q^2$. Unfortunately, these parton distribution functions are not directly accessible experimentally and have to be obtained from fits, which use as input parameters the results of various measurements sensitive to the distribution functions.

One important input to the parton distribution function fits is the inclusive *ep* scattering cross section. The double differential neutral current cross section for moderate $Q^2$, where only contributions from photon exchange have to be accounted for, reads as follows:

$$\frac{d^2\sigma(x,Q^2)}{dx\,dQ^2} = \frac{4\pi\alpha_{em}^2}{x\,Q^4}\left[y^2\,x\,F_1(x) + (1-y)\,F_2(x)\right] \tag{2.10}$$

where $\alpha_{em}$ is the coupling constant of the electromagnetic force. In this formula, two structure functions, $F_1$ and $F_2$, are introduced. In the naïve quark parton model the partons of the proton are exclusively identified with free, pointlike quarks having spin 1/2. In this case, the two structure functions $F_1$ and $F_2$ are dependent on $x$ only. Both are sensitive to the quark content of the proton as the following relations hold:

$$F_1(x) = \sum_{i=1}^{n_f} \frac{e_q^2}{2}\left(q_i(x) + \bar{q}_i(x)\right) \tag{2.11}$$

$$F_2(x) = \sum_{i=1}^{n_f} e_q^2\,x\left(q_i(x) + \bar{q}_i(x)\right) \tag{2.12}$$

where $e_q^2$ is the electric charge of the respective quark. The correlation between $F_1$ and $F_2$ can be expressed also in terms of the so-called Callan-Gross relation, which can be derived independently, based only on the assumption of free, pointlike quarks having spin 1/2:

$$2xF_1 = F_2 \tag{2.13}$$

In the naïve quark parton model the cross section for *ep* scattering is not dependent on $Q^2$, as can be seen from eq. 2.10, when describing *ep* scattering as electrons scattering on free quarks. This scaling behaviour, the independence of *ep* scattering of $Q^2$, is indeed observed, nevertheless only in a region around $x \approx 0.25$. This can be seen in fig. 2.3, where the structure function $F_2$ is plotted against $Q^2$ for different values of x. While $F_2$ is more or less flat for x≈0.25, it tends to rise for lower values of $x$ and tends to decline for higher $x$ values. To explain this feature of $F_2$ the QPM has to be 'QCD-improved', i.e. the fact that the quarks are not free but bound via the strong force has to be accounted for. When doing so and introducing $F_L = F_2 - 2xF_1$, the inclusive *ep* scattering can be rewritten as

$$\frac{d^2\sigma(x,Q^2)}{dx\,dQ^2} = \frac{2\pi\alpha_{em}^2}{x\,Q^4}\left[\left(1+(1-y)^2\right)\,F_2(x,Q^2) - y^2\,F_L(x,Q^2)\right] \tag{2.14}$$

where the structure functions become dependent also on $Q^2$ and $F_L \neq 0$ under the assumption of the partons being in a bound state. Within the theoretical framework of

the QCD-improved QPM, the reason for scaling violations are the dynamics of the strong interaction, that confines the partons in the proton. The quarks of the proton interact dominantly via the strong interaction, i.e. via the exchange of gluons. Alike the photon, also the gluon can split into quark-antiquark pairs, but additionally, they can also radiate further gluons. Therefore, the proton, when viewed with a high resolution power is indeed a very vivid thing. It is build up from its valence quarks, uud, which determine the static properties of the proton like spin, charge etc. But it also contains gluons, which intermediate the strong force between the valence quarks, and sea quarks, quark-antiquark pairs into which the gluons can split up.

The contribution of the gluons to the dynamical properties of the proton is immense: Measurements have shown that gluons carry more than 50 % of the total momentum of the proton [9], [10], [11]. Hence, their influence on the dynamical struture of the proton and *ep* scattering is non-negligible. In fact, the gluon density is one of the most important, but still least determined quantities, when it comes to scattering experiments involving protons. As the next big collider experiment, the LHC, will operate with colliding proton beams, there is an urgent need to understand the proton structure better and to constrain the parton distribution function, especially $g(x, Q^2)$, further [12].

The gluon density can be in principle measured using two independent methods. The first one makes use of the $F_2$ measurements that have been carried out over large ranges of $Q^2$ and x. As $F_2$ depends just on the (anti)quarks densities, it is only indirectly sensitive to the gluon density. The influence of the gluon can be observed in the non-scaling behaviour of $F_2$, which expresses itself in the deviation from a flat distribution in $Q^2$ for the small and large values of x.

The other method to determine the gluon density is directly sensitive to the gluon density of the proton. It makes use of those final states, that are dominantly produced involving gluons. One production channel which is directly sensitive to the gluon density inside the proton, is the production of heavy quarks in *ep* scattering [14].

## 2.3 Heavy Quark Production

Due to their heavy mass charm and bottom quarks are hardly present as sea quarks in the proton, but unlike the top quark they can nevertheless be produced in *ep* scattering at HERA. In the DIS regime the dominant production process is the so-called boson gluon fusion, depicted in fig. 2.4, where the incoming electron emits a photon, which then interacts with an gluon from the proton, producing a heavy quark-antiquark pair. The production processes, that can contribute to the production of heavy quarks in the photoproduction regime apart from the direct process, are shown in fig. 2.5. They all have in common that the photon is resolved.

As the production of heavy quarks involves the fusion of the exchanged gauge boson with a gluon of the proton in direct and resolved boson gluon fusion or the exchange of a gluon in charm excitation, these processes are directly sensitive to the gluon density of the proton. Experimentally heavy hadrons, into which the heavy quarks fragment and which can be measured in the detector, are used as a tag, to identify processes involving

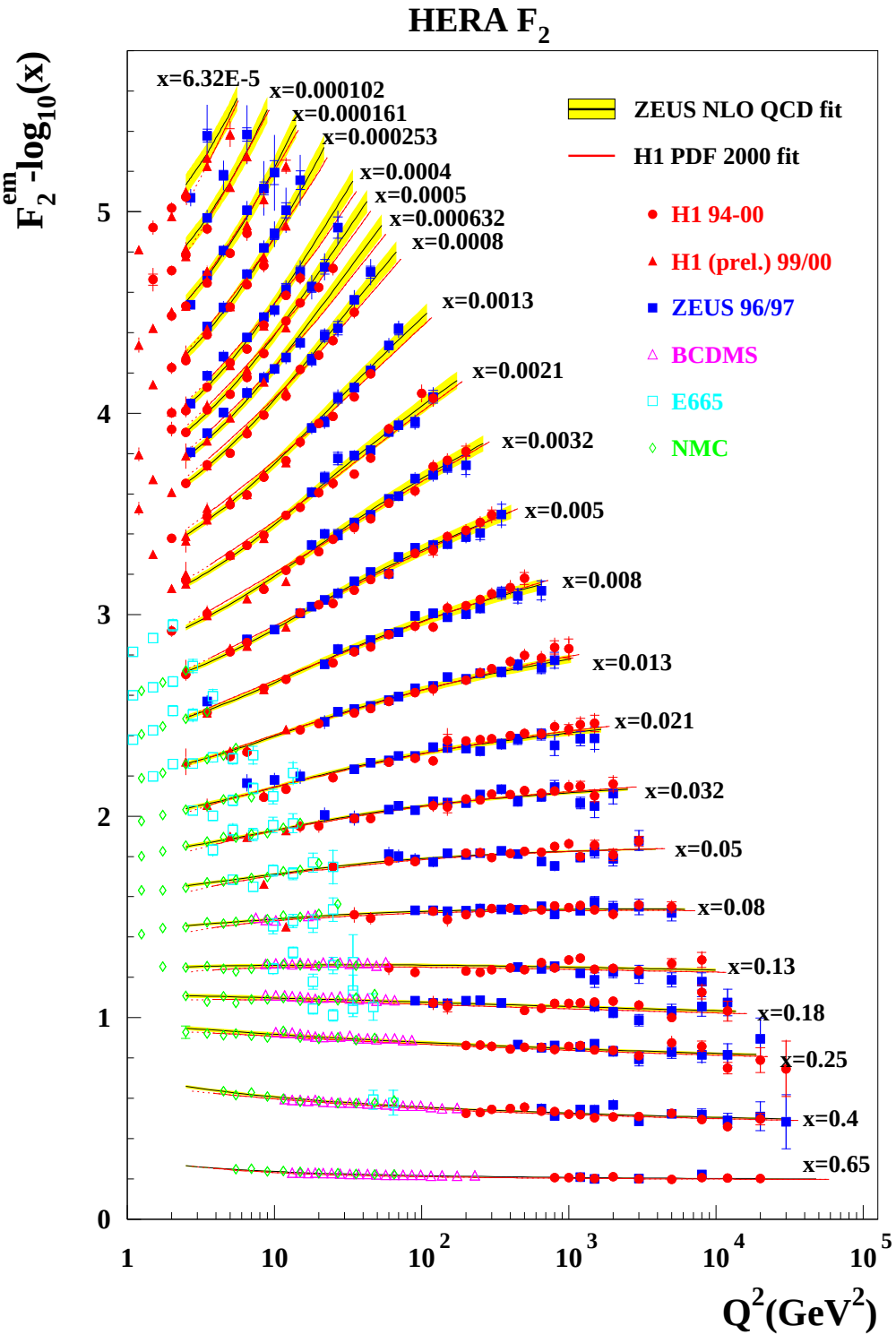


Figure 2.3: The proton structure function $F_2$ as a function of x: Only for x≈0.25 a flat distribution, the so-called scaling behaviour, can be observed. The gluon density is responsible for the rise of $F_2$ at low $x$ values and can be determined indirectly using the slope of $F_2$ (fig. taken from [13]).

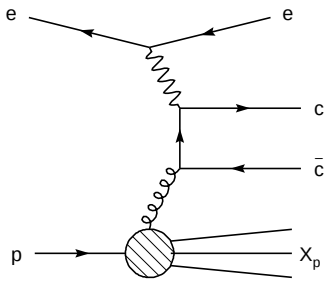


Figure 2.4: Direct boson gluon fusion: The electron emits a photon. In the direct interaction of the photon with the gluon a quark-antiquark pair is produced in lowest order.

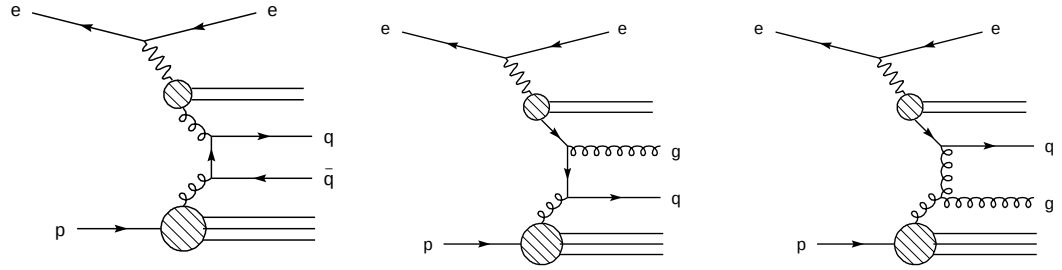


a) resolved boson gluon fusion

b) charm excitation

c) charm excitation

Figure 2.5: Apart from direct boson gluon fusion, as shown in fig. 2.4, there are other processes, that contribute to the production of heavy quarks in *ep* scattering at HERA. These are resolved processes, where a) a gluon from the photon enters the interaction and an additional photon remnant contributes to the multiplicity of the final state and b,c) charm excitation processes, where only one heavy quark from the resolved photon takes part in the hard scattering, the other constitutes a part of the remnant.

boson gluon fusion. Additional to the above introduced kinematic variables, describing inclusive *ep* scattering, the following quantities are of particular interest in the case of heavy quark production:

- **Momentum fraction of the gluon** $x_g$, which describes the momentum fraction of the proton carried by the gluon. $x_g$ is defined as follows:

$$x_g = \frac{\frac{\hat{s}}{x_\gamma} + Q^2}{y \cdot s} = \frac{\frac{M^2(q\bar{q})}{x_\gamma} + Q^2}{y \cdot s} \tag{2.15}$$

  $\hat{s}$ denotes the centre of mass energy of the boson gluon system and can be calculated using $\hat{s}^2 = (g+q_\gamma)^2 = M^2(q\bar{q})$. In photoproduction $Q^2$ equals zero and can be safely neglected. The smaller the $M^2(q\bar{q})$ that can be measured, the smaller the values of $x_g$ that can be accessed. As the size of $M^2(q\bar{q})$ depends on the momenta of the quarks involved, quarks (or the hadrons they fragment into) have to be measured at low momenta.

- **Observed momentum fraction of the gluon** $\mathbf{x}_g$, which describes the experimentally obtained momentum fraction of the proton carried by the gluon, giving the best experimental resolution [15] and neglecting higher order processes, e.g. gluon radiation. The quantity $x_g^{obs}$ is used, as the invariant mass of the heavy quark system cannot be measured directly, because the quarks do not exist as free particle but fragment into heavy hadrons. $x_g^{obs}$ is defined as follows:

$$x_g^{obs} = \frac{(E - p_z)_{Jet1} + (E - p_z)_{Jet2}}{(E - p_z)_{had}} \tag{2.16}$$

  A jet in this context is made up of several particles, spatially close to each other, which are assumed to be the end products of the fragmentation process of the heavy quark. Therefore one of these jets is required to contain a heavy hadron. $(E - p_z)_{had}$ is the difference between energy and longitudinal momentum for the full hadronic final state. Alike $M^2(q\bar{q})$, $(E - p_z)_{Jet}$ is correlated to the transverse momentum of the jets and approximately equals $p_T$. The minimal value of $x_g^{obs}$ that can be measured thus depends on the minimum $p_T$, at which a heavy hadron can be detected. Therefore it is desired to measure heavy mesons at lowest transverse momenta. In lowest order $x_g$ and $x_g^{obs}$ give the same values.

There exists still another reason why the production of heavy quarks is of special interest: QED processes can be calculated perturbatively as a power series of $\alpha_{em}$, since the calculations converge quickly due to the small size of the electroweak coupling $\alpha_{em}$. In QCD, cross sections can be also computed as power series of the strong coupling constant $\alpha_s$, but the series does not converge as rapidly as in QED due to the non-Abelian structure of QCD. Therefore, in **perturbative QCD (pQCD)** special procedures have been developed in order to take care of occurring divergences. These procedures result in the running of the parton density functions, which become dependent on the lower momentum cut-off scale $\mu_F$, down to which soft and collinear gluon emission are explicitly calculated. Therefore parton density functions, measured at a scale e.g. $\mu_F = Q^2$ have to be extrapolated to be valid at another scale. This extrapolation is done with the help of parton evolution

equations. Since in heavy quark production the mass of the heavy quark $m_Q$ provides an alternative cut-off scale $\mu_F = m_Q$, heavy quark production is an ideal testing ground for pQCD parton evolution models over the whole range of $Q^2$. The measurement of heavy quark production cross sections can help to distinguish between theoretical approaches such as standard DGLAP parton evolution equations ([16], [17]) or the alternative BFKL ([18], [19]) or CCFM ([20], [21]) models [22].

However, it is first and foremost important to be able to identify *ep* scattering events, where boson gluon fusion is involved. Boson gluon fusion processes are selected with the help of heavy mesons such as $J/\Psi$ or $D$ mesons [23], [24], [25]. Another method is to tag these processes by a muon, which can be the product of a heavy meson decay [26]. In the following the tagging with the help of $D^*$ mesons and the detection of these charmed mesons is discussed [25].

### 2.3.1 Measurements of $D^*$ mesons

Approximately one fourth of all charm quarks hadronise into charged $D^*$ mesons[1]. The relative fragmentation probability was determined to be [8]:

$$f(c \to D^* X) = 0.224 \pm 0.028 \tag{2.17}$$

$D^{*+}$ ($D^{*-}$) mesons consist of $c\bar{d}$ ($\bar{c}d$) quarks, their mass is $m_{D^*} = (2010.0 \pm 0.5) MeV/c^2$ [8]. In the following only the so-called "golden decay" channel $D^* \to D^0 \pi_{slow} \to K\pi\pi_{slow}$ will be considered. The branching ratios of these subsequent decays are [8]:

$$\mathcal{BR}(D^{*+} \to D^0 \pi^+_{slow}) = (67.7 \pm 0.5)\% \tag{2.18}$$

$$\mathcal{BR}(D^0 \to K^- \pi^+) = (3.8 \pm 0.09)\% \tag{2.19}$$

Even though the total branching ratio of $D^*$ mesons into $K\pi\pi_{slow}$ amounts therefore to only $\sim$2.6%, this channel has still its advantages, because its reconstruction is comparably easy. The mass difference between the $D^*$ and the $D^0$ meson measures $\Delta M = m_{D^*} - m_{D^0} = (145.436 \pm 0.75) MeV/c^2$. Since this value exceeds only slightly the pion mass of $m_\pi = 139.57 MeV/c^2$, the phase space for the emitted pion is very limited. The restriction of the phase space makes it possible to measure the number of produced $D^*$ mesons using the distribution of the mass difference $\Delta M = m(K\pi\pi_{slow}) - m(K\pi)$. The advantage is that by subtracting the two masses systematical errors cancel as well, therefore the resolution for $\Delta M$ is much better than for $m_{D^*}$ or $m_{D^0}$ distributions separately. Fig. 2.6 shows the $m_{D^0}$ distribution for DIS [25] and the $\Delta M$ distribution for photoproduction [26] respectively, both from recent H1 publications.

So far, $D^*$ mesons were successfully studied at H1 in order to test cross section predictions of the standard model [27]; they were also used as a tag for charm quark production to extract gluon densities [28]. Furthermore, the applicability of different pQCD models was tested and compared in $D^*$ events [29] as well as jet shapes and the influences on them could be studied with the help of heavy quark production [30]. In addition, production channels, involving $D^*$ mesons, were used in order to search for new phenomena [31] [32].

[1] If not stated otherwise, the term $D^*$ mesons always refers to both charge states.

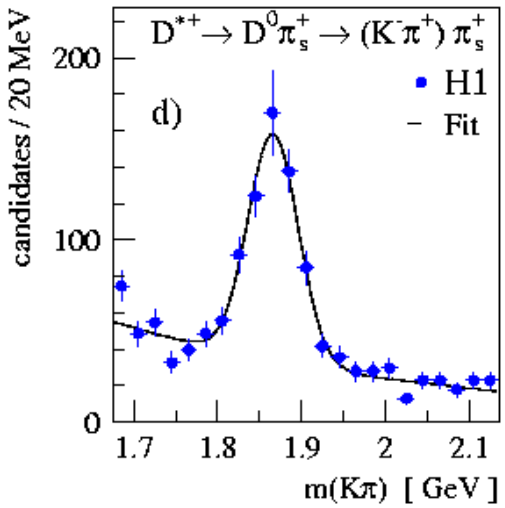


a) $D^0$ resonance [25]

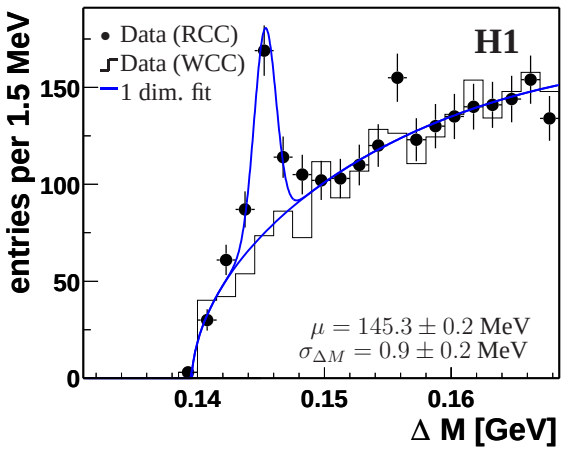


b) $\Delta$m = M(K$\pi\pi_s$) - M(K$\pi$) resonance [26]

Figure 2.6: Invariant mass distributions for $D^0$ mesons and for $D^*$ mesons reconstructed in their golden decay: $\Delta$ M = M(K$\pi\pi_s$) - M(K$\pi$).

Many more analyses are planned or are at a preparation stage, e.g. [33], [34]. However, at the moment the total error of these analyses is still dominated by statistical rather than by systematic uncertainties. All $D^*$ meson analyses would profit from an increase in total luminosity and data taking rate for $D^*$ mesons. Even more is to gain for photoproduction analysis: as at the H1 detector up to now only "tagged" photoproduction events[2] could be selected for storage, most of the $\gamma$p phase space was lost for analysis.

[2] "Tagged" photoproduction events are events, where the scattered electron is detected under extremely small polar angles $\theta'_e$ with special detectors as described in sec. 3.2.

# 3 HERA & H1

In this chapter a short overview over the HERA collider is given. Then, the H1 experiment is introduced, followed by a detailed description of the detector components crucial to this thesis. The chapter is concluded with a presentation of the data acquisition and trigger system.

## 3.1 The HERA storage ring

The HERA storage ring is situated on the site of the research institution **D**eutsches **E**lektron **Sy**nchrotron (DESY) in Hamburg. It consists of two independent storage rings, one for protons and one for electrons, with a circumference of 6.4 km. Protons as well as electrons are accelerated in up to 220 bunches, each containing $\sim 10^{10}$ particles. The final energies are 920 GeV for protons and 27.6 GeV for electrons. Both, electrons as well as protons, have to pass through a system of pre-accelerators, before they are injected into HERA with energies of 12 and 40 GeV respectively. The accelerator facilities as well as the locations of the experimental halls are depicted in fig. 3.1. Due to the geometry, the maximal number of bunches and the velocity of the beam particles being almost the speed of light, the rate of bunch crossings in the interaction regions of the HERA accelerator amounts to ∼10.4 MHz.

One of the three operating experiments at HERA is a fixed target experiment, Hermes, which uses only the electron beam for investigations of the spin structure of the proton by colliding the electrons on polarised gas targets. In two interaction regions the particle beams are collided, there the general purpose collider experiments ZEUS and H1 are situated. Until 2003 the experiment HERA-B was in operation; it investigated heavy quark physics by using a system of wires as target for the proton beam.

All these experiments measure the rates of certain physical processes. This rate is given by the following relation:

$$\mathrm{Rate}_{\mathrm{process}} = \mathcal{L}\,\sigma_{\mathrm{process}}, \tag{3.1}$$

where $\sigma_{\mathrm{process}}$ is a measure for the general probability of a physics process to happen. $\mathcal{L}$ denotes the luminosity, a quantity fixed by beam parameters such as the number of particles in the beam, $N_i$, their collision frequency $\nu$ and the lateral coordinate widths of the bunches in the interaction region, $\sigma_i^2$:

$$\mathcal{L} \sim \frac{N_p N_e \nu}{2\pi\sigma_p^2\sigma_e^2} \tag{3.2}$$

With the end of the year 2000 the HERA underwent a major machine upgrade, which distinguishes HERA-I (1993-2000) and HERA-II (2002 onwards). The aim of this machine upgrade was to increase the luminosity by focusing the beams more sharply in the

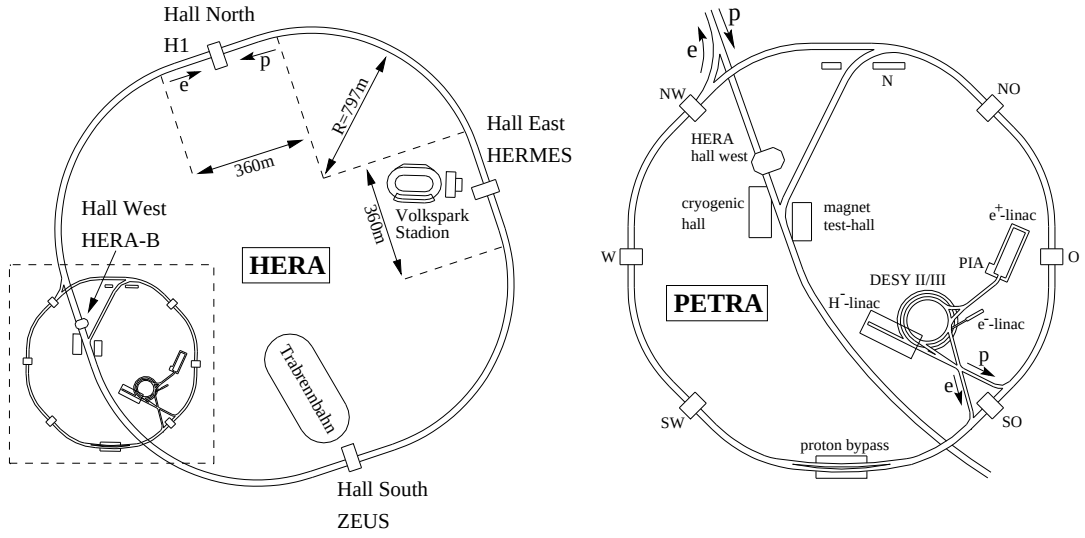


Figure 3.1: A map of the HERA storage ring is shown on the left hand side, the position of the experiments and of prominent landmarks are indicated. The dotted square marks the position of the pre-accelerator and is drawn enlarged on the right hand side, where the complete system of pre-accelerators on the DESY site is depicted.

interaction regions and thus to decrease the lateral coordinate widths. However these constructional changes are accompanied by an expected increase of synchrotron radiation. It arises from the sharper focussing causing a stronger bending of the electron trajectory, which is the direct reason for the higher synchrotron radiation. Another obstacle is that, despite of the increase in delivered data, the amount of recordable data is still restricted due to technical reasons. That implies, that there is not only the need to filter out more background events online, that is during the data taking process, but that there is also the need to select among the physics events those, which are most important to the physics programme. In order to address this question beforehand, the luminosity upgrade was complemented by a detector upgrade and a revised trigger strategy taking into account the virtue of new trigger subsystems built in the context of the upgrade. Detector and trigger system as they are set up for the HERA-II phase are described in the following.

## 3.2 The H1 Experiment

The H1 collaboration uses a multi-purpose detector with an almost 4 $\pi$-coverage around the interaction point [a] (see fig. 3.2). A general overview is given in [35] and [36], where the setup of the detector is described for the HERA-I phase. The detector is designed asymmetric – the instrumentation in the forward proton direction is enhanced, since the centre-of-mass is not at rest in the laboratory frame but is boosted in the proton beam direction. This is because the proton is a factor 30 more energetic than the electron because of the asymmetric beam energies of 920 GeV for protons and 27.6 GeV for electrons. Due to the asymmetric energy distribution most of the multiplicity of an event is produced in the direction of the outgoing proton beam. This is therefore often referred to as forward direction, while the direction of the outgoing electron is also named backward direction.

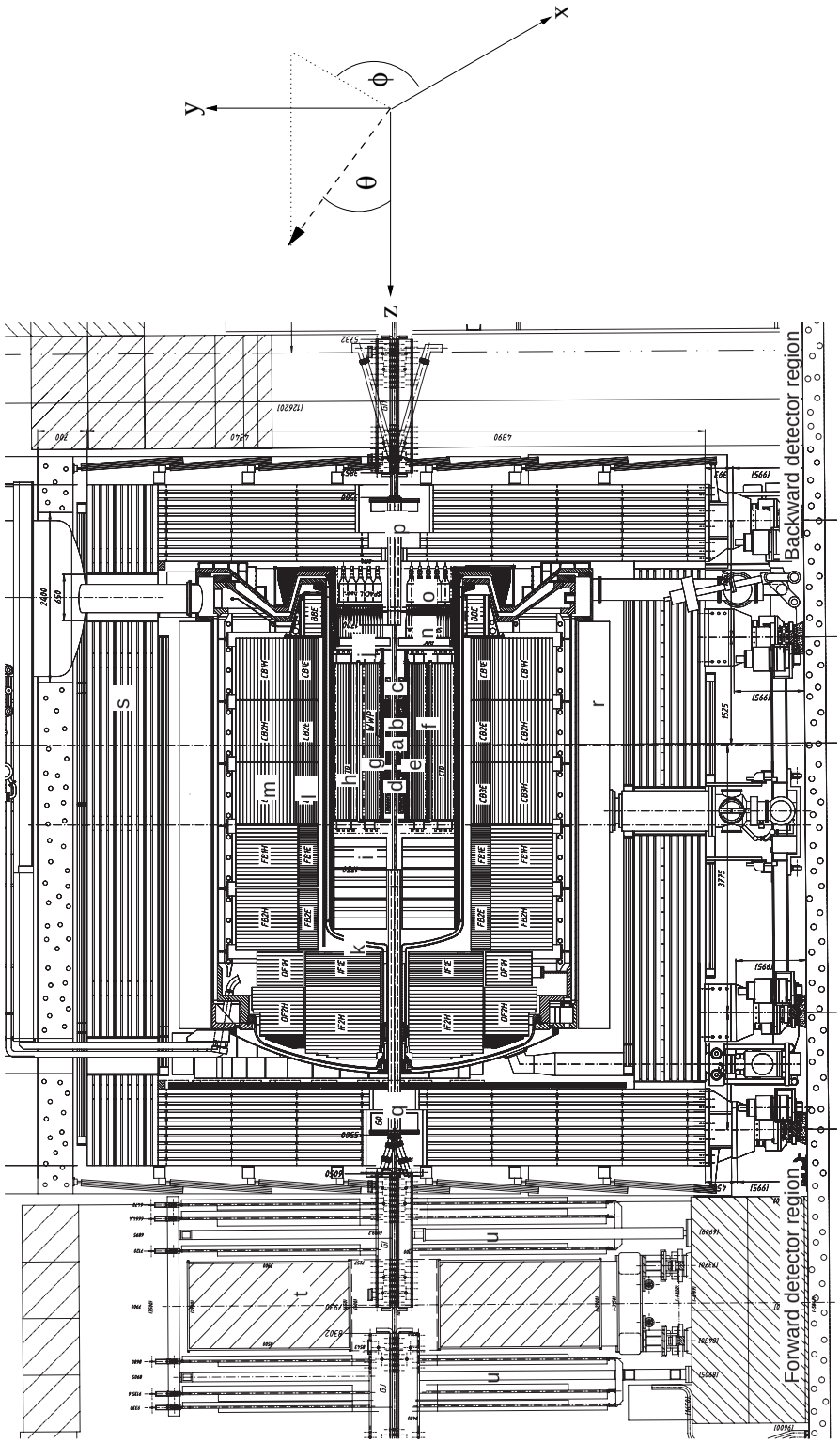


| | | | | | | | |
|---|---|---|---|---|---|---|---|
| a | Interaction **P**oint (**IP**) | h | **C**entral **J**et **C**hamber 2 (**CJC2**) | o | **Spa**ghetti **Cal**orimeter, hadr. (**SpaCal** hadr.) |
| b | **C**entral **S**ilicon **T**racker (**CST**) | i | **F**orward **T**racking **D**etector (**FTD**) | p | supra-conducting magnet (forward direction) (GG) |
| c | **B**ackward **S**ilicon **T**racker (**BST**) | j | **B**ackward **P**roportional **C**hamber (**BPC**) | q | supra-conducting magnet (backward direction) (GO) |
| d | **F**orward **S**ilicon **T**racker (**FST**) | k | **L**iquid **Ar**gon Cryostat (**LaR**-Cryostat) | r | supra-conducting solenoid |
| e | **C**entral **I**nner **P**roportional Chamber **2000** (**CIP2000**) | l | **L**iquid **Ar**gon **C**alorimeter, elm. (**LaR** elm.) | s | **C**entral **M**uon **D**etector (**CMD**) |
| f | **C**entral **O**uter z-Chamber (**COZ**) | m | **L**iquid **Ar**gon **C**alorimeter, hadr. (**LaR** hadr.) | t | Muon Toroidal Magnet |
| g | **C**entral **J**et **C**hamber 1 (**CJC1**) | n | **Spa**ghetti **Cal**orimeter, elm. (**SpaCal** elm.) | u | **F**orward **M**uon **D**etector (**FMD**) |

Figure 3.2: The H1 detector in side view.

The coordinate system at H1 is defined as a right-handed coordinate system. The origin coincidences with the interaction point [a], while the positive $z$-axis is defined to point into the direction of the outgoing proton beam. The $y$-axis points perpendicular upwards, while the $x$-axis is defined to point towards the centre of the HERA ring. The solid angles are defined as follows: The polar angle $\theta$ is defined as the angle between an outgoing particle and the z-axis, while the azimuthal angle $\phi$ is the angle in the $x$-$y$-plane. The coordinate system is also schematically sketched in fig. 3.2.

The H1 detector is constructed such, that around the interaction point ([a]) silicon trackers ([b],[c],[d]) provide high resolution of the interaction vertex and possible secondary decay vertices. These inner structures are embedded in the tracking chambers, where momentum, charge and direction of the tracks as well as the vertex of the interaction are determined ([e] - [j]). The adjacent calorimeters, both the liquid argon calorimeter and the spaghetti calorimeter making use of scinttilating fibres, measure the energy of the particles via their energy deposit ([k] - [o]). All these components are enclosed in a superconducting solenoid ([r]), providing a 1.16 T magnetic field, which is crucial to the momentum measurement in the trackers. Two other superconducting magnetic structures are built-in close to the beam pipe. These are the GO and GG magnets ([q] and [p]), which provide the final focussing of the beams. The completion of the detector is the muon system ([s] and [u]), which is equipped with its own magnetic structures ([t]). The muon chambers are designed to detect muons, which in general do not deposit their whole energy in the calorimeters and are not stopped in the calorimeters. The detector components of the H1 experiment shall be explained in detail in the following:

- **Silicon Tracker:** At H1 the system of silicon trackers is composed of the **C**entral **S**ilicon **T**racker (**CST** [b]), the **B**ackward **S**ilicon **T**racker (**BST** [c] [37]) and the **F**orward **S**ilicon **T**racker (**FST** [d]). The main use of the BST is to detect the scattered electron in its fiducial acceptance region of $165° \lesssim \theta \lesssim 176°$ delivering complementary information to those of SpaCal [38]. The FST is designed to improve tracking in the forward region for $8° \leq \theta \leq 16°$ [39]. The CST covers the central region of the detector with $30° \lesssim \theta \lesssim 150°$ [40].

- **Central Proportional Chambers:** The **C**entral **I**nner **P**roportional Chamber **2000** (**CIP2000** [e] [41]) provides information on the z-coordinate of tracks and on the vertex from which the tracks of an event are originating. It consists of five cylindric multiwire proportional chambers with pad readout and wires parallel to the beam pipe [42]. Further information is obtained with the help of the **B**ackward **P**roportional **C**hamber (**BPC** [j]), which is installed in front of the backward calorimeter, in order to measure the track of scattered electrons with a polar angle $156° \lesssim \theta \lesssim 174.5°$. It also helps to distinguish electrons from photons which both deposit their energy in the calorimeter.

- **Forward Tracker:** The **F**orward **T**racking **D**etector (**FTD** [i]) consists of three supermodules containing different types of tracking devices. The FTD covers a polar angular range of $5° \lesssim \theta \lesssim 30°$.

- **Central Drift Chambers:** The **C**entral **J**et **C**hambers, CJC 1 [g] and CJC 2 [h], are the heart of the H1 tracker system. Their combined geometrical acceptance

for the polar angle covers $15^\circ \lesssim \theta \lesssim 165^\circ$ [43]. Both are drift chambers with wires parallel to the $z$-direction. While $r$-$\phi$ information is obtained from the drift time of the charges within the chamber, the $z$-coordinate is measured via charge division along the wires and is therefore less precise. The resolutions obtained average $\sigma_{r\phi} = 0.17$ mm and $\sigma_z = 22$ mm [36]. Information from the CJCs is used within the FTT system, therefore the layout of the chambers is described below in further detail. Additional $z$-information is delivered by the **C**entral **O**uter **z**-Chamber (**COZ** [f], [36]), a drift chamber whose inclusion in the event reconstruction leads to an improved resolution in $r$-$z$ of $\sigma_{rz}$ =380 $\mu$m.

- **Backward Calorimeter:** The **Spa**ghetti **Cal**orimeter (**SpaCal**) is a lead scintillating fibre calorimeter consisting of two sections, electromagnetic ([n] [44] and hadronic ([o] [45]). Its acceptance in $\theta$ ranges from $155^\circ \lesssim \theta \lesssim 177^\circ$. Both parts of the SpaCal consist of cells with quadratic cross sections. They contain the lead-embedded scintillating fibres, which convert showers, induced by entering particles, into light pulses. The electromagnetic part has a four times finer granularity compared to the hadronic part and achieves a spatial resolution of $\approx$ 3mm. The SpaCal is used for triggering purposes in the mid-DIS regime ($1.5\ \mathrm{GeV}^2 \lesssim \mathrm{Q}^2 \lesssim 100\ \mathrm{GeV}^2$ corresponding to the angular acceptance of the calorimeter). As it is used in this analysis, it is described in further detail below.

- **Liquid Argon Calorimeter (LAr):** In the forward detector region of $4^\circ \lesssim \theta \lesssim 154^\circ$ the energy of the particles is measured using the **L**iquid **A**rgon **C**alorimeter (**LaR** [36]), which also consists of an electromagnetic ([l]) and a hadronic section ([m]). It is constructed as a sampling calorimeter with alternating layers of argon as active material and lead (em. section) as well as stainless steel (hadr. section) as absorber material. The LAr energy resolution was measured to be $\sigma_E/\mathrm{E} \approx 11\%/\sqrt{E/GeV} \oplus 1\%$ for the electromagnetic section and $\sigma_E/\mathrm{E} \approx 50\%/\sqrt{E/GeV} \oplus 2\%$ for the hadronic section [46]. The calorimeter is embedded in a cryogenic system [k], in order to provide sufficient cooling to keep the argon in the liquid phase.

- **Muon Detector:** The muon system of the H1 Experiment consists of the **C**entral **M**uon **D**etector (**CMD** [s]) and the **F**orward **M**uon **D**etector (**FMD** [u]) [36]. The CMD consists of limited streamer tubes, which are mounted on the magnet coil and the iron magnetic flux return yoke and serve also to detect energy deposits which leak out off the LAr. The CMD covers the angular region of $6^\circ \lesssim \theta \lesssim 172^\circ$, whereas the FMD has an acceptance of $3^\circ \lesssim \theta \lesssim 17^\circ$. The latter detector consists of drift chambers mounted on either side of a toroidal magnet [t].

- **Time of Flight and Veto system:** The time of flight system and the veto walls are designed to distinguish between $ep$ scattering from background events such as beam gas interactions using differences in their timing [47], [48]. These systems consist of scintillating detectors readout by photomultipliers.

- **Luminosity system and electron taggers:** The luminosity at H1 is determined using the well-calculable Bethe-Heitler process $ep \leftrightarrow ep\gamma$ [49]. The radiated photons are detected by a photon tagger, a calorimeter placed close to the beam pipe at $z$=-103m, while the electrons are detected with an electron tagger at $z$=-6m and $z$=-40m. The rate with which in both devices signals are detected in coincidence

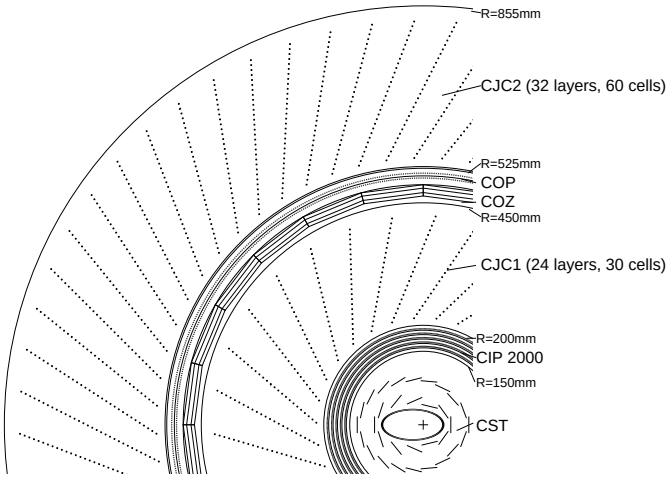


Figure 3.3: A radial view of the H1 tracking system with the CJCs. Only their signal wires are depicted in order to enhance the clearness of the drawing.

allows to determine the luminosity online. For the offline determination of the luminosity only the signals from the photon tagger are used, which results in a statistical precision of 2% [35], [50]. The electron taggers are also capable of tagging photoproduction events, where the scattered electron leaves the main detector undetected under a very small scattering angle, meaning 0 GeV$^2 \lesssim Q^2 \lesssim$ 1.5 GeV$^2$. At the beginning of 2006 a new electron tagger has been installed at $z$=-40 m [51].

### 3.2.1 Central Jet Chambers (CJC)

With an active $z$-length of 2.2 metres the CJCs are the largest tracking devices of the H1 experiment, they are the main instruments to obtain track information. Both chambers are placed around the beam pipe in the central detector region with an radius of 203 mm$\leq R_{CJC1} \leq$ 451 mm (CJC1) and 530 mm$\leq R_{CJC2} \leq$ 844 mm (CJC2). They are separated by the COZ and the COP (central outer proportional chamber), see fig.3.3.

CJC1 consists of 24 layers of azimuthal wires, which are grouped into 30 cells, which extend azimuthally from the sense wire to both adjacent cathode wires and radially over the full radial span of CJC1. Thus it makes use of 30×24 sense wires, while CJC2 is operated with 60×32 sense wires. As shown in fig. 3.3, the jet chamber cells are tilted by about 30° with regard to the radius vector from the origin to ensure that the electrons drift perpendicular to the traversing ionising particles and thus to improve the resolution for high momentum tracks. Additionally this helps also to solve the usual track ambiguities, which arise from the fact that it is not a priori known on which side of the wire the charged particle passed. The most important parameters of the chambers are summarised in table 3.1.

The CJCs are both jet chambers filled with an gas mixture (Ar-$CO_2$-$CH_4$) that is ionised, once a charge particle traverses the chamber. Free electrons originating from these ionisations are accelerated with the help of anode wires. Thus amplification is obtained, an avalanche develops and once the electrons reach the anode wires an electronic

| | CJC1 | CJC2 |
|---|---|---|
| **acceptance in $\theta$** | | |
| total acceptance | $22.3° \lesssim \theta \lesssim 157.7°$ | $27.5° \lesssim \theta \lesssim 142.5°$ |
| partial acceptance | $10.5° \lesssim \theta \lesssim 169.5°$ | $25.7° \lesssim \theta \lesssim 154.3°$ |
| **number of wires per cell** | | |
| sense wires | 24 | 32 |
| potential wires | 50 | 66 |
| field wires | 10 | 10 |
| cathode wires | 49 | 65 |
| **resolutions** | | |
| $\sigma_{r\phi}$ | 0.17 mm | |
| $\sigma_z$ | 22 mm | |
| $\sigma_t$ | 0.5 ns | |
| $\sigma_{dE/dx}$ | 10 % | |
| double hit resolution | 2 mm | |

Table 3.1: Overview over the most important parameters of the central jet chambers [36].

signal can be measured. An algorithm, which takes into account pulse shape and timing of this charge signal as well as its integral, is used to extract from the measured signals on each end of the wires the time $t$ the electrons needed to drift onto the anode wire with respect to the time $t_0$, which is the time of the $ep$ scattering.

### 3.2.2 Spaghetti Calorimeter (SpaCal)

The SpaCal is constructed as a sampling calorimeter with scintillating fibres which are embedded into lead as absorber material. Electrons and photons intruding in the lead produce electromagnetic showers, which enter the scintillating material and are converted into light, whose intensity is proportional to the deposited energy and can be measured using photomultipliers. The active fibres used in the SpaCal measure 0.5 mm in diameter for the electromagnetic section. 90 of these fibres at a time are embedded in a layer of lead. At the ends they are bundled into two ropes, each of which are connected to a light mixer, that distributes the light to the adjacent photomultiplier and ensures that it is homogeneously illuminated. Each photomultiplier is read-out with a quadratic cross section of $40.5 \times 40.5$ mm$^2$. 1192 of these form the electromagnetic section of the SpaCal. Two read-out channels represent a so-called submodule, eight of which are grouped into a supermodule. The energy resolution for the electromagnetic part is found to be $\sigma_E/\mathrm{E} \approx 7.5\%/\sqrt{E/GeV} \oplus 1\%$ [52], for the hadronic section $\sigma_E/\mathrm{E} \approx 36\%/\sqrt{E/GeV} \oplus 4\%$ [53]. When an energy deposit is detected in the SpaCal, a clustering algorithm is used in order to combine the hit read-out channels into clusters, which are attributed to a particle each.

## 3.3 The H1 Trigger System

While the bunch crossing rate at HERA amounts to 10.4 MHz, the actual cross section of $ep$ scattering leads to a nominal physics rate of roughly 1000 Hz. The observed rate

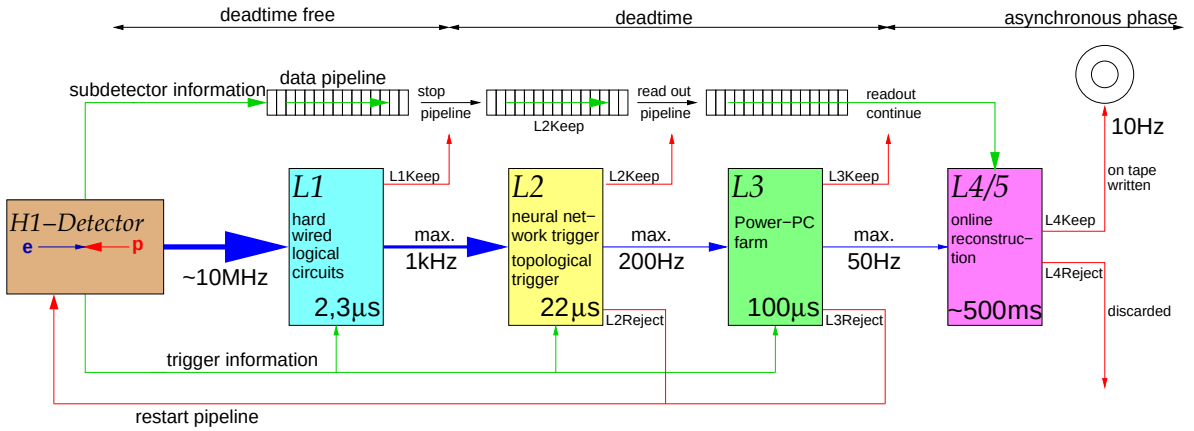


Figure 3.4: A schematical sketch of the H1 trigger system (after [55]).

however amounts to approximately 50 000 Hz [54], as there is a rather high percentage of background events that cause signals in the detector. The reasons are proton beam gas interactions and proton beam wall interactions, where stray protons interact either with rest gas molecules in the beam pipe or hit solid parts of the detector or the beam pipe, producing particle showers. Other sources are synchrotron radiation and cosmic muons. The data acquisition system is pipelined, but the length of these buffers is limited, so that in case an event should be recorded permanently, the pipelines have to be stopped to prevent the event from being overwritten and to read it from the buffers. Because of this, during the complete read-out of the detector no further events can be taken. Therefore it is necessary to cut down the rate of read-out background events to a minimum in order to decrease the deadtime due to the detector read-out, which takes 1 ms. Also, there is the need to select among the real *ep* events those, which are most important to the H1 physics programme. Trigger systems make the decision, whether to readout or not, based on partial information coming out of the several detector components.

### 3.3.1 Design of the Trigger System

In order to optimise the decision, the H1 trigger system is designed as a multi-level system, schematically shown in fig. 3.4. On each of the four trigger levels more time is available, such that the decision can successively be more refined and sophisticated.

#### Level 1

The first level runs parallel to the operation of the detector and does not contribute to the deadtime, since a system of data pipelines stores temporarily detector information. This results in an available decision time of 2.3 $\mu$s. On level 1 the included trigger subsystems of the respective subdetectors transmit in total 256 so-called **t**rigger **e**lements (**TE**), which encode information e.g. on the energy deposit in the SpaCal or the number of tracks over certain thresholds in the CJCs. Using hard-wired, but still programmable logic circuits these trigger elements are combined into 128 subtriggers. In case one or more of the 128 subtrigger conditions are fullfilled the data pipeline is stopped. This corresponds to a so-called L1 KEEP signal, triggering a halt of data taking and thus starting the deadtime.

Within the current H1 trigger strategy an output rate of 1 kHz for the level 1 system with its 128 subtriggers is desired in order to restrict the deadtime to be $\leq 10\%$.

### Level 2

The second trigger level operates during the deadtime of the detector. It consists of dedicated purpose built hardware and makes use of the full detailed trigger data of most subsystems, including some which are not available at earlier stages. Level 2 is actually composed of three independent systems, the neural network trigger ([56], [57]), the second level of the FTT ([58], [59], [60]) and the topological trigger ([61], [62]). The latter employs $r\phi$ correlations between the signal of various detector subsystems in order to distinguish between background and physics events, which have a somehow different topology. The former systems are explained in detail in section 3.3.3 and chapter 4.

On level 2 the decision time is fixed to 22 $\mu$s during which either a L2 KEEP or a L2 REJECT signal has to be transmitted to the central trigger. Whereas a L2 KEEP signal triggers the actual readout of the detector, a L2 REJECT signal restarts the pipeline, resuming data taking. The envisaged output rate of L2 is limited to 200 Hz.

### Level 3

Level 3 was realised as a part of the FTT project and is designed as a farm of Power-PCs, which perform an event reconstruction with information from the trigger subsystems. If L3 succeeds in calculating the invariant mass of every possible combination of tracks and if it does not find any of these masses to be consistent with a particle resonance within some mass window, a L3 REJECT signal is sent, which immediately stops the detector readout and resumes the data taking. Thus, deadtime is significantly reduced in case L3 is fast enough. In case L3 does not manage to analyse every track combination within the time limit of 100 $\mu$s, the search is aborted and an automatic L3 KEEP signal is created by the central trigger. A L3 KEEP signal is of course sent as well if a resonance has been found. The contemplated output rate is 50 Hz.

### Level 4

Level 4 is an asynchronous software trigger, which is integrated into the central data acquisition system. The L4 algorithms are started once the readout has been finished. L4 has access to all raw data and could hence be used to reconstruct the full online event with the full intrinsic detector resolution. The trigger comes to a L4 REJECT or L4 KEEP decision within approximately 500ms. In case of a L4 KEEP signal the raw data of the full event is stored permanently to disk. L4 is also used for monitoring purposes by filling online histograms that can be evaluated by the detector shift crews. The envisaged logging rate, which fixes the output rate of L4, is 10 Hz. At the same time it also fixes the input rate of L4 to 50 Hz, which means, it must be made sure, that the output rates of the subsequent trigger levels L1 to L3 are reduced such the L4 input rate amounts to 50 Hz. In order to make sure that these specifications can be met, a certain trigger mix together with prescaling strategies are chosen ([63], [64]).

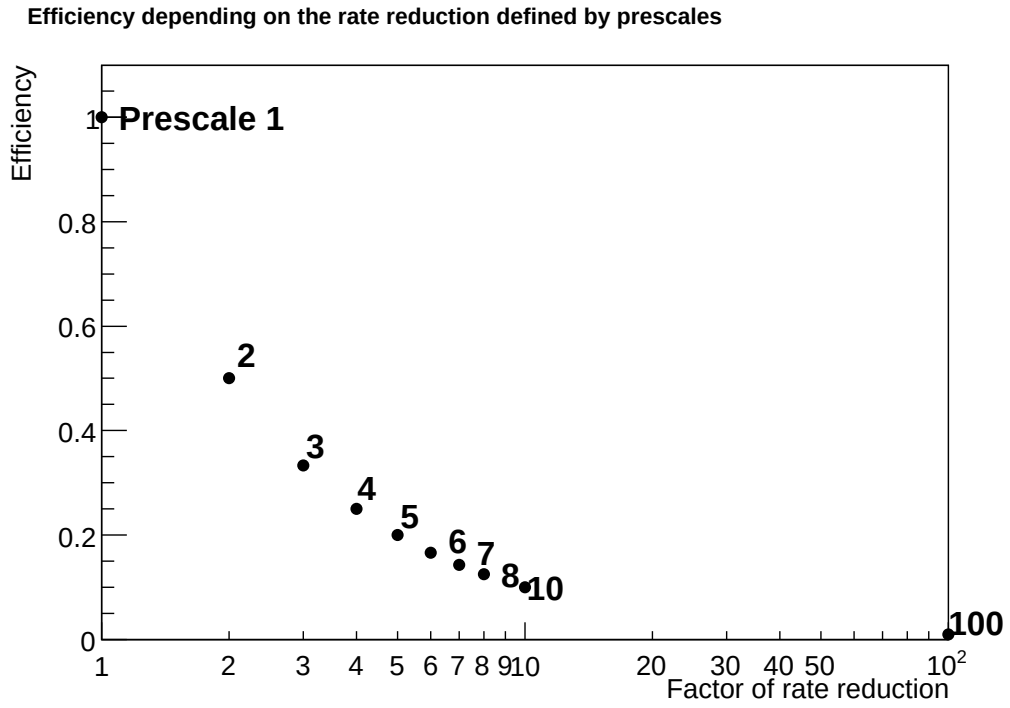


Figure 3.5: The efficiency for different prescales and the corresponding rate reductions. The efficiency for a given prescale x amounts to $\epsilon = \frac{1}{x}$ as only one out of x events is kept.

### 3.3.2 Trigger strategies: Prescales and event weights

Because of the restricted input rate allowed for the L4 system, the preceeding trigger levels are limited to certain output rates. That implies that rates have to be reduced on each trigger level such that the output rate matches the defined input rate of the subsequent level. In case this condition can not be fullfilled using the intrinsic rate reduction power of the subtrigger, the procedure of downscaling is applied. Downscaling of triggers means, that out of all, so-called raw, positive trigger decisions only every x-th is defined to be an actual trigger decision and actually triggers a KEEP signal. In other words, a prescale of x corresponds to arbitrarily choosing every x-th triggered event for further processing. This arbitrary selection of course also extends to the signal events, from which also only every x-th is kept. Hence, a rate reduction with the help of prescales has immediate effects on the corresponding efficiency of the trigger, defined in eq. 6.2 in section 6.1. This correspondence is shown in fig. 3.5, where the efficiencies for different prescale values and the resulting rate reduction (defined in eq. 6.2 in section 6.1) are depicted.

For the various physics channels exist different independent triggers with different rate reduction powers and efficiencies, depending on the nature of the respective physics channel and its signature in the detector. The degree of discrimination from background events determines the 'trigger ability' of a process, the easiness with which it can be selected among background events. Sometimes a trigger has to be implemented, knowing that it will have to be prescaled since it has not enough intrinsic rate reduction power. In order to maximise the amount of data taken, the prescales at H1 are not predefined and fixed, but are applied dynamically according to a predefined trigger strategy.

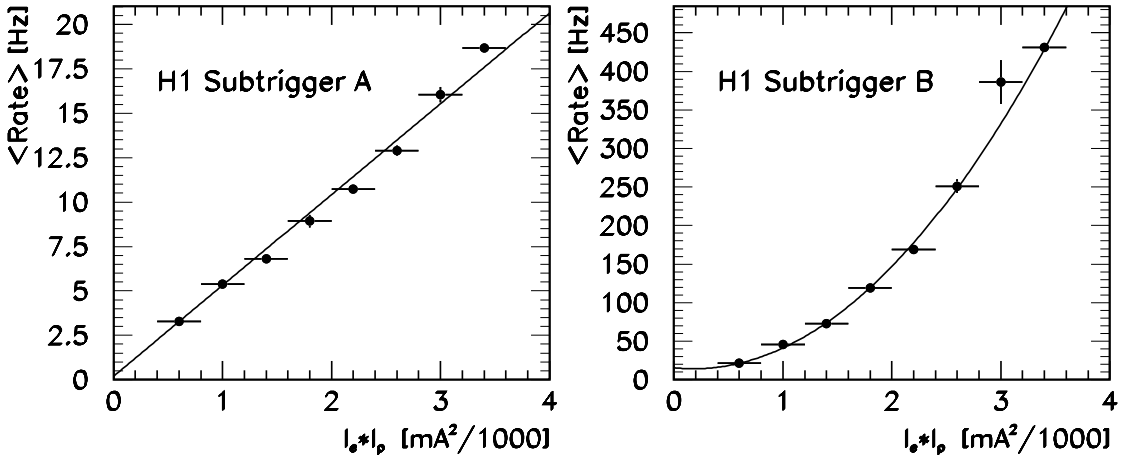


Figure 3.6: Subtrigger A and B depend differently on the luminosity $\mathcal{L} \sim I_e I_p$, with $I$ being the currents of the electron and the proton beam respectively [63].

This procedure of autoprescaling [63] makes use of the fact that subtriggers depend differently on the instantanous luminosity, as shown in fig. 3.6. Here, the rate of subtrigger B rises quadratically with the luminosity, a behaviour typical for triggers suffering from pile-ups or accidental coincidences. Hence, subtrigger B does not produce the best physics yield at high luminosities. As the purity of the events triggered by B tends to decline with rising luminosity, the allowed output rate should not rise linearly with the raw rate of the subtrigger. The rate of subtrigger A on the other hand rises linearly with the luminosity, its purity tends to be constant. Therefore, the rate after prescaling should be higher for subtrigger B in case of low luminosity in comparison to the after-prescale rate of subtrigger A, while it should be the other way around for high luminosities.

On L1 the output rate of 1kHz is shared among the different subtriggers, which are pooled into groups corresponding to various physics channels. Each of these groups or physics channels are attributed with a predefined bandwidth, a prescale or with a weight. In this context the allowed bandwidth defines the maximum rate, the trigger group is allowed to take, while a predefined prescale fixes, whether every x-th or every y-th event is thrown away. A weight defines the allowed share of either the overall budget or the budget prescribed to a group of triggers. During data taking the prevailing output rates are regularly checked and the prescales adjusted accordingly. Because of the dynamical adjustment of prescales depending on the beam conditions, an overall higher efficiency in data taking can be achieved. In between those checks and adjustments, the prescales stay constant. The data taking periods with constant prescales are called runs. Normally, a run contains about 20 000 to 30 000 events. As autoprescaling is used at H1, its implications should be taken into account, when optimising a trigger in terms of rate reductions and efficiencies as well.

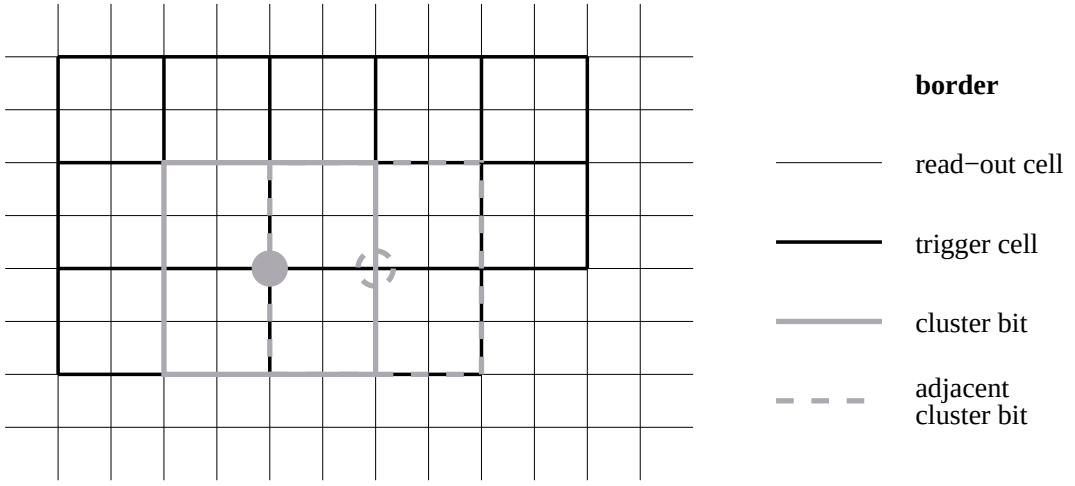


Figure 3.7: The arrangement of IET trigger cells and cluster bits [65].

### 3.3.3 Trigger Subsystems

In the following, the trigger subsystems used in this analysis shall be introduced in more detail. This concerns the SpaCal inclusive electron trigger, the CIP z-vertex trigger, the LAr trigger as well as the level 2 neural network. The Fast Track Trigger will be introduced in the next chapter.

#### SpaCal inclusive electron trigger (IET)

The **i**nclusive **e**lectron **t**rigger (**IET**) trigger is designed to select events with a scattered electron in the backward calorimeter. It uses information on the energy deposits in trigger cells, each of which consist of 2×2 readout channels of the electromagnetic section of the SpaCal. The respective total energies of the trigger cells then contribute to the energy of so-called cluster-bits, which sum up the energies of 2×2 trigger cells. Since on every edge of each trigger cell a centre of a cluster bit is placed (see fig. 3.7), their distance amounts to 8.1 cm and their area to 16.2×16.2 cm$^2$, which is significantly larger than $\pi \times (\mathrm{R}_{Molière} = 2.55\mathrm{cm})^2$=20.43cm$^2$, the size of the projected shower profile in the $r$-$\phi$ plane. Thus, each trigger cell contributes to the energy sum of in total four cluster bits and it is made sure, that at least one cluster bit collects the total energy of a single electromagnetic cluster. The trigger information transmitted encodes, whether at least one cluster-bit contained an electromagnetic cluster with an energy above the predefined trigger level energy threshold:

| **SpaCal_IET** | IET>0 | IET>1 | IET>2 |
|---|---|---|---|
| **energy threshold** | 3 GeV | 6 GeV | 9 GeV |

The innermost part of the SpaCal is called central IET region. It is the most active region as it corresponds to the lowest $Q^2$. Due to the high level of radiation in these parts, the percentage of energy deposits caused by synchrotron radiation or beam gas interactions is significantly higher than in the outer parts of the SpaCal. Therefore, subtriggers with IET trigger elements included are validated on level 2, where a radius

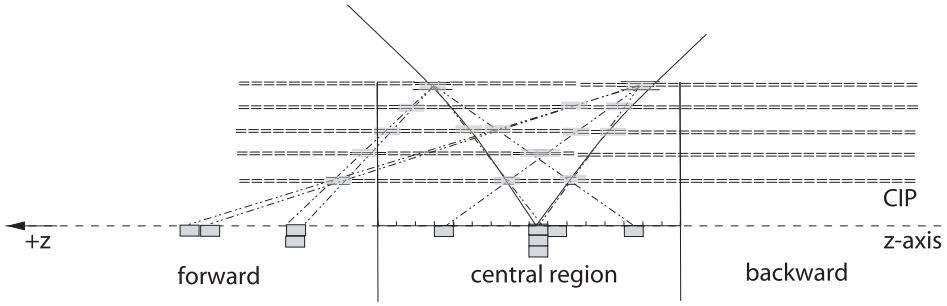


Figure 3.8: Working principle of the CIP2k z-vertex trigger: All tracks found in the five chamber are extrapolated to the $z$-axis and added to a $z$-vertex histogram, whose 22 bins are divided in forward, central and backward region. Depending on the relation between the number of possible tracks in the respective regions, the events is classified as *ep* scattering or background event.

cut is applied and all events, where the position of the cluster bit is situated within a radius of 20 cm around the beam pipe, $R_{ClusterBits} \leq 20$ cm, are rejected. Moreover on analysis level, those parts of the SpaCal have to be identified, where the readout and trigger cells did not work properly.

### CIP z-vertex trigger

The CIP2000 z-vertex trigger uses information from the five chamber layers of the CIP2000 and looks for hit patterns, which can be combined to rays and extrapolated onto the $z$-axis. Their respective $z$-position is filled into a $z$-vertex histogram, whose bins are classified as forward, central and backward, as shown in fig. 3.8. Depending on the relation of central rays to the sum of backward and forward rays, a CIP significance is defined, which can be used to distinguish on Level 1 within 2,3 $\mu$s between background and possible *ep* interactions:

$$\#_{Central\,Tracks} > S \times (\#_{Backward\,Tracks} + \#_{Forward\,Tracks})\,, \tag{3.3}$$

where S translates to the corresponding significance trigger bits as follows:

| **CIP_sig trigger bit** | 0 | 1 | 2 | 3 |
|---|---|---|---|---|
| **corresponding significance S** | 0 | 1 | 2 | 4 |

In addition, the CIP2k trigger delivers information on time of the bunch crossing, CIP_T0, as well as on the number of track combinations pointing to the $z$-vertex in the CIP chamber, encoded in seven bits:

| **CIP_mul trigger bit** | 1 | 2 | 3 | 4 | 5 | 6 | 7 |
|---|---|---|---|---|---|---|---|
| **corresponding multiplicity** | >0 | >2 | >6 | >10 | >20 | >30 | >65 |

### LAr big tower

In order to be able to supply the central trigger within less than 2.3$\mu$s with information on the energy deposit in the LAr calorimeter, the 45000 channels of the calorimeter are

comprised into 4845 so-called trigger cells ([66]). From these, 688 **t**rigger **t**owers (**TT**) and 256 **b**ig **t**owers (**BT**) with an ever coarser granularity are formed. Each of these towers are split up into an electromagnetic and in a hadronic section. The spatial division of the LAr into these towers depends on the solid angle $\theta$, with finer granularity for small values of $\theta$, as the foremost forward region is expected to populated with a higher particle (and energy) density. Their distribution is shown in fig. 3.9. In the azimuthal angle $\phi$ the calorimeter is divided into up to 32 BTs.

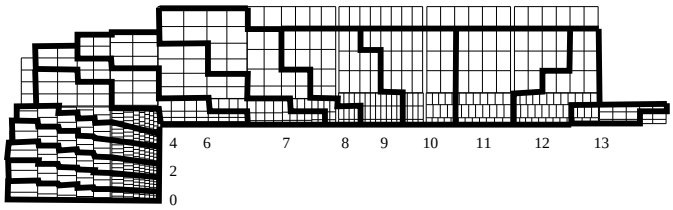


Figure 3.9: The segmentation of the LAr trigger towers along the z-axis [67].

The information delivered to the central trigger includes information on the $t_0$, the number of electromagnetic clusters detected in the electromagnetic section of LAr, in order to trigger high $Q^2$ events, as well as the sum over the energies of the BTs in the forward region as well as in the central and forward barrel, in order to trigger events with a large (missing) transverse energy. A still prevailing problem of the LAr trigger is a high level of noise, which couples in from external devices such as the magnets or power supplies. The lower the energy threshold for triggering, the higher the contribution from noise. On the other hand a low energy thresholds are desired, in order to be able to trigger also events with low transverse energies efficiently. Statistically, noise in the LAr causes high trigger rates for the LAr-based trigger. This has the advantage that LAr based subtriggers can be used as monitor triggers in efficiency analysis for processes, the LAr based subtriggers are actually not designed to trigger.

### Level 2 neural network trigger

Neural networks belong to a group of methods, employing statistical learning, in order to do pattern recognition. At H1 the **L2 n**eural **n**etworks (**L2NN**) consists of parallel processors, which are fed with the information from the different detector subsystems available at the time of the trigger decision [56],[68].

The neural network has to be trained beforehand with a set of signal and background events. When evaluating a so far unknown event, the neural networks calculates a probability $0 < P < 1$ for an event to belong to the signal. Depending on this probability the event can be either rejected or kept. The cut-off for $P < P_{\mathrm{cut-off}}$ is adjustable and can be chosen freely, allowing for an optimisation in terms of rate reduction and efficiency. As an example, the values for rejection power and efficiency that can be obtained for triggering $D^*$ mesons in untagged photoproduction is shown in fig. 3.10 [69]. The line is the curve for all possible cut-off values.

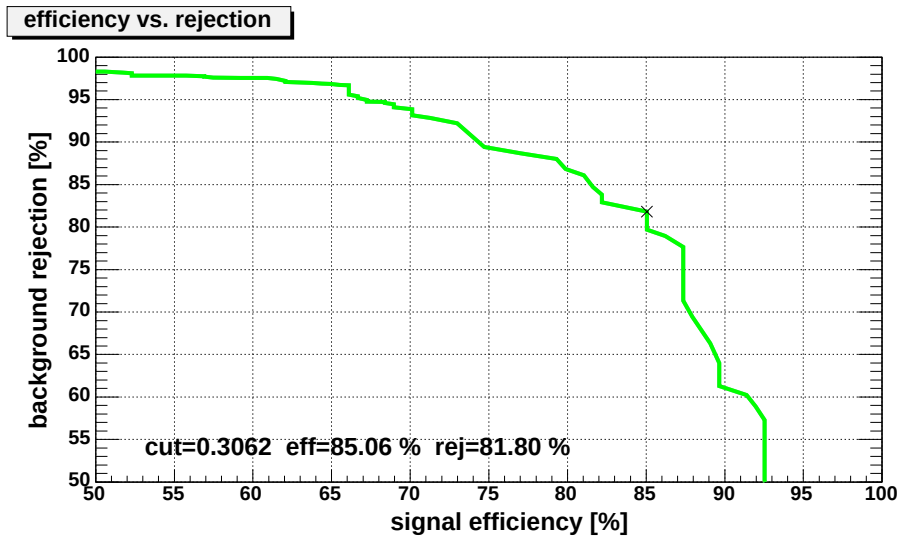


Figure 3.10: Relation between efficiency for background rejection versus the signal efficiency for L2NN-triggered $D^*$ mesons [69]. The solid line represents the obtainable performance as function of the different cut-off values. The cross indicates the relation between background rejection and signal efficiency for a cut-off value of 0.3062. The background rejection is here defined as $\frac{\#\text{triggered events}}{\#\text{total events}} \times 100$.

# 4 Technical realisation of the Fast Track Trigger (FTT)

The **F**ast **T**rack **T**rigger (FTT) ([58], [59]) is a trigger system, which reconstructs tracks out of information from the CJCs. Various track quantities are then used in order to deliver trigger signals on the first three levels of the H1 trigger system ([54], [70]). In this chapter the technical realisation and the working principle of the FTT are described.

## 4.1 Track parameters

When charged particles traverse the CJCs, their path is bend according to the Lorentz' force, due to the magnetic field of 1.16 T inside the detector. Thus, the track of a charged particle, starting at the nominal interaction point, resembles a 3-dimensional helix structure (4.1). In order to describe it, five parameters are used:

- **Curvature $\kappa$:** The curvature of a track is defined as the inverse radius of the track projected onto the $r$-$\phi$-plane. In the presence of a homogeneous $z$-component of the magnetic field $B$, $\kappa$ is related to the signed transverse momentum $P_T$ according to:

$$P_T\,[GeV] = -Q[C] \times c[\frac{m}{s}] \times B_z\,[T] \times \frac{1}{\kappa\,[m^{-1}]}, \tag{4.1}$$

  with $Q$ being the charge of the particle, measured as multiples of the elementary charge, $c$ the speed of light and $B_z$ the magnetic field in the $z$-direction.

- **Distance of closest approach $d_{ca}$:** The smallest distance between the projection of the track into the $r$-$\phi$-plane extrapolated from the point of measurement to the interaction region and the origin of the H1 coordinate system is called the distance of closest approach, $d_{ca}$.

- **Azimuthal angle $\phi$:** The angle between the tangent of the track at the $d_{ca}$ point and the $x$-axis is defined to be the azimuthal angle $\phi$.

- **Polar angle $\theta$:** The angle between the axis of the helix path of the track and the $z$-axis is defined to be the polar angle $\theta$.

- **Coordinate $z_0$:** The $z$-coordinate of the $d_{ca}$ point is defined as the $z_0$ of a track.

The tracks of particles in drift chambers have to be reconstructed from the space points, where free charges have been produced along the path of a traversing ionising particles. In case of the full reconstruction, this is done by a sophisticated and time-consuming fit-algorithm, the non-iterative algorithm of Karimäki for $\kappa$,$\phi$ and $d_{ca}$ [71] and a subsequent linear least-squares fit for $\theta$ and $z_0$. For the online reconstruction of tracks as needed for a fast track trigger this is however not possible, therefore dedicated means were developed to find an optimal compromise between fast convergence and accurate resolution.

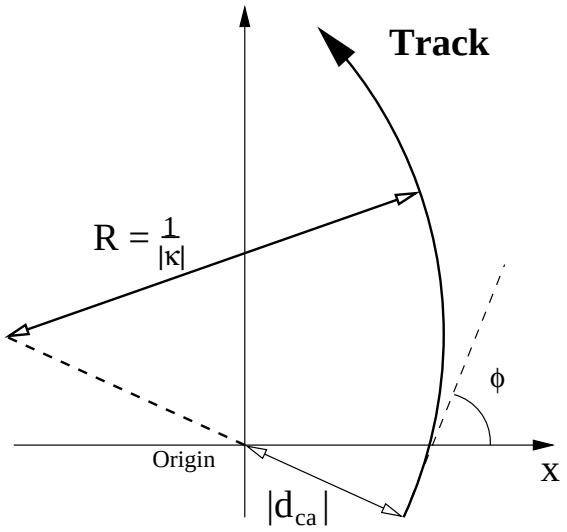


Figure 4.1: Schematic sketch of the definition of the track parameters $d_{ca}$, $\kappa$ and $\phi$ in the $x$-$y$ plane.

## 4.2 Technical Realisation

For the FTT not the full information from the CJCs is used, but instead only four trigger layers consisting of three wire layers each are taken into account. As a consequence only 4×3, i.e. 12, wire layers out of 56 are used. The FTT is much faster, because is uses only part of the wires normally used in the offline reconstruction, which has the advantage of being more precise. The spatial distribution of the FTT trigger layers is shown in fig. 4.2. Whereas in the inner chamber CJC1 three trigger layers are used, the outer chamber CJC2 contains only one trigger layer. The layout of the trigger cells, which constitute the smallest entity of the FTT, is sketched in fig. 4.3.

### 4.2.1 Track finding on Level 1

On the first trigger level, the analogue pulses from the CJC wires are digitised at a frequency of 80 MHz. This is done via a **d**ifference **o**f **s**ample (DOS) algorithm, which returns the charge $Q$ measured at a time $t$ on the respective CJC wire. This $Qt$ information is filled into shift registers with a frequency of 80 MHz. Within these shift registers the algorithm then looks for hits by searching for charges $Q$ exceeding the noise level. Time information can be thus extracted with a precision of 2-3 ns. The $z$-coordinate is obtained using a charge division technique, that is via the ratio of the charges on the opposite ends of a wire are used to determine the $z$-coordinate. This yields a precision of $\sigma_z \approx 6$ cm.

In order to be able to achieve a trigger decision within the 2,3 $\mu$s available on the first trigger level L1 four shift register entries are combined, thus reducing the effective digitisation to 20 MHz for the first level. The shift registers are then used in order to perform a parallel search for track segments in all trigger cells consisting each of three primary wires plus two wires from neighbouring cells, in order to account for tracks crossing cell boundaries. As it is still unclear at this stage, on which side the track passed the signal wire, there are two shift registers filled for each wire. Each assuming the actual track to

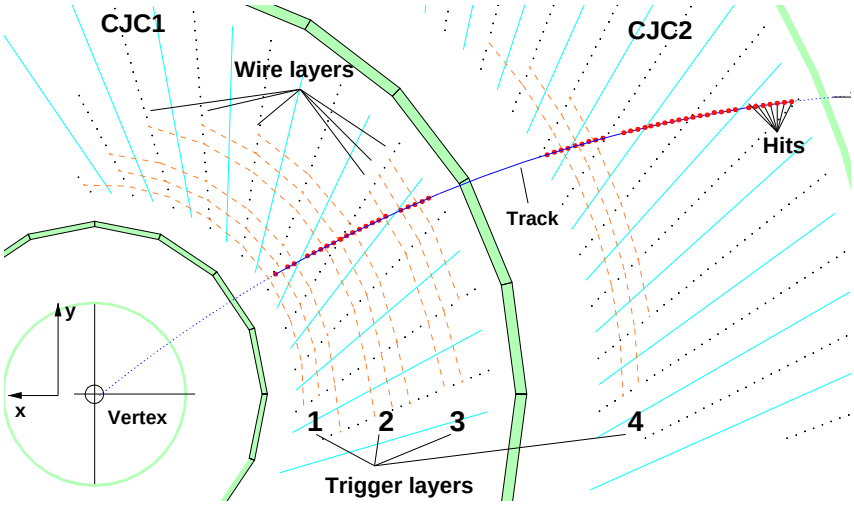


Figure 4.2: A radial view of the CJCs and the 4×3 wire layers used by the FTT. Depicted are the used sense wires as well as the walls of the cell.

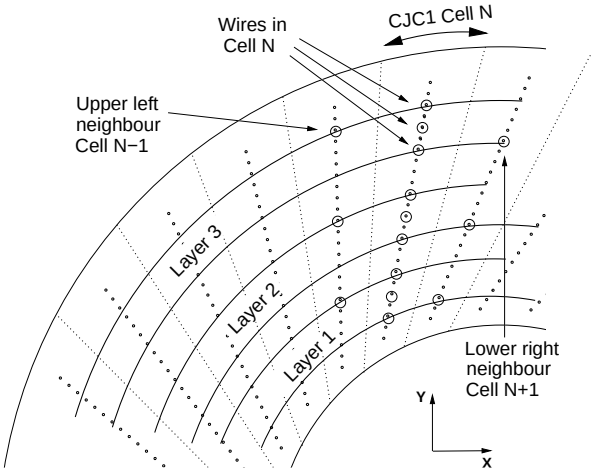


Figure 4.3: Layout of the FTT trigger cells. Indicated are also the neighbourig wires used in the segment finding.

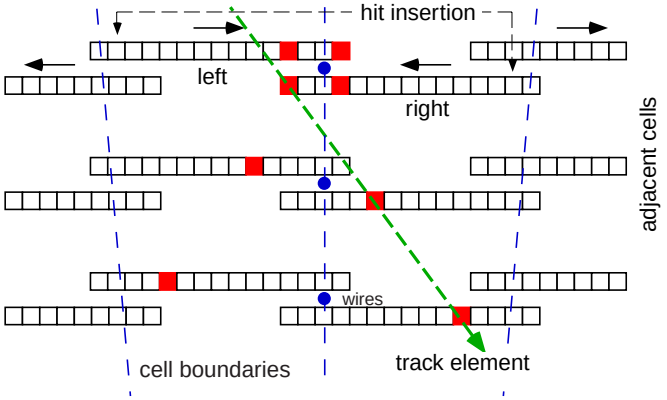


Figure 4.4: Here the filling of the shift registers and the finding of track segments in a trigger cell is scematically shown: A passing track, depicted as a dashed line, traverses the cell, causing electron to drift onto the wire. After the respective drift times, which depend purely on the distance of the primary ionised particles from the wire, hits are detected on the wires. They are filled into registers, which are shifted from left to right and from right to left, in order to account for both possible drift directions of electrons. In case the hits in the shift registers (here marked darkly) match the precalculated hit pattern of a possible track, a track segment in the trigger cell has been found.

be lying on the right or left hand side of the used signal wire. The bit patterns in the shift registers represent free charges generated $n_{bit} \times 80 \cdot 10^{-6} s^{-1} \times v_{driftvelocity}$ away from the position of the wire. Any track traversing a trigger cell should be characterised by specific bit patterns, that can be calculated beforehand for each track and each trigger cell (see fig. 4.4).

Track segments, i.e. possible tracks through a trigger cell, are found by comparing the online found bit patterns with so-called masks, which are pre-calculated sets of all the bit combinations that could possibly be caused by "valid" tracks coming from the nominal vertex and passing through the respective trigger cell. The track segments are characterised by specific values of $\kappa$ and $\phi$, which are precalculated corresponding the respective mask used in the segment finding. On the subsequent stage of track finding, the linking of track segments in the four layers is performed. In the course of this procedure, the found track segments of each of the four trigger layers are filled according to their $\kappa$-$\phi$ values into one 2-dimensional histogram with a $\kappa$-binning appropriate in resolution to the time resolution of the shift patterns. In this case $16 \times 60$ bins are used, with 60 equaling the number of CJC2 cells. If the $\kappa$-$\phi$ values for at least two valid track segments of different trigger layers are consistent, i.e. fall into the same $\kappa$-$\phi$ bin or neighbouring bins, they are linked to a valid track (for a schematic overview see fig. 4.5). When the segment linking is done, the left/right ambiguities are resolved, as the $\kappa$-$\phi$ values stay consistent over the different trigger layers only for those track segments, where the correct assumption was made concerning the side of the signal wire on which the particle traversed the trigger cell.

The found track information is then evaluated and various trigger elements are constructed in order to summarise this information, which is then transmitted to the central

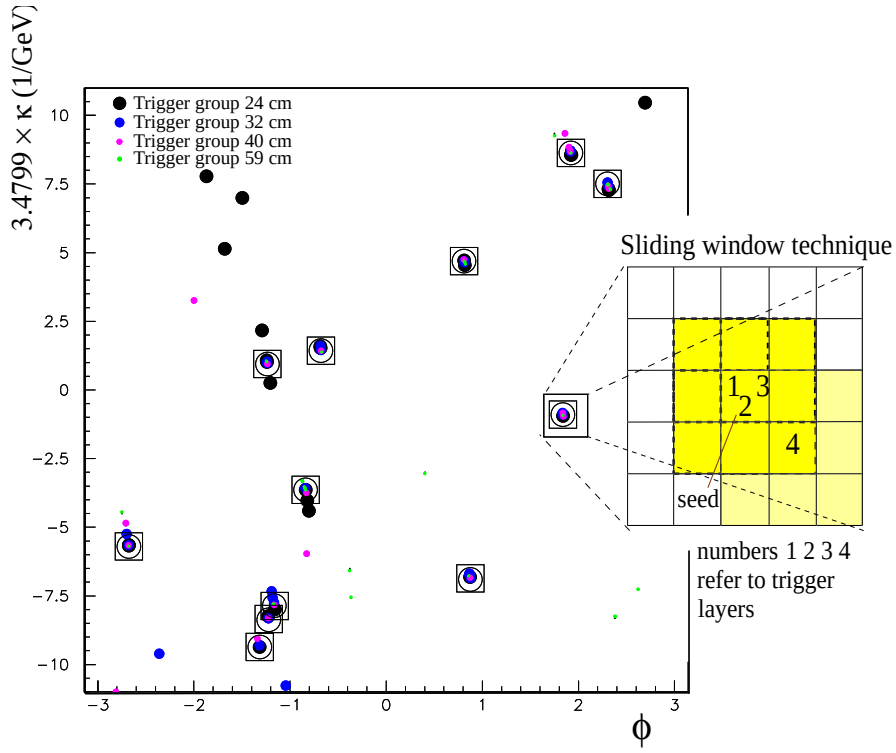


Figure 4.5: The information on the $\kappa$-$\phi$ values of found track segments is filled into a histogram. Then these segments are linked to tracks, when at least two of them are consistent in $\kappa$-$\phi$. With a sliding window technique, neighbouring bins are also taken into account.

| FTT-L1 Trigger element | Meaning | |
|---|---|---|
| **# tracks above $P_T$ Threshold** | | |
| FTT_mul_Ta | 100 MeV | # tracks 0 to ≥7 |
| FTT_mul_Tb | 160 MeV | # tracks 0 to ≥3 |
| FTT_mul_Tc | 400 MeV | # tracks 0 to ≥3 |
| FTT_mul_Td | 900 MeV | # tracks 0 to ≥3 |
| FTT_mul_Te | 1800 MeV | # tracks 0 to ≥3 |
| **Topological triggers** | | |
| FTT_topo_0 | back-to-back topology | |
| FTT_backtoback_2 | back-to-back topology wide angle | |
| FTT_isotrack | isolated track | |
| FTT_2isotrack | one or two weakly isolated tracks | |
| FTT_eplusjet | Neutral current topology (electron plus jet) | |
| FTT_topo_5 | isotropic topology | |
| FTT_topo_6 | Only one hemisphere contains tracks | |
| **Other trigger elements** | | |
| FTT_seg | At least one segment found | |
| FTT_Qtot | Total charge | $Q_{tot}$ <≤ to ≥+3 |
| | more > 7 track of one charge (NaN) | |

Table 4.1: FTT L1 trigger elements transmitted to the central trigger [72].

trigger. The implemented trigger elements for use in the level 1 decision are summarized in tab. 4.1 [72]. They encode the number of tracks above certain transverse momentum thresholds as well as the total charge in an event and its topology, e.g. the spatial distribution of linked segments.

### 4.2.2 Refined track finding and track fitting on Level 2

At level 2 initially the segment finding and linking as described above are carried out again, using at this stage the full shift register information with a digitisation sampling of 80 MHz instead of the 20 MHz used at L1. Hence a better time resolution and consequently a higher spatial resolution is achieved. The $\kappa$-$\phi$ histogram used for segment linking is therefore significantly finer binned, it uses $40 \times 640$ bins instead of $16 \times 60$ as done on Level 1. When at least two segments with consistent $\kappa$-$\phi$ values are found, the ($x$,$y$)-coordinates of each of the linked segments are calculated. Depending on the calibration, which takes into account the drift velocity and the precise position of the signal wires, precise information on the space coordinates of the hits belonging to a mask can be extracted.

The thus obtained ($x$,$y$)-coordinates are then used in a non-iterative circle fit in the $r$-$\phi$-plane, which also uses the event vertex in the fit and assumes the tracks to be coming from it [54], [70]. This fit makes the track parameters $\kappa$ and $\phi$ more precise. The track parameters $r$ and $\phi$ can be determined with a resolution that is about a factor 20 better

| FTT-L2 Trigger element | Meaning | |
|---|---|---|
| **# tracks above $P_T$ Threshold** | | |
| FTT_mul_Ta | 100 MeV | # tracks >0 to >7 |
| FTT_mul_Tb | 170 MeV | # tracks >0 to >3 |
| FTT_mul_Tc | 417 MeV | # tracks >0 to >3 |
| FTT_mul_Td | 710 (2006: 600) MeV | # tracks >0 to >3 |
| FTT_mul_Te | 1000 (2006: 800) MeV | # tracks >0 to >3 |
| FTT_mul_Tf | 2500 (2006: 1500) MeV | # tracks >0 to >3 |
| FTT_mul_Tg | 5000 (2006: 3000) MeV | # tracks >0 to >3 |
| FTT_mul_Th | 2006: 5000 MeV | # tracks >0 to >3 |
| **Topological triggers** | | |
| FTT_topo_0 to FTT_topo_15 | similar to L1 TEs, but with refined binning | |
| **Invariant masses (only after 2006)** | | |
| FTT_M0-9 | invariant masses for two track combinations | |
| **Total sum over various quantities** | | |
| FTT_Qtot | Total charge | $Q_{tot}$ < -3 to >+3 |
| FTT_et_1 | total transverse energy | $E_T$ >1.0 (2006: 5.0) GeV |
| FTT_et_2 | | $E_T$ >2.0 (2006: 10.0) GeV |
| FTT_pt_1 | total transverse momentum | $P_T$ >1.0 GeV |
| FTT_pt_2 | | $P_T$ >2.0 GeV |
| FTT_Vap_1 | energy flow between | $V_{ap}$ >0.25 GeV |
| FTT_Vap_2 | different hemispheres | $V_{ap}$ >1.0 GeV |
| **Other trigger elements** | | |
| FTT_zvtx_acc | FTT z-Vertex found within acceptance region | -50 cm < $z_{vtx}$ <+50 cm |
| FTT_zvtx_histo | quality of FTT z-Vertex | grade 1-3 |

Table 4.2: FTT L2 trigger elements transmitted to the central trigger [73].

than possible at level 1. Then a fit in the $r$-$z$-plane is performed, using the information on the $z$-coordinate. By the means of this fit, information on $\theta$ is obtained on trigger level. Both fits are carried out by **D**igital **S**ignal **P**rocessors (**DSP**s). The track information is then used in order to calculate within 20 $\mu$s various trigger elements, which are summarised in tab. 4.2 [73].

### 4.2.3 Invariant masses on Level 3

The precise track information obtained at L2 is used on level 3 in order to calculate invariant masses of particles, with the help of additional information from the other trigger subsystems used for particle identification. Level 3 consists of a series of Power-PCs, each of which executes a different, speed-optimised resonance finder algorithms (see [74] for the current setup). The Power-PCs were not designed exclusively for the FTT, but are commercially produced and sold products. The finder algorithms are programmed in C. Time consuming calculations of for instance square roots or trigonometric functions

have to be avoided, in order to be able to deliver a decision within the time limit. The L3 trigger runs in the deadtime caused by the ongoing detector readout. Within 100 $\mu$s it has to arrive at a decision and has to transmit either a L3 KEEP or a L3 REJECT signal, with the latter one aborting the readout and resuming data taking. There are two crucial constrains on Level 3: First of all, the algorithms have to deliver a decision fast in order to abort the readout of the detector as soon as possible. As the detector readout takes 1 ms, the deadtime can be significantly reduced, if the trigger rejects events as fast as possible, in case an event is not interesting. Moreover it is important, that the resolutions of the parameters used as L3 input, are high enough. Only then, interesting events can be found and an event selection on trigger level is meaningful.

# 5 Performance of the FTT Level 2 system

As the FTT uses approximately only one fourth of the wire layers of the CJCs used in the offline track reconstruction, it is natural that the resolution of the FTT track is less precise compared to the one obtained in the offline reconstruction. In order to get an estimate for the selection power of the FTT level 3 system, when cutting on invariant masses, it is crucial to investigate the performance of the L2 system in terms of track resolutions and the overall stability of the L2 output used on L3. Hence, in this chapter, the resolution achieved for FTT L2 tracks is analysed over the full data taking period of 2005 and 2006. This information is then used to obtain a sample of runs, where the FTT L2 system was working reliably, and which can serve as basis for further investigations. In this thesis, the first systematic study of the FTT L2 track resolutions for data is presented.

## 5.1 Track resolution

The track resolution of the FTT tracks is determined with regard to the offline reconstructed tracks by comparing each track parameter of the offline reconstructed track with the track parameter the FTT has reconstructed for the very same track. In order to be able to account for technical problems reducing the nominal resolution power of the FTT, an iterative procedure was used in order to get a realistic estimate of the actual resolution.

### 5.1.1 Track Matching

A priori it is not known, which FTT reconstructed track corresponds to which offline reconstructed track. Therefore the tracks have to be paired using their parameters. For practical reasons this is done by calculating the distance $\mathcal{D}$ in $\kappa$-$\phi$[1] for every possible combination of pairs of offline and FTT tracks in an event, according to the following formula:

$$\mathcal{D} = \sqrt{\sum_{i=1}^{N} \frac{(x_{\text{offline}} - x_{\text{FTT}})_i^2}{w_i^2}}, \tag{5.1}$$

where the sum runs over the total number $N$ of all regarded trackparameters $x$, whose differences are weighted with a normalisation factor $w$, which accounts for the resolution, varying significantly depending on the regarded variable $x$, which can be either $\kappa$, $\phi$ or $\theta$.

After having calculated the distance $\mathcal{D}$ between each offline and each FTT track, the thus constructed track pairs are then arranged according to their respective distance $\mathcal{D}$ in $\kappa$-$\phi$. The two tracks with the smallest distance are taken to be the reconstructions of the same physical track and are removed from the list. Then the track pair which has the smallest distance of all remaining pairs of tracks is matched and so on until either no

[1] $\kappa$ in this context corresponds to $Q/P_T$, all other parameters from eq. 4.1 are set to 1.

| Parameter | Cut value |
|---|---|
| transverse momentum $P_T$ | $> 0.12$ GeV |
| polar angle $\theta$ | $> 20$ °<br>$< 160$ ° |
| distance of closest approach $d_{ca}$ | $\leq 2$ cm |
| Start radius $R_{start}$ | $\leq 50$ cm |
| Radial length $R_{length}$ | $\geq 10$ cm (for $\theta \leq 150°$)<br>$\geq 5$ cm (for $\theta < 150°$) |
| Number of hits in jet chambers $N_{CJChits}$ | $\geq 0$ |
| Vertex type | primary vertex |

Table 5.1: Cuts applied to offline tracks before they are included in the track matching and in the performance study. These cuts take pattern from the track selection, which is widely used in analyses in H1.

FTT or no offline track is left to be matched to a track of the other kind. In the track matching procedure only those offline reconstructed tracks were included, that fullfil certain selection criteria. The respective cuts on the included offline tracks are listed in table 5.1.

### 5.1.2 Selection of the analysed sample

The basic sample analysed contains 2005 and 2006 data. As the FTT was in 2005 still in the commissioning phase and as it is a new detector component, it was necessary to select among all the runs in 2005 and 2006 those where the FTT delivered reliable data. This was not always the case, as for example at the end of 2005, wrong L2 masks were loaded, which led to a wrong determination of track parameters.

Therefore the determination of the resolution was done in iteratively. In a first step the expected resolutions were used as normalisation factor $w$ in the track matching procedure. The matching was done in $\kappa$ and $\phi$, with $0.03 \times \kappa_{\text{offline}}$ and 5 mrad being the respective weighting factors, based on the resolutions specified as expectations in [75]. The weighting for $\kappa$ takes into account the strong dependence of $\sigma_\kappa$ on $\kappa$, which is discussed below in sec. 5.2.

After the track matching for each pair of matched tracks the difference between each offline and FTT reconstructed track parameter was calculated, e.g. $\Delta\phi = \phi_{\text{offline}} - \phi_{\text{FTT}}$. The mean value of these distributions as well as their RMS value[2] was then calculated for each run in 2005 and 2006 and used in order to characterise the performance of the FTT Level 2 system (see also section 5.3 for more details). Mean and RMS values did not vary much over the whole run period, only single runs or single luminosity fills were characterised by having mean and $\sigma$ values, that were not at all consistent with the average value of all analysed runs, they were off by several orders of magnitude (see fig. 5.7

[2]The value RMS (root mean square) was approximated using $\sigma_x = \sqrt{\frac{1}{N} \cdot \sum_{i=1}^{N} (x_i - x_{mean})^2}$, with N being the number of bins in the histogram, $x_i$ the i-th bin and $x_{mean}$ the mean value of all bins [76].

- 5.11). In some cases this malfunctioning of the Level 2 track reconstruction could be traced back to technical problems. As a consequence, these runs were excluded from the sample used in the determination of resolutions and only those runs were included in the analysis, that did not vary much from the average off all runs.

### 5.1.3 Determination of the resolutions

Resolutions are determined by subtracting the quantity that shall be analysed from a reference quantity. The width of the resulting distribution, i.e. its $\sigma$, is then used as a measure for the resolution of the respective quantity. In this analysis, the difference $\Delta x = x_{\text{offline}} - x_{\text{FTT}}$, with $x$ being each of the three track parameters $\kappa$, $\phi$ and $\theta$, was calculated. Two fit methods were then tested in order to determine the resolution of these parameters. As their distributions have quite large tails, a double Gaussian fit was applied to them, moreover an exponentially modified Gaussian was fitted to the data in order to account for the broad shoulders.

The formula for a double Gaussian distribution with an assumed identical mean $\mu$ is defined as:

$$G_{double}(\Delta x) = A_1 \cdot e^{-0.5 \cdot \frac{(\Delta x - \mu)^2}{\sigma_1^2}} + A_2 \cdot e^{-0.5 \cdot \frac{(\Delta x - \mu)^2}{\sigma_2^2}} \tag{5.2}$$

Another approach to fit a function with large tails is the exponentially modified Gaussian [77],[78], which is the convolution of a Gaussian distribution with an exponential decay. The modified "Gaussian" used here is defined as follows:

$$G_{modified}(\Delta x) = A \cdot e^{-0.5 \left| \frac{(\Delta x - \mu)}{\sigma} \right| \left( 1 + \frac{1}{1 + 0.5 \cdot \left| \frac{(\Delta x - \mu)}{\sigma} \right|} \right)} \tag{5.3}$$

The resolution of track parameters can be determined using the the weighted mean of the mean deviations of the double Gaussian distribution. It is defined as an effective $\sigma_{\mathit{eff}}$, calculated as:

$$\sigma_{\mathit{eff}} = \frac{A_1 \sigma_1 + A_2 \sigma_2}{A_1 + A_2} \tag{5.4}$$

An error on the resolution $\sigma_{\mathit{eff}}$ can be estimated applying the general laws of error propagation for a function $y = f(x_1, x_2, ...x_N)$, yielding

$$(\delta y)^2 = \sum_{i,j=1}^{N} \left( \frac{\partial y}{\partial x_i} \frac{\partial y}{\partial x_j} C_{ij} \right), \tag{5.5}$$

with $C_{ij}$ being the correlation matrix for the errors of the different fit parameters [79].

Using the uncertainty of the fit parameters and their correlation matrix, the uncertainty of the effective resolution can be calculated using

$$
\begin{aligned}
(\delta\sigma_{\mathit{eff}})^2 = &\frac{\partial\sigma_{\mathit{eff}}}{\partial\sigma_1}\frac{\partial\sigma_{\mathit{eff}}}{\partial A_1}C_{\sigma_1,A_1} + \frac{\partial\sigma_{\mathit{eff}}}{\partial\sigma_2}\frac{\partial\sigma_{\mathit{eff}}}{\partial A_2}C_{\sigma_2,A_2} \\
&+ \frac{\partial\sigma_{\mathit{eff}}}{\partial\sigma_1}\frac{\partial\sigma_{\mathit{eff}}}{\partial A_2}C_{\sigma_1,A_2} + \frac{\partial\sigma_{\mathit{eff}}}{\partial\sigma_2}\frac{\partial\sigma_{\mathit{eff}}}{\partial A_1}C_{\sigma_2,A_1} \\
&+ \frac{\partial\sigma_{\mathit{eff}}}{\partial\sigma_1}\frac{\partial\sigma_{\mathit{eff}}}{\partial\sigma_2}C_{\sigma_1,\sigma_2} + \frac{\partial\sigma_{\mathit{eff}}}{\partial A_1}\frac{\partial\sigma_{\mathit{eff}}}{\partial A_2}C_{A_1,A_2} \\
&+ \left(\frac{\partial\sigma_{\mathit{eff}}}{\partial\sigma_1}\right)^2 C_{\sigma_1,\sigma_1} + \left(\frac{\partial\sigma_{\mathit{eff}}}{\partial\sigma_2}\right)^2 C_{\sigma_2,\sigma_2} \\
&+ \left(\frac{\partial\sigma_{\mathit{eff}}}{\partial A_1}\right)^2 C_{A_1,A_1} + \left(\frac{\partial\sigma_{\mathit{eff}}}{\partial A_2}\right)^2 C_{A_2,A_2}
\end{aligned}
\tag{5.6}
$$

$$
\begin{aligned}
(\delta\sigma_{\mathit{eff}})^2 = &\frac{A_1 A_2\,(\sigma_1-\sigma_2)}{(A_1+A_2)^3}\left(C_{\sigma_1,A_1} - C_{\sigma_2,A_2}\right) \\
&+ \frac{(\sigma_1-\sigma_2)}{(A_1+A_2)^3}\left(A_2^2 C_{\sigma_2,A_1} - A_1^2 C_{\sigma_1,A_2}\right) \\
&+ \frac{1}{(A_1+A_2)^2}\left(A_1^2 C_{\sigma_1,\sigma_1} + A_1 A_2 C_{\sigma_1,\sigma_2} + A_2^2 C_{\sigma_2,\sigma_2}\right) \\
&+ \frac{(\sigma_1-\sigma_2)}{(A_1+A_2)^4}\left(A_2^2 C_{A_1,A_1} + A_1 A_2 C_{A_1,A_2} + A_1^2 C_{A_2,A_2}\right)
\end{aligned}
\tag{5.7}
$$

The error of the fit parameter $\sigma$ for the modified Gaussian fit is taken to be the uncertainty on the thus extracted resolution. The usage of the modified Gaussian is justified because the fit formula has the capability of describing the broad tails of the distribution consistently compared to the double Gaussian with the advantage of having only three free parameters. Also, the $\chi^2$/ndf values are more or less compatible for both fits.

To determine the resolutions, the sample containing only the runs with parameters close to the average was analysed. As a further constraint, it was required, that only three tracks had been detected in the CJCs. Firstly, in order to ensure the definiteness of the track matching procedure. Secondly, because $D^*$ mesons decay into three particles. For $\theta$ a constant background was used as additional free parameter in the fit, as there was a small fraction of tracks, which were not fitted in $\theta$ on FTT level, only in $\phi$ and $\kappa$. This can happen when there was not enough charge deposited on the wires, so that it was not possible to extract a $z$-coordinate using charge division. The tracks without $\theta$-measurement are the cause for uncorrelated entries in the histogram for the $\theta$ distribution. Allowing for an additional fit parameter describing this constant background, yields a better description of the distribution when fitting and should be therefore applied. The resolution then tends to be better with that additional parameter, as the flat constant background is not longer interpreted as shoulders of the distribution and is not tried to be fitted using the Gaussians anymore.

As can be seen from the summary table 5.2 and figures 5.1 for 2005 data and 5.2 for 2006 data, both fits yield comparable results for the resolutions in both data taking pe-

| Resolution measured in... | | $\Delta\phi$ [mrad] | $\Delta\theta$ [mrad] | $\Delta\kappa/\kappa$ [%] |
|---|---|---|---|---|
| **Simulation FTTemu [65]** (factor arises from different definition of the Gaussian, see text) | $\sigma_{\mathit{eff}} \times 2$ | 2.2 | 88 | 3.8 |
| **Double Gaussian** | $\sigma_{\mathit{eff}}$ (2005) | 4.40±0.01 | 134.0±0.4 | 4.079±0.002 |
| | $\sigma_{\mathit{eff}}$ (2006) | 4.11±0.01 | 118.7±0.2 | 3.968±0.002 |
| | $\sigma_{\mathit{eff}}^{2006}$ ($P_T$ >1 GeV) | 2.35±0.07 | 111.98±0.91 | 4.18±0.01 |
| **Modified Gaussian** | $\sigma$ (2005) | 3.33±0.00 | 118.6±0.2 | 2.746±0.003 |
| | $\sigma$ (2006) | 3.17±0.00 | 105.26±0.07 | 2.644±0.002 |
| | $\sigma^{2006}$ ($P_T$ >1 GeV) | 1.88±0.01 | 100.6±0.2 | 3.297±0.007 |
| **used as normalisation factor in eq. 5.1 later on** | $\sigma_{weight}$ | 5.5 | 145 | 2.75 |

Table 5.2: Comparisons of resolutions for 2005 and 2006 data as measured herein and the values expected from simulations studies with the FTT simulation programme FTTemu. While the resolution of the data was determined using a three track sample, the simulation studies used a sample of diffractive J/Ψs events, which contain exactly two high $P_T$ tracks.

riods. Fitting problems are most prominent for the $\theta$ distribution, which does not only suffers from a constant background, but is also distinctively asymmetric. One Gaussian is clearly not enough to describe the data and even the double Gaussian has sometimes problems describing the distributions, which is reflected in the fact, that the functions underestimate the height of the distributions. The shapes of the distributions are not purely Gaussian because they are object to many systematic influences, some of which will be discussed in the next section. It is worth noting, that the resolutions are better for the 2006 data compared to the 2005 data – obviously, the performance of the FTT could be improved during this period. The resolutions obtained for 2006 with real track data from the FTT are consistent with what was expected from Monte Carlo simulation studies ([54], [65][3]). Only for the $\phi$ resolutions a deviation of a factor of about 2 can be observed. They result from the difference in the data samples analysed. As the mentioned simulation studies used an diffractive J/Ψ sample in the leptonic decay channel (J/Ψ → μμ, J/Ψ → ee) with exactely two tracks, this sample was dominated by high $P_T$ tracks (∼80% having a $P_T > 1$ GeV), while these high momentum tracks only made up ∼10% of the data sample analysed here. Since high momentum tracks suffer much less from multiple scattering, the resolution of their track parameters tend to be better in $\phi$. Consequently, when comparing only the high $P_T$ subsample of 2006 with the simulation study, both yield similar results (see tab. 5.2). Further influences on the resolution of the track parameters will be studied in the next section.

[3]In order to compare the resolutions, a factor of two had to be multiplied to the resolutions obtained in the MC studies, because in contrast to the definition used in here, the Gaussian in [65] was defined without the factor 0.5 in the exponent, i.e. as $G_{double}(\Delta x) = A_1 \cdot \exp\{-\frac{(\Delta x-\mu)^2}{\sigma_1^2}\} + A_2 \cdot \exp\{-\frac{(\Delta x-\mu)^2}{\sigma_2^2}\}$

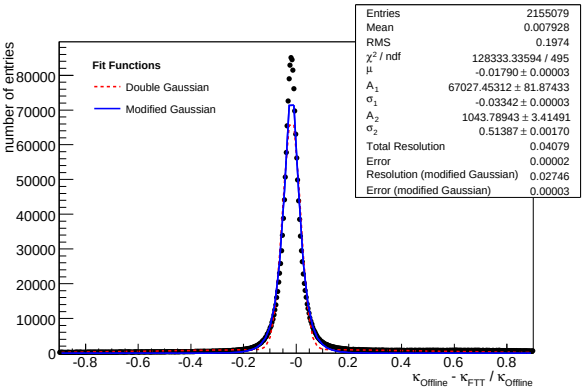


a) resolution in $\kappa$ (data 2005)

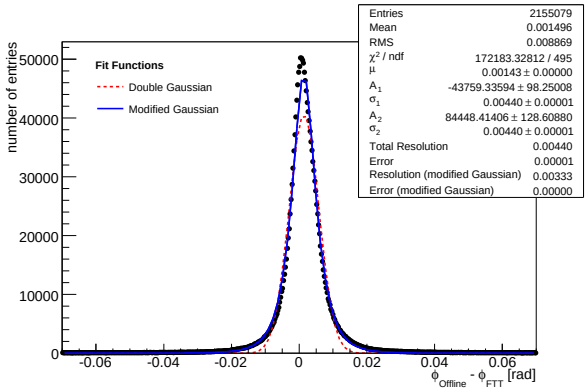


b) resolution in $\phi$ (data 2005)

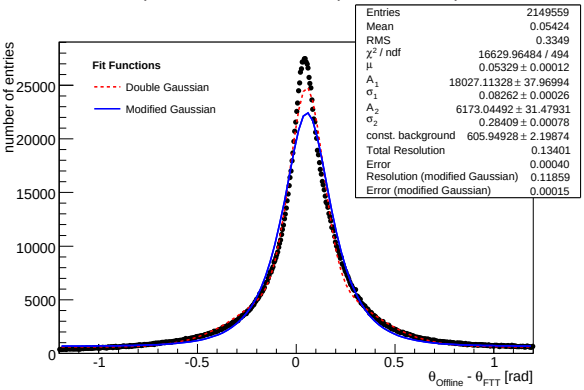


c) resolution in $\theta$ (data 2005)

Figure 5.1: Resolution of the FTT measured track parameters $P_T^{FTT}$ (a), $\phi^{FTT}$ (b) and $\theta^{FTT}$ (c) relative to the offline reconstructed parameters $P_T^{offline}$, $\phi^{offline}$ and $\theta^{offline}$ for a 2005 sample containing exactly three tracks.

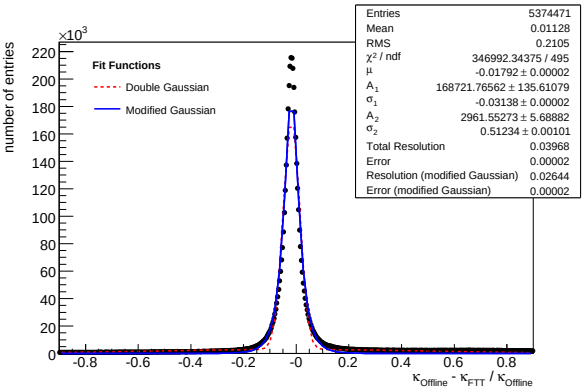


a) resolution in $\kappa$ (data 2006)

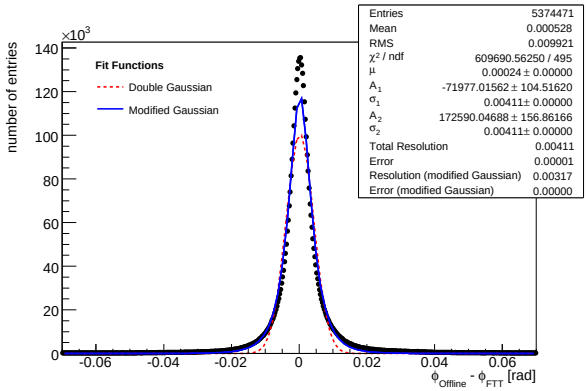


b) resolution in $\phi$ (data 2006)

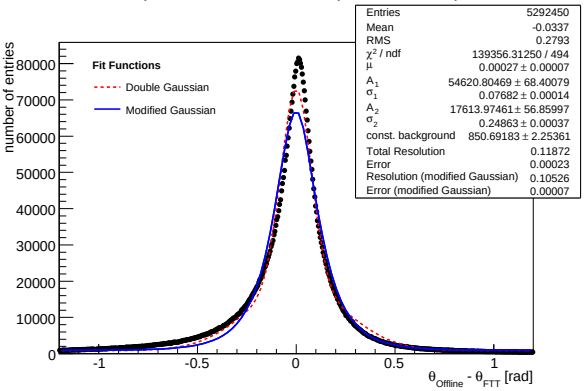


c) resolution in $\theta$ (data 2006)

Figure 5.2: Resolution of the FTT measured track parameters $P_T^{FTT}$ (a), $\phi^{FTT}$ (b) and $\theta^{FTT}$ (c) relative to the offline reconstructed parameters $P_T^{offline}$, $\phi^{offline}$ and $\theta^{offline}$ for a 2006 sample containing exactly three tracks.

## 5.2 Influences on the resolution of tracks

The above mentioned parametrisation of tracks as helixes is valid only in first approximation when effects of multiple scattering, energy loss and inhomogeneities of the magnetic field are neglected. These can significantly influence the measurement of track parameters, and are also the reason why the $\Delta x = x_{off} - x_{\mathrm{FTT}}$ distributions are not described by a single Gaussian, but rather by a double or multiple Gaussian. The most important factors having impact on the resolutions of the track parameters shall be studied in the following using the FTT track parameter resolutions.

### 5.2.1 Multiple Scattering

While traversing the beam pipe and the walls of a tracking chamber a charged pointlike particle can encounter Coloumb scatterings on a massive point charge. Several subsequent scatterings lead to a significant deviation from the original path of the particle. This is called multiple scattering and sums up in the way of many relatively small random changes of the direction of flight [80]. Multiple scattering can be approximated using a Molière distribution [8]:

$$\theta_{plane}^{RMS} = \frac{13.6\mathrm{MeV}}{\beta c P} z \sqrt{x/X_0}\,[1 + 0.038 \ln x/X_0] \tag{5.8}$$

with $P$, $\beta c$ and $z$ being the momentum, velocity and the charge number of the incident particle and $x/X_0$ the thickness of the scattering medium in radiation lengths. Fig. 5.3 shows the impact of multiple scattering on the resolutions of FTT tracks. The plots depict the difference $\Delta\phi = \phi_{\mathrm{offline}} - \phi_{\mathrm{FTT}}$ for different ranges in $P_T$: Whereas on the left hand side $\Delta\phi$ is shown only for tracks with a transverse momentum of the offline tracks of 100 MeV $< P_T <$ 170 MeV, the distribution on the right hand side is restricted to tracks having a transverse momentum of 1 GeV $< P_T <$ 2.5 GeV. The respective resolutions vary significantly due to the effects of multiple interaction: Whereas the low $P_T$ sample shows an effective resolution of 8.87 $\pm$ 0.22 mrad, the high $P_T$ sample has with 2.32 $\pm$ 0.09 mrad a resolution that is approximately a factor of 4 better[4]. Both samples were restricted to contain only negatively charge tracks due to the influence of the missing energy loss correction (see section 5.2.3). For the low $P_T$ sample the charge conjugate distribution was plotted as solid line to explicitly show, that the distributions in principle look the same, but are only shifted in their means.

### 5.2.2 Intrinsic spatial resolution: Number of linked segments

Additional to the uncertainties arising through multiple scattering, there exists also an error on the track measurements resulting from the intrinsic spatial resolution. For N $\geq$ 10 uniformly spaced position measurements made along a trajectory in a uniform medium, the following approximation holds [8]:

$$\delta\kappa_{res} = \frac{\epsilon}{L'^2}\sqrt{\frac{720}{N+4}} \tag{5.9}$$

[4]Both resolutions are determined with a double gaussian fit, the modified gaussian delivers as results 6.98 $\pm$ 0.02 mrad and 1.86 $\pm$ 0.00 mrad

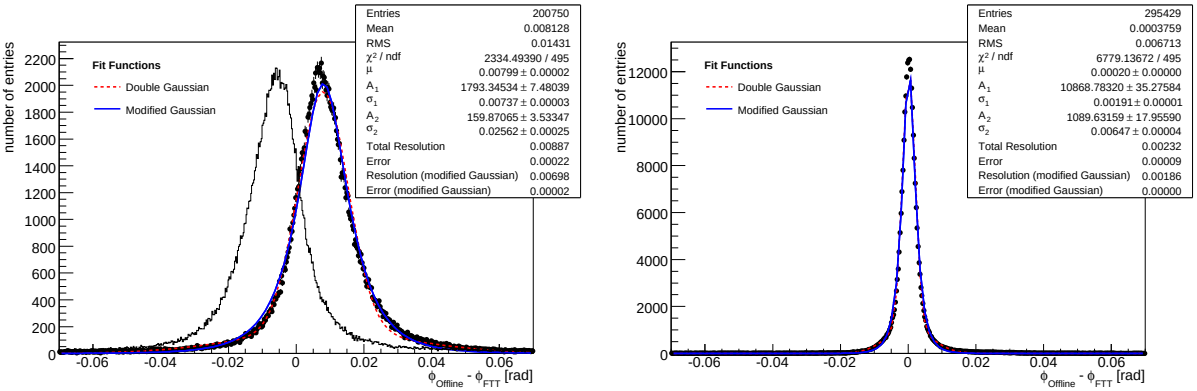


a) resolution in $\phi$ for $100 < P_T < 170$ MeV

b) resolution in $\phi$ for $1000 < P_T < 2500$ MeV

Figure 5.3: The effect of multiple scatterings on the resolution of the track parameter $\phi$. The low $P_T$ sample on the left hand side has a worse resolutions than the high $P_T$ sample on the right hand side. In addition the means of the distributions for positively and negatively charged tracks are also shifted depending on the charge of the measured particle, as explained in sec. 5.2.3. Therefore only the distributions for negatively charged tracks are fitted. The distribution for the positively charged tracks is additionally shown for the low $P_T$ sample on the left hand side.

with the track curvature $\kappa_{res}$, the projection length of the track onto the bending plane $L'$, $N$ the number of position measurements and $\epsilon$ the measurement error for each point, perpendicular to the trajectory.

At the FTT the influence of the intrinsic spatial resolution can be measured quite easily: The number of segments linked to an actual track can vary from 2 to 4. Each of these linked segments contains at least three hits, so that depending on the number of linked segments a minimum of 6 to a maximum of 20 hits have been used in FTT track reconstruction. Therefore, one can study the influence of the intrinsic spatial resolution by comparing the resolutions for tracks with different numbers of linked segments. This is shown as an example in fig. 5.4 for the parameter $\kappa$: The plot on the left hand depicts the distribution for tracks created from two linked segments, the obtained resolution amounts to 5.33 $\pm$ 0.04 %. The resolution for tracks with four linked segments is significantly better: The resolution of the distribution on the right hand side is 2.08 $\pm$ 0.05 %[5].

A systematic approach to describe the combined influence of both of these effects, multiple scattering and the intrinsic spatial distribution, was introduced in [81]. Based on this approach, a theoretical prediction for the angular and momentum resolutions was formulated in [82] for the H1 tracker system, including the FTT and using eq. 5.8 and 5.9. Fig. 5.5 shows the comparison of these predictions with the resolutions determined in this analysis. The experimental measurement lies below the theoretical expectation for the FTT, which can be qualitatively understood, when taking into account, that the measured resolutions were obtained in comparison to the CJC tracks. The resolutions for the CJC and FTT tracks are correlated, because they are in principle reconstructed from the same hits. That implies that the CJC and FTT measured track parameters deviate from the parameters of the genuine physical trajectory in a correlated manner, that is they either

[5]Both resolutions are determined with a double gaussian fit, the modified gaussian delivers as results 3.74±0.02% and 1.482±0.006%

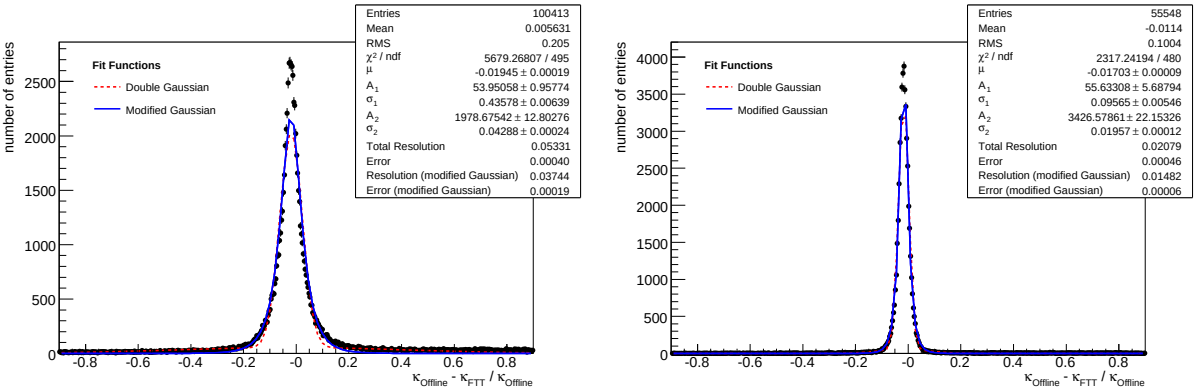


a) resolution in $\kappa$ for two linked segments

b) resolution in $\kappa$ for four linked segments

Figure 5.4: Resolutions for $\kappa$ depending on the number of segments, that were linked in the track finding procedure.

both overshoot the genuine value or both underestimate it. An experimentally obtained resolution from a comparison of FTT with CJC tracks should thus yield a better resolution than expected theoretically for the absolute resolution of the FTT tracks in comparison with the genuine trajectories. Apart from this effect, the experimental resolutions agree nevertheless reasonably well with the shape of the predicted distributions.

### 5.2.3 Missing energy loss corrections: Charge of the track

Relativistic particles passing through the jet chambers loose energy due to ionisation and atomic excitation processes. The mean rate of their energy loss $\frac{dE}{dx}$ measured in $\left[\frac{\text{MeV cm}^2}{\text{g}}\right]$ is described by the Bethe-Bloch formula [8]:

$$-\frac{dE}{dx} = Kz^2\frac{Z}{A}\frac{1}{\beta^2}\left[\frac{1}{2}\ln\frac{2m_ec^2\beta^2\gamma^2T_{max}}{I^2} - \beta^2 - \frac{\delta}{2}\right] \tag{5.10}$$

Here $z$ is the charge of the incident particle, $A$ $\left[\frac{\text{g}}{\text{mol}}\right]$ the atomic mass of the absorber, $I$ the mean excitation energy, $T_{max}$ the maximum kinetic energy that can be imparted to a free electron in a single collision and $\delta$ takes into account density effect corrections to ionisation energy losses. $K = 4\pi N_A r_e^2 m_e c^2$ contains Avogadro's number $N_A$, the classical electron radius $r_e$ as well as the electron mass $m_e$.

Due to the above described energy loss the curvature of track tends to rise as they pass through the chamber. That means that a trajectory has a measurably higher $\kappa$ values after its passage through the jet chambers compared to the $\kappa$ it had when entered the CJCs. For the offline reconstruction this energy loss is taken into account while it is not regarded in the FTT online reconstruction. The deviation from the incident trajectory due to energy losses is also reflected in a shift from the incident $\phi$ direction to higher or lower angles for oppositely charge tracks. Thus, as demonstrated in fig. 5.6, for FTT reconstructed tracks, which are not corrected for $\frac{dE}{dx}$ effects, there is a deviation expected in $\Delta\phi$ for oppositely charged track compared to the offline measured track. It can indeed be observed, when comparing the means for the $\Delta\phi$ distributions for negatively and positively charged tracks. Due to the $\frac{1}{\beta^2}$ dependence of the Bethe-Bloch formula this effect can be most prominently observed for low transverse momenta. In fig. 5.3 this is

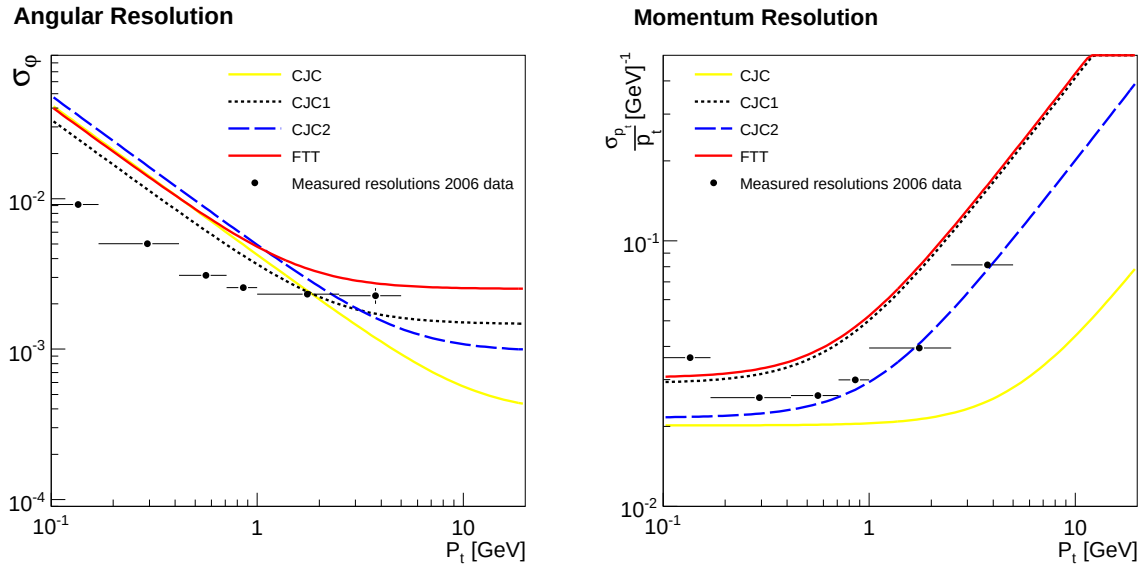


a) theoretical and measured angular resolutions

b) theoretical and measured momentum resolutions

Figure 5.5: Comparison of the theoretical prediction for the resolution in $\phi$ and the relative resolution in $\kappa$ to the measured values. The experimentally obtained resolutions for the FTT tracks lie below the theoretical curve (taken from [82]) as they were determined relative to the CJC tracks, whose measurements are correlated with those of the FTT reconstructed tracks. Thus a part of the FTT track resolution is not taken into account, but absorbed in the CJC track resolution, which was used as normalisation. As a consequence, the measured FTT resolution underestimates the real resolution of the FTT and deviations of the theoretical from the experimental curves are expected.

demonstrated, where the $\Delta\phi$ distribution is shown for positively (solid line) and negatively (fitted dots) charged tracks: While the mean for positively charge tracks measures $\mu$ = -6.43±0.02 mrad, the one for negatively charged tracks measures $\mu$ = 7.99±0.02 mrad. This effect is still visible, when plotting the distribution for negatively and positively charged tracks separately, but not as pronounced. Therefore for an inclusive $P_T$ sample the systematic shift can be seen best, when plotting the means of the $\Delta\phi$ distributions for a large number of samples. This is done in fig. 5.10, where the mean, as obtained by the modified Gaussian fit of the distribution for negatively and positively charged tracks is plotted against the respective run number for the beginning of 2006. The large deviations from the otherwise homogenous behaviour of the means arises from technical problems, however for most runs the expected systematic shift of the means for negatively (left hand side) and positively charged tracks (on the right) can be observed. To apply energy loss corrections during the FTT online reconstruction is technically not possible, because there is not enough time for the extensive calculation that would be needed. Fig. 5.10 was created in the course of the analysis of the time dependence of the FTT performance, whose results shall be described in the following section.

## 5.3 Performance of the Level 2 system in 2005 and 2006

In order to be able to monitor the FTT L2 system and to select runs with sufficient quality for analysis purposes, a programme was developed to determine various parameters of the L2 performance for every run separately. The thus analysed quantities included the difference in number of reconstructed tracks, normalised to the number of offline

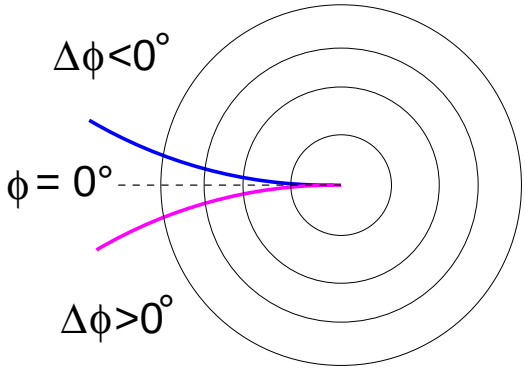


Figure 5.6: Schematic sketch of the influence of missing energy loss corrections: Shown are the four layers of the FTT as circles and three track passing them. One is an "ideal" high $P_T$ track, which traverses at $\phi$=0° without energy losses (dashed line). Thus it is a straight line, which does not change its direction. This is however not true for real tracks, as they undergo energy losses, their curvatures rise, they are bend according to their charge either to the left or to the right. This is the case for the thick lines, representing real tracks of opposite charge, which are attributed a lower or higher $\phi$ value depending on their charge, $\Delta\phi \gtrless 0°$. While offline the bend tracks are reconstructed as the original track, the dashed line, with the help of energy loss correction, the FTT can reconstruct only the bend trajectories.

tracks and technical quantities like the number of failing DSP fitters (used in the track fitting procedure on L2) due to data transfer errors. Monitored were also the distributions $\Delta x = x_{\text{offline}} - x_{\text{FTT}}$ for the track parameters $\phi$, $\theta$ and $\kappa$. In order to be able to compare them among different runs, the mean values for the distributions as well as the $\sigma$ values, i.e. the resolutions of the respective parameters, were determined for each run. This was done also as a function of charge and transverse momentum. To determine the resolutions, the modified Gaussian was used, because it has three instead of five free parameters and is thus more likely to converge fast. Therefore it is very convenient to use the modified Gaussian for applications, where a large number of distributions has to be fitted without the possibility of explicit supervision.

With the help of this monitoring programme the performance of the FTT Level 2 system could be investigated time dependend. This was done for the second half of 2005 and for the first half of 2006. The system was found to run stable for most of the times. Periods with unreliable reconstruction due to changed system parameters could be identified. Additionally the impact of changed FTT settings, e.g. new calibrations, on the track parameters could be monitored and quantified. Examples are shown in fig. 5.8 to 5.11, where several parameters are plotted against the run number. Fig. 5.8 shows, how many of the found tracks were not fitted on L2, because of data transfer errors to and from the DSP fitters. While the percentage of these non-fitted tracks was quite large at the beginning of the monitored run period, these problems could be solved during 2005, so that their number dropped to the per mille level.

Another improvement was made due to a new calibration for drift vectors and wire positions, that was introduced starting with run $\backsim$435525. The impact of this calibration can be seen in fig. 5.8, where the mean value of the $\Delta\phi$ as well as the means of the $\Delta\kappa$

distribution for positively and negatively charged tracks is plotted against the runs in 2005. Large deviations for the average values are a sign for unstable FTT performance and technical problems. For instance, the spikes for the runs after 436500 are the result of wrong masks that were used in the L2 system. However, systematic changes can also be observed: The new calibration established after run $\backsim$435525 resulted in a mean value of $\phi$ closer to zero than before. Additionally systematic deviations in the mean of the $\kappa$ distribution for positively and negatively charged tracks could be eliminated.

Another result of this time-dependent long-term study of the FTT performance was that the reconstruction of $\theta$ could be much improved in 2005 and in 2006. This is shown in fig. 5.9, where the mean and $\sigma$ values for $\theta$ are plotted against the run numbers of 2005 and 2006. The improvements concerning the mean value of the distribution were achieved due to a new calibration introduced in 2005, those concerning the $\sigma$ value are due to the use of the right z-vertex in the fit which determined $\theta$. The missing energy loss corrections, already discussed in sec. 5.2.3, result in a systematic shift of the means for the $\Delta\phi$-distributions of positive and negatively charged tracks, shown in fig. 5.10. The spikes in the distribution for the run ranges between 446000 and 448000 are due to the use of a wrong vertex position within the Level 2 system, which again is an example, of how technical problems of the L2 system can affect the L2 performance and how a continuous monitoring with the programme developed can allow to identify technical problems.

The relative fraction of tracks found and reconstructed by the FTT in comparison with offline reconstructed tracks varies with the electron beam current, since the single hit efficiency of the FTT and thus also the track finding efficiency depends strongly on the amount of charge inside the chamber. The higher the luminosity, the lower the track finding efficiency due to charge screening in the CJCs. This is shown in 5.11, where the dots and the axis on the right hand side describe the electron beam current in units of mA, while the bars represent the average percentage of offline tracks not found by the FTT, plotted against the run number. This fraction of tracks not found by the FTT of 15% in average is due to the fact, that here only the bare difference of the number of tracks was calculated. There were no cuts applied on offline tracks to filter out only those within the FTT acceptance, therefore this fraction includes also the fraction of tracks outside the FTT acceptance. Other definitions of the track samples to be compared in number only lead to differences in the overall normalisation, their shape and their dependence on the electron beam current is always the same.

For all the distributions shown, it is worthwile noticing, that the obtained resolutions are slightly worse for all the variables due to the fact, that the algorithm matches the tracks of each event regardless of the multiplicity of an event. As the quality of the FTT track reconstruction tends to decrease with a rising number of tracks, the resolutions for the total data samples of 2005 and 2006 are slightly worse than those obtained with a sample, where the number of tracks was restricted to be three, as done in sec. 5.1.3. With the help of the monitoring programme, a data sample could be selected, that contained all the stable FTT runs for 2005 and 2006. This was achieved by requiring for each run, that it should contain more than 500 events and the above described parameters, i.e. the number of failing DSP fitter, the mean and $\sigma$ of the track parameters and the fraction of tracks not found, should not exceed a value too far away from the average value of all

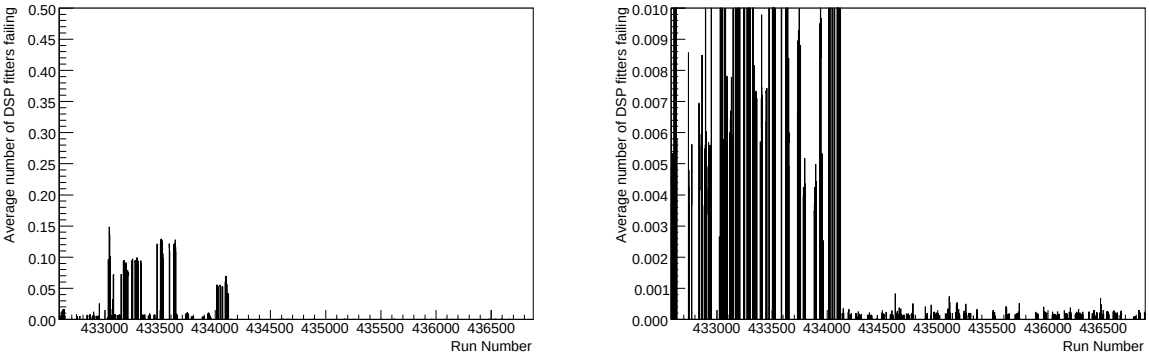


a) fraction of tracks not being fitted

b) fraction of tracks not being fitted (zoomed in)

Figure 5.7: Technical problems due to data transfer errors to and from the DSP fitters were solved in the course of the year 2005.

| **FTT parameter** | **unit** | **Cut applied in 2005** | **Cut applied in 2006** |
|---|---|---|---|
| fraction of data transfer errors to DSP fitters | % | $\leq 20$ | $\leq 0.2$ |
| $\lvert\kappa^{mean}\rvert$ | $[\mathrm{GeV}^{-1}]$ | $\leq 0.0225$ | $\leq 0.0225$ |
| $\sigma_\kappa$ | $[\mathrm{GeV}^{-1}]$ | $\leq 0.04$ | $\leq 0.04$ |
| $\lvert\phi^{mean}\rvert$ | [rad] | $\leq 0.003$ | $\leq 0.0008$ |
| $\sigma_\phi$ | [rad] | $\leq 0.011$ | $\leq 0.0115$ |
| $\lvert\theta^{mean}\rvert$ | [rad] | $\leq 0.15$ | $\leq 0.07$ |
| $\sigma_\theta$ | [rad] | $\leq 0.2$ | $\leq 0.18$ |
| $\frac{\#\mathrm{tracks}^{offline}-\#\mathrm{tracks}^{FTT}}{\#\mathrm{tracks}^{offline}}$ | % | $\leq 30$ | $\leq 23$ |

Table 5.3: Selection cuts for stable FTT runs.

runs. The values used for 2005 and 2006, respectively, are listed in tab. 5.3. Some of the cuts applied were changed for 2006, because solved technical problems allowed for a harder cuts without a loss of statistics.

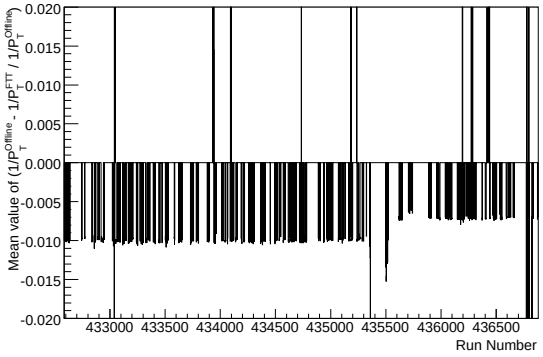


a) Mean value of $\kappa$ per run number (neg. tracks)

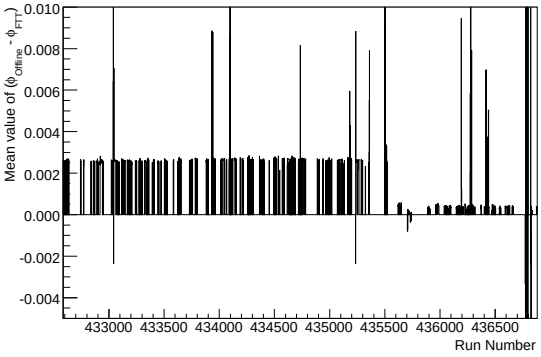


b) Mean value of $\phi$ as function of run number

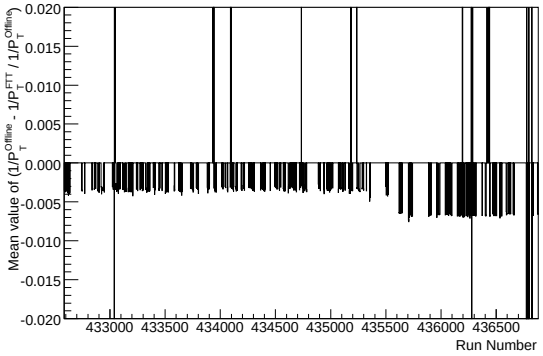


c) Mean value of $\kappa$ per run number (pos. tracks)

Figure 5.8: The impact of the improved calibration introduced with run $\backsim$435525: It resulted in a mean value of $\phi$ closer to zero than before, additionally systematic deviations in the mean of the $1/P_T$ distribution for positively and negatively charged tracks were eliminated.

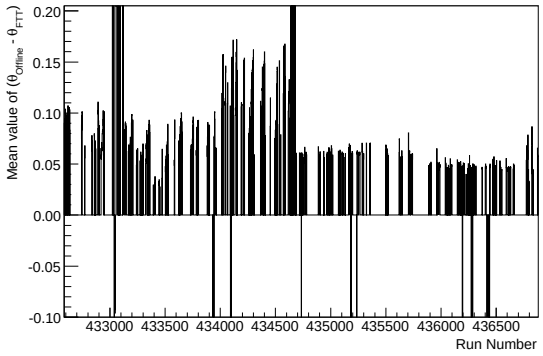


a) Mean value of $\theta$ per run number (2005 data)

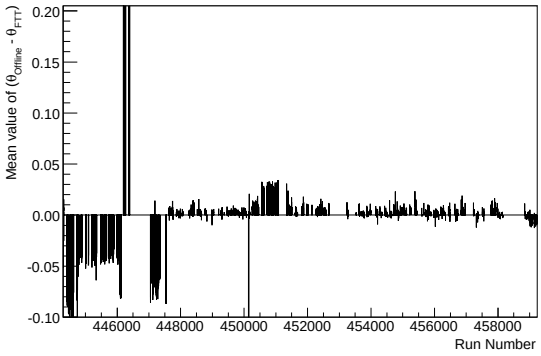


b) Mean value of $\theta$ per run number (2006 data)

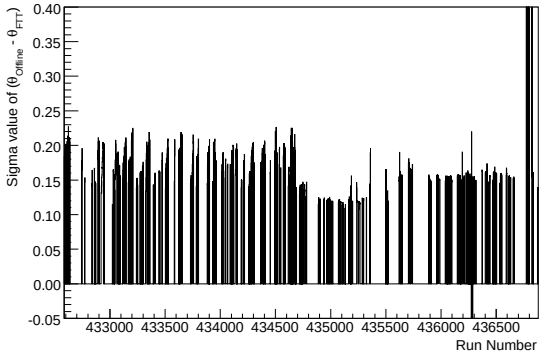


c) Resolution of $\theta$ per run number (2005 data)

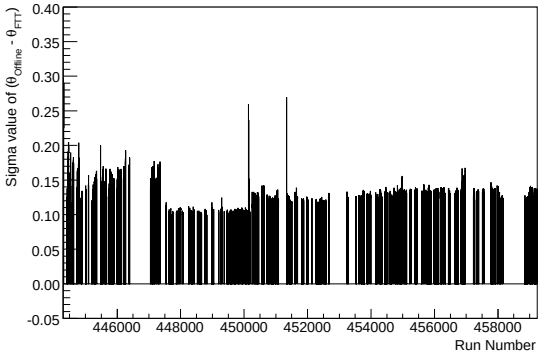


d) Resolution of $\theta$ per run number (2006 data)

Figure 5.9: The reconstruction of $\theta$ could be much improved in 2005 and in 2006.

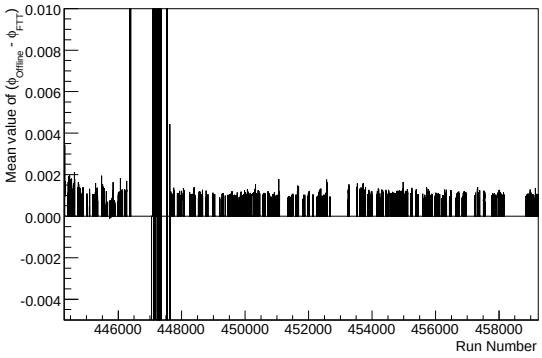


a) Mean value of $\phi$ per run number (neg. tracks)

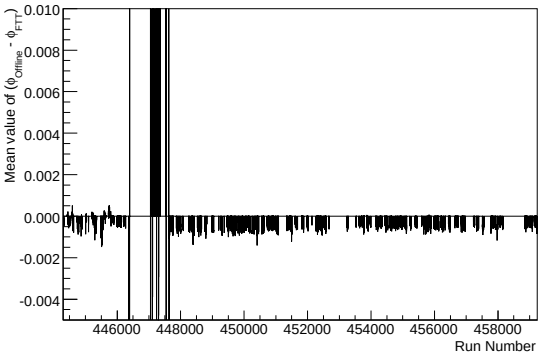


a) Mean value of $\phi$ per run number (pos. tracks)

Figure 5.10: The missing energy loss corrections result in a systematic shift of the means for the $\Delta\phi$-distributions of positive and negatively charged tracks.

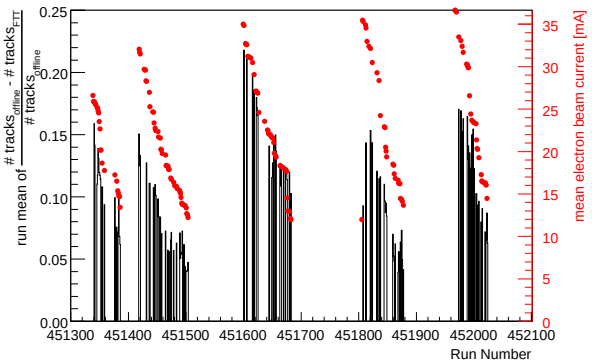


Figure 5.11: The relative fraction of FTT reconstructed track (bars, left axis) in comparison with offline reconstructed tracks varies with the electron beam current (dots, right axis).

# 6 Online event selection of $D^*$ mesons

In order to judge the usability of the FTT for data taking and triggering purposes, its capability of selecting $D^*$ mesons was analysed in terms of selection efficiencies and rate reductions. Two kinematic regimes were studied separately, namely DIS (in 2005 data) and photoproduction (in 2006 data). In the following, first of all the definitions of selection efficiencies and rate reductions as well as experimental methods to determine them are introduced. Then the results of the investigations carried out in this thesis are presented in two sections. The first one covers the DIS regime; it introduces the applied events selection and presents findings on the efficiencies of the trigger elements applied in DIS. Furthermore, investigations on a possible FTT trigger on level 2 for DIS events are presented, which include also a study of the quality of the FTT trigger elements encoding the multiplicity above the respective $P_T$ thresholds. The second section of this chapters gives an overview about studies on how to trigger $D^*$ mesons in untagged photoproduction. It starts of with a level 1 analysis, which led to an improved L1 trigger setup. Subsequently, the currently implemented L2 photoproduction trigger setups are discussed. All of these studies are results of this thesis. This is followed by a study on the performance of L3: In this thesis, the resolution of the invariant mass $\Delta M$ and $m_{D^0}$ is determined for the first time in data. Also discussed are efficiencies and rate reductions on Level 3.

## 6.1 Efficiencies and Rate Reductions: Definition and Determination

A trigger system designed to select events for permanent storage is characterised by two important variables: efficiency $\epsilon$ and rate reduction $\mathcal{R}$. The former one determines the percentage of signal events the trigger selects for storage in comparison to those it should have actually selected. The latter one determines the selectivity of the trigger, that is how many events are rejected in comparison to the total number of events the trigger has been confronted with. Naturally, it is desired to reject as many events as possible on trigger level while keeping all signal events. Thus, a high rate reduction accompanied by a high efficiency characterises a trigger with an optimal performance. The efficiency $\epsilon$ is defined by the following relation:

$$\epsilon = \frac{\#\text{Triggered } \mathbf{signal} \text{ events}}{\#\text{total } \mathbf{signal} \text{ events}} \tag{6.1}$$

The question left open by the above definitions is how the number of total (signal) events is to be determined. It is clear, that both, $\epsilon$ and $\mathbf{R}$, have to be measured in comparison to a well-defined sample. How to select this sample is not trivial and is described in the following: The recorded data at H1 do not constitute a well defined basic population nor even an unbiased sample. The reason for this is simply that events can be rejected on each trigger level and thus are not stored. When defining a well-defined subsample, two methods are applicable: the absolute and the relative determination of efficiencies.

Absolute efficiencies are determined using a sample of signal events triggered by so-

called monitor triggers. Thus, it is ensured, that a random but nevertheless well-defined subsample of the total data is taken as basis of efficiency determinations. Absolute efficiencies are used in cross section measurements to estimate the true total number of signal events in contrast to the observed number of signal events, which is lower due to trigger inefficiencies. The monitor triggers used should be independent, i.e. they should use information from other detectorsubsystems than the subtrigger to be analysed. Henceforth, three different sets of these monitor triggers are used in order to obtain well-defined data samples for the determination of the absolute efficiency. They are described in table 6.1. At H1, due to the prescale strategy, the following definition for absolute efficiencies is used:

$$\epsilon_{abs} = \frac{\text{subtrigger}_{raw} \,\&\&\, \text{monitortrigger}_{act} \,\&\&\, \text{eventselection}}{\text{monitortrigger}_{act} \,\&\&\, \text{eventselection}} \tag{6.2}$$

Here, raw expresses the fact, that a trigger triggered and actual means, that this trigger decision was actually the basis on which the event was kept. This is done in order to interpret the effects of prescales not as trigger inefficiencies.

Efficiencies can also be determined relatively, that is in comparison to a sample selected by a trigger realised on the same or a preceding trigger level. This method is used, when an existing trigger is tested for possibilities to improve it with additional trigger conditions. The efficiency of the trigger elements which are to be implemented is then examined relatively to the sample selected by the existing trigger or a trigger on a preceeding trigger level. This relative efficiency gives then an estimate of how many signal events would be kept, if the analysed additional trigger requirements would be used. For the measurement of the relative efficiency of a subtriggers it is fully sufficient to require a *raw* trigger bit:

$$\epsilon_{rel} = \frac{\text{additionaltriggerconditions}_{raw} \,\&\&\, \text{subtrigger}_{raw} \,\&\&\, \text{eventselection}}{\text{subtrigger}_{raw} \,\&\&\, \text{eventselection}} \tag{6.3}$$

The errors for both, relative and absolute, efficiencies are calculated using Bayes' Theorem, as implemented in the analysis software package ROOT [76]. The errors are assigned on a 68.3% confidence level. The exact procedure along with a discussion of the advantages of this method in comparison to using Poisson or binominal errors is described in detail in [83].

Rate reductions express, how many events are rejected already on trigger level. In multi-level trigger systems they can only be estimated using special transparent runs, where the subsequent trigger levels are switched off and all events are recorded. Thus the rate reduction can be determined by comparing the total number of events, that would have been taken, if no trigger at all was active on the same trigger level, to the number of events taken by a specific trigger:

| Monitor subtriggers | | explanation |
|---|---|---|
| **SpaCal** | | energy in SpaCal IET trigger cells |
| | S0: SPCLe_IET>1 | $> 6$ GeV |
| | S3: SPCLe_IET>2 | $> 9$ GeV |
| | S9: SPCLe_IET>0 | $> 2$ GeV |
| **LAr &** | S24: Mu_Any && LAr_Etrans>1 | any muon trigger, $E_T$ in LAr $> 4.2$ GeV |
| | S25: Mu_Any && LAr_Etmiss>1 | any muon trigger, missing $E_T$ in LAr $> 3.8$ GeV |
| | S64: LAr_Etrans>2 && LAr_IF>1 | $E_T > 6.4$ GeV, sum over big towers in the inner forward region (IF) $> 2.0$ GeV |
| | S65: LAr_electron_1 | electromagn. energy above 2.5 to 5 GeV (depending on LAr region) |
| | S66: LAr_Etmiss>2 && LAr_IF>1 | missing $E_T > 6.4$ GeV, sum over big towers in IF $> 2.0$ GeV |
| | S67: LAr_electron_1 | electromagn. energy above 2.5 to 5 GeV (depending on LAr region) |
| | S68: LAr_electron_1 && CIP_sig>0 | electromag. energy, significance of vertex (see 3.3.3) |
| | S76: LAr_Etrans>1 | $E_T > 4.2$ GeV |
| | S77: LAr_Etmiss>1 | missing $E_T > 3.8$ GeV |
| | S78: LAr_Etmiss>1 | missing $E_T > 3.8$ GeV |
| **others** | S63: FwdMu_Val_Any&&VETO_GL | any valid forward muon, global veto against background, based the on time of flight and the veto system (see sec. 3.2) |
| **S61** | S61: for photoproduction studies, see tab. 6.3 | energy in SpaCal, 1 track $> 900$ MeV |

Table 6.1: Monitor triggers used to determine absolute efficiencies, S65/67 and S77/78 differ in having different L2 conditions.

$$\begin{aligned} \mathcal{R}_{\text{Factor}} &= \frac{\#\text{total events}}{\#\text{triggered events}} \\ \mathcal{R}_{\text{percentage decrease}} &= \left(1 - \frac{\#\text{triggered events}}{\#\text{total events}}\right) \times 100 \end{aligned} \tag{6.4}$$

## 6.2 Triggering $D^*$ mesons in deep inelastic scattering

In the following, the trigger setup used to select $D^*$ mesons in DIS is described and analysed in terms of rate reduction and efficiency. First of all the event selection concerning the scattered electron is motivated and presented, then the FTT trigger elements are analysed in detail and compared. Finally the performance of the complete S61 is presented and possible further rate reductions on the subsequent level 2 trigger system are discussed.

### 6.2.1 Event selection and trigger setup

In this paragraph the selection of the signal events is explained. It was required that the events contain a $D^*$ meson candidate, reconstructed from its decay particles $K\pi\pi_{slow}$ (see sec. 2.3.1). In addition a couple of further cuts are introduced to enhance the signal to background ratio. Among these are cuts on the minimal transverse momenta of the particles, $P_T^{D^*}$ >2.0 GeV, $P_T^{Kaon}$ >0.5 GeV, $P_T^{\pi}$ >0.3 GeV and $P_T^{\pi_{slow}}$ >0.12 GeV. Also the scalar sum of transverse momenta of the Kaon and the Pion are required to be above $|\vec{P}_T^{kaon}| + |\vec{P}_T^{\pi}|$ >2.0 GeV. Additional cuts concern the deviation of the reconstructed mass of the $D^0$ meson from the nominal values ([8]) $|m(D^0)_{rec} - m(D^0)_{nom}|$ <0.08 GeV and the reconstructed $\Delta M = m_{D^*} - m_{D^0} < 0.17$ GeV. As there is a scattered electron required (DIS sample), there are cuts applied in the reconstruction of a possible electron scattered into the SpaCal. Further cuts concern the quality of tracks used in the reconstruction of the $D^*$ meson and, in order to suppress background, on the event timing and the event vertex. All these cuts are summarised in table 6.2. The event selection utilises on the whole the same cuts as applied in the event selection used in [33]. For all of the following efficiency studies it was used in order to select the signal event sample for DIS. In addition, only those runs were included in the study, in which the main detector components were working, namely CJC1, CJC2, LAr, time of flight and veto system, lumi system, CIP2000, COZ as well as SpaCal, and where the FTT was delivering reasonable track information (see sec. 5.3). The investigations concerning the rate reductions were carried out without any event selection, but included only L2/L3/L4 transparent runs, where no events were rejected on the second, third and fourth trigger level. The data used for the DIS efficiency studies were collected in 2005.

The subtrigger used to select the DIS $D^*$ meson sample was subtrigger 61. Its setup is summarised in table 6.3, showing that S61 employs both SpaCal and FTT trigger elements. Its efficiency will be analysed in the next section.

| Variable | Cut |
|---|---|
| **Global event quantities** | |
| Event timing | 438 < $T_0$ signal of CJC < 478 |
| Vertex position | -35 cm < Z-vertex < 35 cm |
| **Quantities of the $D^*$ mesons** | |
| Transverse momentum ($D^*$ meson) | $P_T^{D^*} > 2.0$ GeV |
| Transverse momentum (Kaon) | $P_T^{Kaon} > 0.5$ GeV |
| Transverse momentum (Pion) | $P_T^{\pi} > 0.3$ GeV |
| Transverse momentum (slow Pion) | $P_T^{\pi_{slow}} > 0.12$ GeV |
| Scalar sum of $P_T$ (Kaon and Pion) | $P_T^{Kaon} + P_T^{\pi} > 2.0$ GeV |
| Difference of $m(K\pi\pi_{slow}) - m(K\pi)$ | $\Delta M < 0.17$ GeV |
| Mass of the $D^0$ meson | $\lvert m_{D^0}^{rec} - m_{D^0}^{nominal}\rvert < 0.08$ GeV |
| Cut on track parameters | analogue to those listed in tab. 5.1 |
| **Quantities of the scattered electron** | |
| Polar angle | $157^\circ < \theta_e < 173^\circ$ |
| Energy | $E_e > 11.0$ GeV |
| Cluster radius of the energy deposit | $R_e < 4.0$ cm |
| Impact point in SpaCal | Several regions cut out, see tab. 6.4 |

Table 6.2: Event selection for the DIS sample.

| run number | S61 setup | explanation of trigger element |
|---|---|---|
| 401627 - 405719 | FTT_Tc>1 && | two tracks with $P_T > 400$ MeV |
| | (SPCLe_IET>2 \|\| | energy deposit of > 9 GeV in SpaCal |
| | SPCLe_IET_Cen_3) | energy deposit of > 9 GeV in central SpaCal region |
| 401627 - 405719 | FTT_Td>0 && | one track with $P_T > 900$ MeV |
| | (SPCLe_IET>2 \|\| | energy deposit of > 9 GeV in SpaCal |
| | SPCLe_IET_Cen_3) | energy deposit of > 9 GeV in central SpaCal region |

Table 6.3: The setup of subtrigger S61.

### 6.2.2 Triggering the scattered electron: SpaCal trigger conditions

The electromagnetic part of the SpaCal, which is exploited in DIS, might suffer from different inefficiencies. These may arise in the determination of the energy of an electron candidate because of a broken photomultiplier or readout card. There can also exist genuine trigger inefficiencies due to broken trigger cards. In addition a false calibration can not only lead to wrongly determined electron energies, but can also be the reason for trigger cells triggering despite of the electron energy actually being too low. The impact of these influences is investigated in this thesis based on a commonly used method. First of all, the energy weighted distribution of electrons for the SpaCal is plotted, then the inefficient areas of the SpaCal are determined by systematically eye-scanning this distribution for problems for asymmetries and noticeable deviations. The energy distributions in these areas are then plotted and compared to that of the whole spacal and also to the one in an area, which is defined by a reflection of the area to be studied at the origin and thus has reversed xy-coordinates. All three energy distributions should be very similar within statistical fluctuations. Only the number of detected electrons should strongly depend on the radius, because of the correlation between $\theta_{e'}$ and the inclusive cross section. This not being case is a strong indication for a broken readout card or a falsely calibrated photomultiplier.

Fig. 6.1 depicts the energy weighted spatial distribution of electrons in the SpaCal for 2005 data[1]. Clearly visible and also indicated by black boxes are regions of decreased sensitivity, i.e. regions, where scattered electrons are not detected at all or have a different energy distribution than in fully functional areas of the SpaCal. This is demonstrated in fig. 6.2. Here one can see the energy distribution of the full SpaCal, which is plotted as shaded histogram. Prominently visible is the so-called kinematic peak at $\sim$27.5 GeV [84]. In comparison the energy distribution of a SpaCal area with decreased sensitivity is shown, marked with dots: Here no kinematic peak is visible, the electron energy distribution is rather flat. Also depicted for comparison is the energy distribution of the area reflected in the origin for the same event sample as triangles: Its energy distribution is comparable to the one of the whole SpaCal, which supports the assumption, that the area investigated is indeed not working properly. Its spatial position is marked in fig. 6.1 by a dotted rectangle.

The findings of these studies are summarised in tab. 6.4, where the coordinates of the SpaCal areas which should be cut out and not be used in analyses are listed. This list was compared to an earlier study [85], which produced independently from this study the same results apart from the fact that several SpaCal holes were not detected then but developed later and were only discovered in this study. These occurrences were immediately reported to people affected by these inefficiencies [33].

The impact of these "dead" cells is demonstrated in fig. 6.3, where the efficiency of the SpaCal trigger elements for selecting $D^*$ events in DIS in comparison to LAr monitor[2] triggers is plotted as a function of $\theta_e$. The efficiency of the SpaCal TEs is plotted as a black line before the inefficient cells are cut out and in comparison as red dots after they have been excluded. It can be seen, that cutting out areas of decreased SpaCal sensitivity

[1] The DIS studies, the SpaCal is needed for, cover only 2005 data. Additionally during the shutdown in winter 2005/2006 the SpaCal was repaired.

[2] This was possible, because the LAr triggers suffered from noise and triggered, despite the fact that there was of course not second scattered electron in the event causing energy deposit in the LAr.

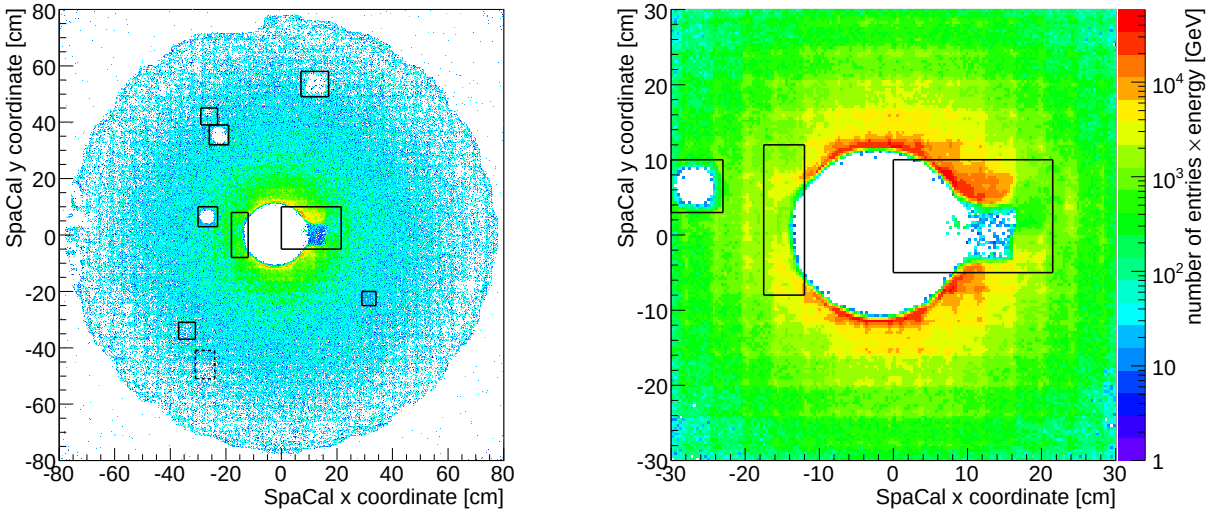


a) full SpaCal b) inner SpaCal

Figure 6.1: The energy weighted spatial distribution of electrons which have hit the SpaCal. The black boxes indicate regions of decreased sensitivity, i.e. regions, where scattered electrons are not detected at all or have a different energy distribution than in fully functional areas of the SpaCal as demonstrated in fig. 6.2.

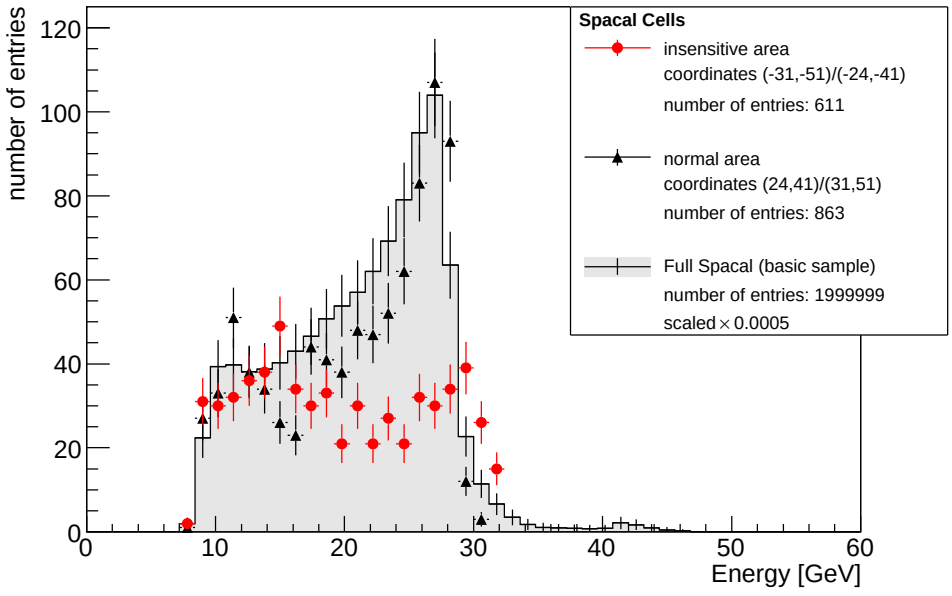


Figure 6.2: The energy distribution of all electrons (solid line) compared to the one of the insufficient areas (dots) and of an area defined by a reflection in the origin (triangles, reversed coordinates). The coordinates are given as the (x,y)-coordinates of the lower left and the upper right corner of the areas.

| Region of decreased SpaCal sensitivity (number of dead photomultiplier) | X range | Y range |
|---|---|---|
| 75 and 76 | 0 to 18 cm | -5 to 5 cm |
| 547 | -31 to -24 cm | -51 to -41 cm |
| 306 | -37 to -31 cm | -37 to -31 cm |
| 59 and 60 | -18 to -12 cm | -8 to 8 cm |
| 258 | -26 to -19 cm | 32 to 39 cm |
| 403 | -29 to -23 cm | 39 to 45 cm |
| 190 | -30 to -23 cm | 3 to 10 cm |
| 691 and 692 | 7 to 17 cm | 49 to 58 cm |
| 223 | 29 to 34 cm | -25 to -20 cm |

Table 6.4: Regions of dead SpaCal cells or cells with decreased sensitivity in the data taking period 2006.

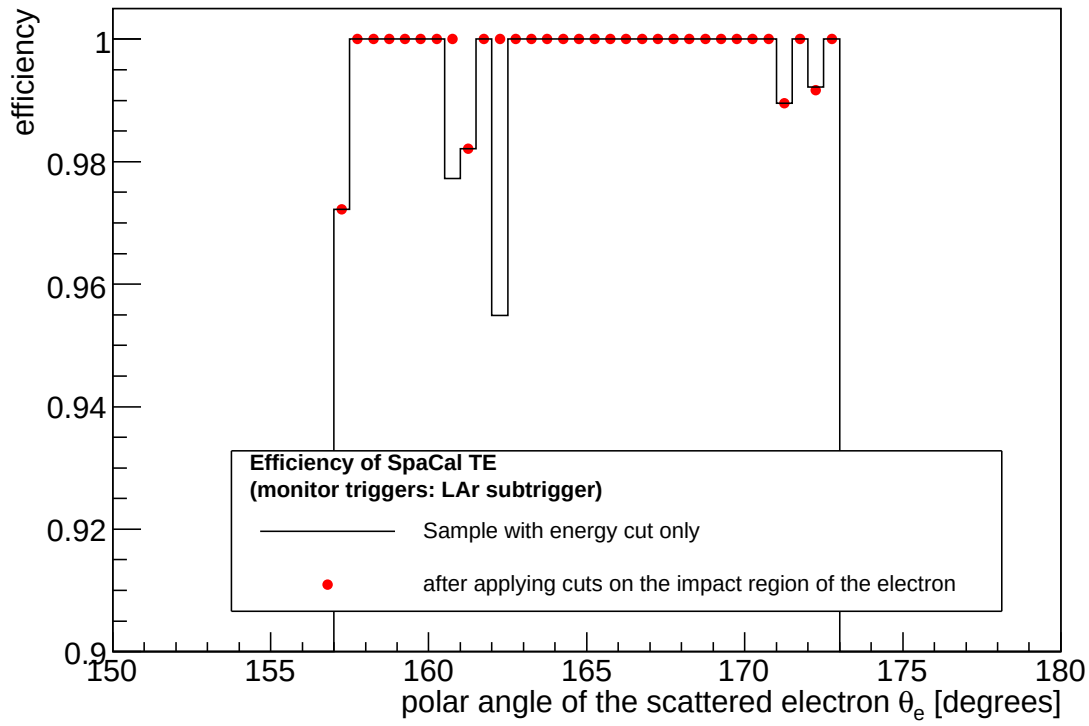


Figure 6.3: The efficiency of the SpaCal trigger elements used in S61 as function of $\theta_e$. Before the application of cuts on the impact region of the electron, inefficiencies can be spotted (black line). After regions of decreased SpaCal sensitivity are cut out, the trigger becomes more efficient (red dots). For some inefficiencies no regions of decreased SpaCal sensitivity could be identified and cut out. As the overall efficiency was satisfying, the reasons for inefficiencies (wrongly calibrated or insufficient photomultipliers) were not investigated in more detail.

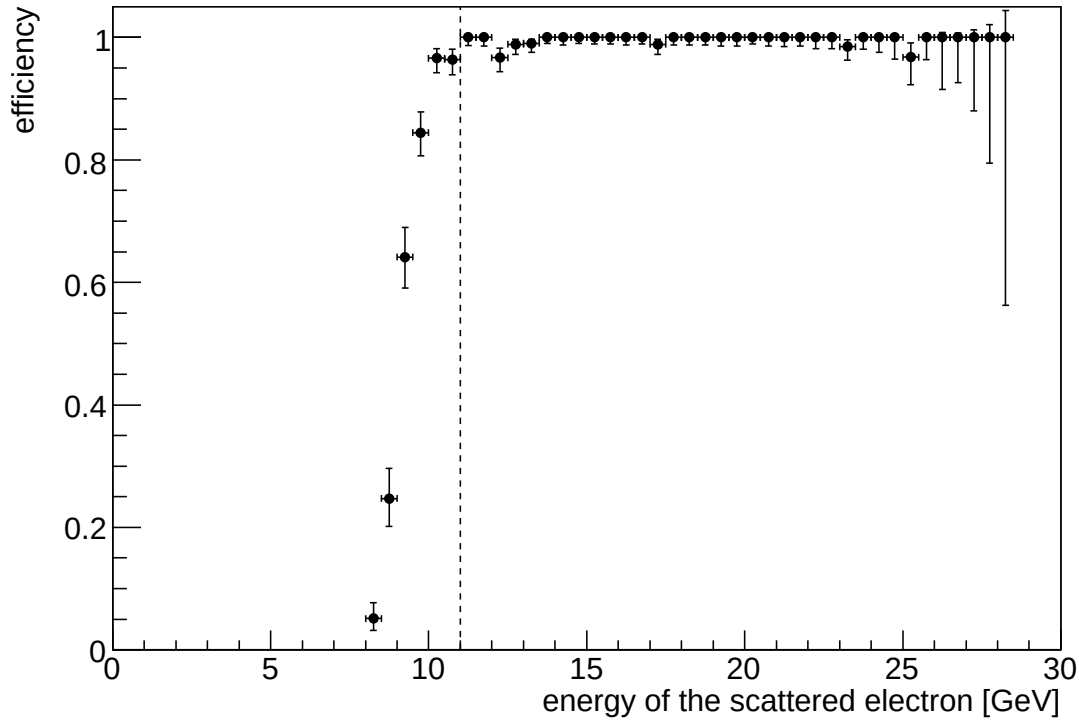


Figure 6.4: The efficiency of the SpaCal trigger elements used in S61 in dependence of the energy of the scattered electron. Before the application of cuts on the minimal energy of the electron, a threshold behaviour of the trigger can be observed (markers). Above an electron energy of 11 GeV (dashed line), the efficiency is flat.

improves the efficiency of S61 in region of $\theta_e \approx 162°$. Still, there are some holes undetected, which are situated in the inner region (high $\theta_e$ regime, $\theta_e > 170°$) and in the outer region of the calorimeter (low $\theta_e$ regime, $\theta_e \approx 157{,}5°$). However, in the scope of analysis of $D^*$ mesons the overall efficiency of the SpaCal TE is fully satisfying and does not need further improvement. Its integrated efficiency amounts to $0.998 \pm 0.004$, which is at the moment fully sufficient for the precision aimed at in the analysis of $D^*$ mesons, due to the statistical yield.

Before moving on to the FTT TEs in S61, the threshold behaviour of the SpaCal trigger elements shall be shortly discussed. Fig. 6.4 shows the efficiency of the SpaCal trigger elements as a function of the electron energy. The trigger threshold lies at 9 GeV, but the distribution becomes flat only for $E_e > 11.0$ GeV (dashed line). Therefore it is important to cut on the energy of the electron, in order to have a clear cut instead of a washed out threshold slope. This allows to study FTT effects in detail.

With the above introduced cuts on the quantities of the scattered electron the efficiency of the SpaCal trigger elements used in S61 amounts to 100 % in most bins of $\theta_e$ and $E_e$. The same is true for all event variables of $D^*$ mesons in DIS, e.g. $Q^2$, inelasticity $y$, transverse momentum of the $D^*$ meson [86].

### 6.2.3 Triggering $D^*$ mesons: FTT track based trigger conditions

In the following the performance of the FTT TEs used in S61 is analysed. The efficiency of the FTT TEs was determined by using a $D^*$ meson sample that was recorded by SpaCal subtriggers as reference, because this gives higher statistics compared to LAr monitor triggers. The analysed FTT TE, Tc1 and Td0, correspond to at least two tracks above 400 MeV and one track above 900 MeV, respectively. Fig. 6.5 shows the efficiencies as a function of different variables for both of these trigger elements, with the Tc1 efficiencies depicted as dots, while the ones for Td0 are marked by triangles. The differences between the trigger elements are most prominently seen in the dependence on the multiplicity of an event (here measured as the number of central tracks as specified in table 5.1) and on the transverse momentum of the track with the highest $P_T$ in an event, see fig. 6.5, a) and c). When regarding the related event quantities, namely the inelasticity of an event and the transverse momentum of the $D^*$ meson, the dependence is not as strong, but rather smeared out, partly also because of the larger bin size, see fig. 6.5, b) and d). The integrated efficiency of FTT Tc1 amounts to 0.9842±0.0009, while the one of FTT Td0 measures 0.978±0.001. Thus, the overall difference amount to 0.007±0.001, with a slightly better performance of the FTT Tc1, requiring two tracks with a lower $P_T$ threshold. As the setup of the S61 was changed in order to improve the efficiency of the multi-purpose heavy flavour trigger for selecting J/Ψ mesons significantly and in order to tame its rate, an accompanying loss of 0.7 % efficiency for $D^*$ mesons is acceptable [87], [88].

The overall performance of the S61 (determined using LAr triggers) is shown in fig. 6.6 as a function of $Q^2$ of the $D^*$ meson and inelasticity y. The integrated efficiency of S61 amounts to 0.9895±0.005, which is consistent with the expected value, when combining the SpaCal and FTT Td0 efficiencies, both obtained with a LAr reference sample. The FTT Td0 efficiency amounts in the case of LAr as monitor trigger to 0.998±0.004. It is slightly higher than the efficiency obtained with the SpaCal triggered reference sample, as the LAr triggered reference sample has a higher multiplicity per event, also the highest $P_T$ in the event is higher. The efficiencies obtained for the FTT Td0 trigger element yields together with the above quoted SpaCal efficiency an expected efficiency of the full S61 of 0.9895±0.006. The slightly dropping efficiency of S61 for events with low multiplicities could be improved with an improved track finding efficiency for the FTT L1 trigger, which is however already close to its design values. The integrated efficiencies are summarised in table 6.5.

### 6.2.4 Further possibilities on Level 2

S61 triggers on L1 with stable rates of approximately 12 Hz [89], while the trigger elements, composing S61, run with rates of 20 000 Hz (FTT TE) and 50 Hz (SpaCal TE). Only their combination allows for stable S61 running without prescales. S61 is linearly dependent on the instant luminosity, which is planned to be raised by increasing the beam currents before the shutdown of HERA. Therefore S61 might in future deliver higher rates, and hence might be object to prescaling. As this is not desired, possible validations of S61 on the second trigger level are presented in the following. Their aim is to reduce the rate of S61 on the second trigger level while obtaining nevertheless high efficiencies and

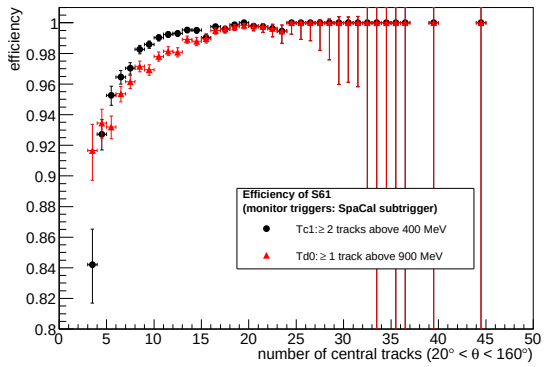


a) depending on number of central tracks

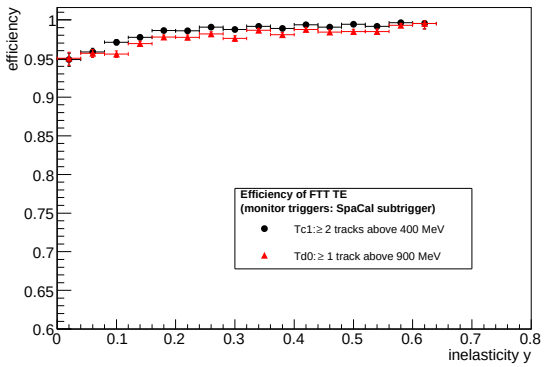


b) inelasticity $y$

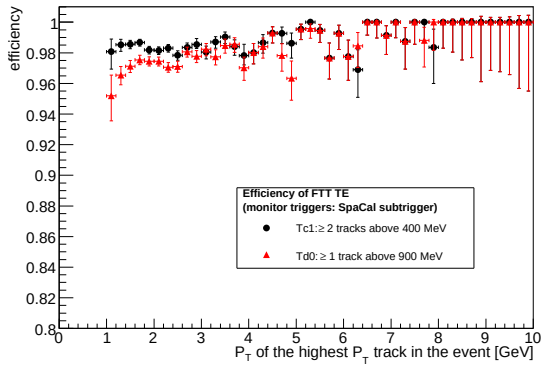


c) transverse momentum of highest $P_T$ track

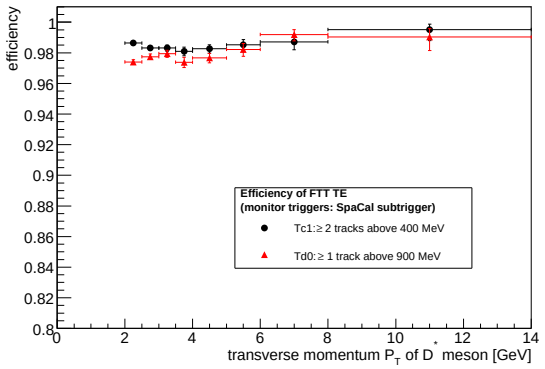


d) transverse momentum of $D^*$ meson

Figure 6.5: Efficiency of FTT trigger elements Td0 and Tc1 for the selection of $D^*$ mesons in comparison. While Td0 is more efficient triggering low multiplicity events, Tc1 is more efficient for events with low $P_T$ tracks only. When comparing the relevant variables of the $D^*$ mesons, $P_T$ and inelasticity, the differences amount to less than 1 % in total.

| analysed subtrigger or TE | efficiency for | |
|---|---|---|
| | LAr monitor triggers | SpaCal monitor triggers |
| SpaCal TE | 0.998±0.004 | not independent, not used |
| FTT TE Tc1 | 0.989±0.006 | 0.9842±0.0009 |
| FTT TE Td0 | 0.998±0.004 | 0.978±0.001 |
| full S61 (Td0) | 0.9895±0.005 | not independent, not used |

Table 6.5: Efficiencies for S61 and its trigger elements. The efficiencies for the FTT TEs are higher for the LAr monitor trigger sample, because these have a higher multiplicity per event, also the highest $P_T$ in the event is higher.

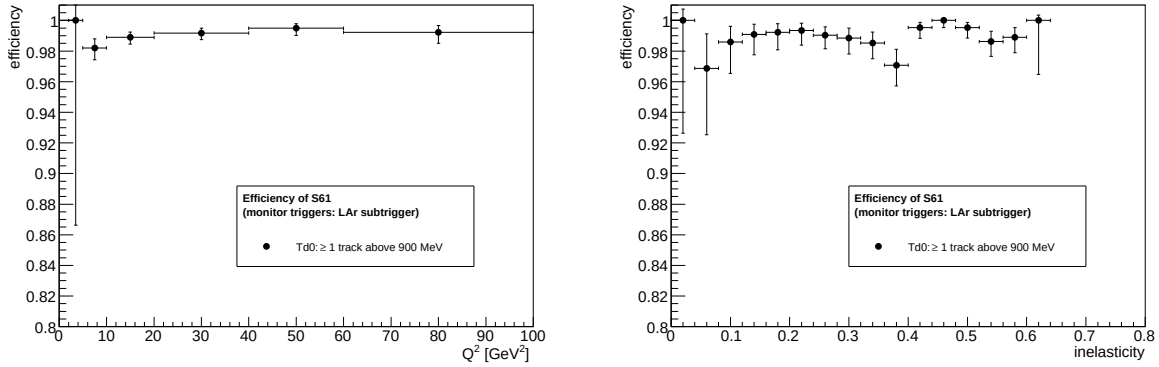


a) full efficiency of S61 as function of $Q^2$ b) full efficiency of S61 as function of inelasticity $y$

Figure 6.6: Efficiency of S61: The subtrigger is highly efficient. The efficiencies of more than 95 % for all bins of the above shown variables are reproducible for the other relevant quantities.

thus allowing to use S61 without prescales.

Fig. 6.7 shows the expected efficiencies and percentage rate reductions for various trigger setups. These trigger setups differ in the number of tracks required and in the $P_T$ threshold. Squares mark efficiencies and rate reductions, if exactely one track above the different thresholds is required, while circles and triangles represent the requirement of at least two and three tracks above the thresholds. For each multiplicity requirement, indicated by the three different marker styles, seven markers are drawn, representing the applied thresholds at 100, 170, 417, 700, 1000, 2500 and 5000 MeV. The rate reductions as well as efficiencies shown were determined using L4 transparent runs and were measured relative to the efficiency and rate of S61 on L1. The efficiencies and rate reduction obtained through prescaling are indicated by a straight black line. All of the shown trigger setups show efficiencies and rate reductions, which are at least as good as the one obtained by prescaling. With increasing number of tracks required, the markers for the respective thresholds are shifted towards higher rate reductions and lower efficiencies. The same is true for the required threshold. This indicates, that a combination of both, minimal multiplicity requirement and minimal $P_T$ would yield an optimal relation of efficiency and rate reduction. The presented conditions have however not been yet implemented as L2 trigger, as there is not yet an urgent need to reduce the S61 rate, furthermore the impact on efficiencies of the other charm events, S61 is supposed to trigger, have to be investigated.

One possible setup combining multiplicity and $P_T$ conditions is indicated in fig. 6.7 as a black star. It requires at least three tracks above 100 MeV and at least one track above 1000 MeV. It is characterised by maximum rate reduction and minimum efficiency loss, yielding a rate reduction of 50 % almost without reducing the efficiency. When it is analysed differentially relative to the S61 L1 efficiency, it becomes evident, that there is no dramatic loss in efficiency for any of the analysis bins of $D^*$ mesons in DIS. This is shown in fig. 6.8, where the L2 efficiencies as function of inelasticity $y$ and the transverse momentum of the $D^*$ meson relative to the L1 efficiencies are plotted. The integrated relative efficiency of this level 2 setup amounts to 0.968±0.002. The convoluted absolute efficiency of L1 and L2 conditions, amounts to 0.958±0.005, using the above obtained L1

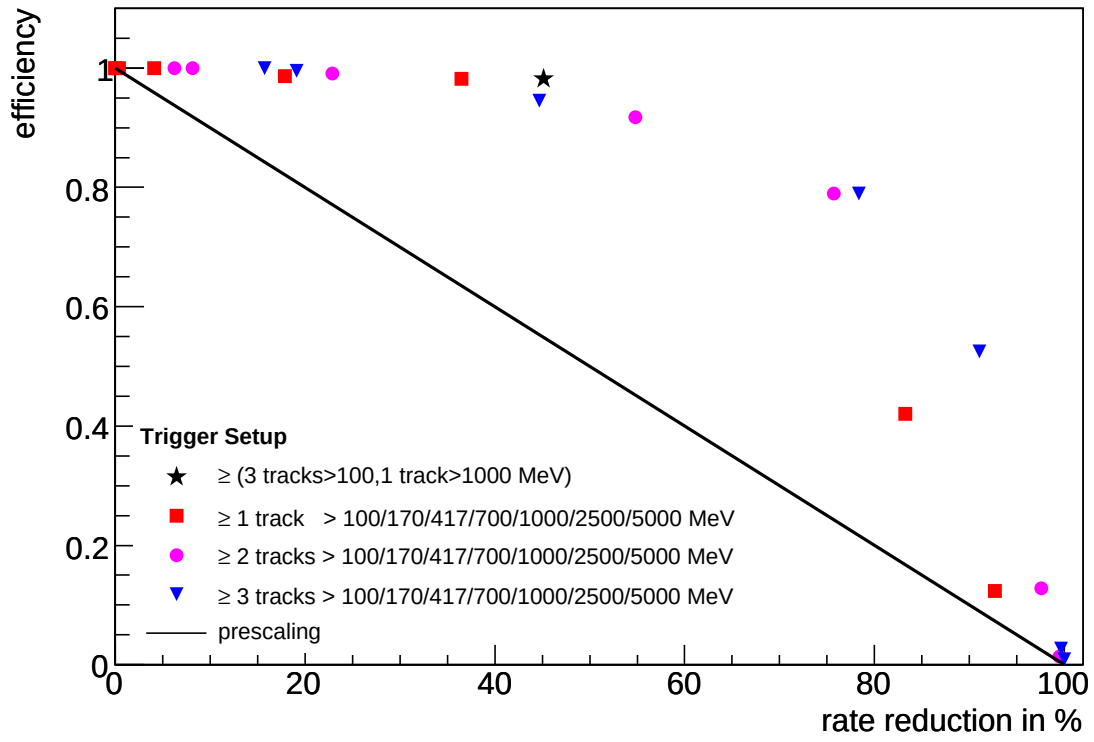


Figure 6.7: Possible rate reductions and efficiencies of L2 trigger conditions on S61 for DIS data. Shown is the efficiency in dependence of the rate reduction in percent for a trigger condition requiring one, two or three tracks (different colours) above each $P_T$ threshold (100, 170, 417, 700, 1000, 2500 and 5000 MeV, each represented by the n-th marker in the respective colour counted from the left hand side).

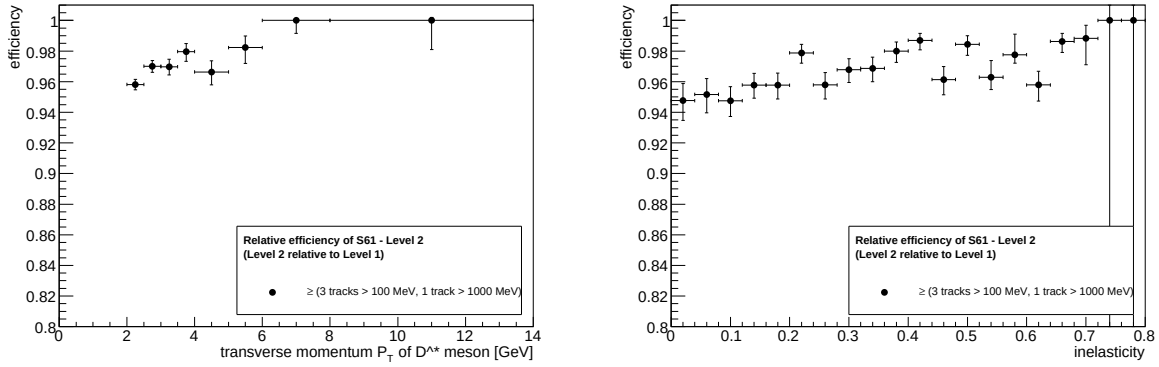


a) relative efficiency of S61 Level 2 as function of $P_T$ b) relative efficiency of S61 Level 2 as function of $y$

Figure 6.8: The efficiencies for a possible setup of a FTT-L2 trigger for $D^*$ mesons depicted as functions of the transverse momentum of the $D^*$ meson and of the inelasticity, measured relative to the L1 efficiencies.

efficiency.

In order to study the threshold behaviour of the FTT trigger elements in terms of multiplicity and transverse momentum $P_T$, an additional investigation was undertaken. It analyses the efficiency of S61 and additional L2 trigger conditions for different variables, where the additional L2 trigger elements applied were varied in the number of tracks required above 100 MeV and in the threshold above which one track was required. Fig. 6.9 shows, how the efficiency of S61 changes when the number of tracks required above 100 MeV is varied from more than one to more than five. As can be seen from the plot on the left hand side, the efficiency of the respective trigger condition is approximately 50 %, when the events contain as many tracks as required. Although, events with $D^*$ mesons have already at least three tracks from the decay particles, there can be still inefficiencies observed, when there are at least two tracks above 100 MeV required. This points to the fact, that there is a certain amount of events, where two or more tracks are not detected in the FTT. The right hand side depicts how the multiplicity variations influence the selection efficiency as function of the inelasticity of an event. While for the number of tracks a quite sharp threshold for the trigger selection is observed, the slope of the efficiency as a function of the inelasticity is much softer. So, while the efficiency depending on the number of central tracks in an event is very low for some bins due to the trigger selection, the efficiency as a function of the inelasticity is affected by these trigger cuts for a quite large span of $y$, but never drops to zero. This effect is in part also arises of course from the fact, that the number of tracks in events is a discrete distribution, while $y$ is a continuous function.

A similar investigation on the impact of the used $P_T$ threshold was performed, whose outcome is shown in fig. 6.10. Required is in detail at least one track above 417, 710, 1000, 2500 and 5000 MeV. Not surprisingly, the influence on the selection efficiency is largest as function of variables like the $P_T$ of the $D^*$ meson or of the selected track with the highest transverse momentum. The slope of the efficiencies as functions of $P_T$ for different trigger thresholds are however not as steep as the slope of the efficiencies as functions of multiplicity for different number of tracks above a certain threshold (compare

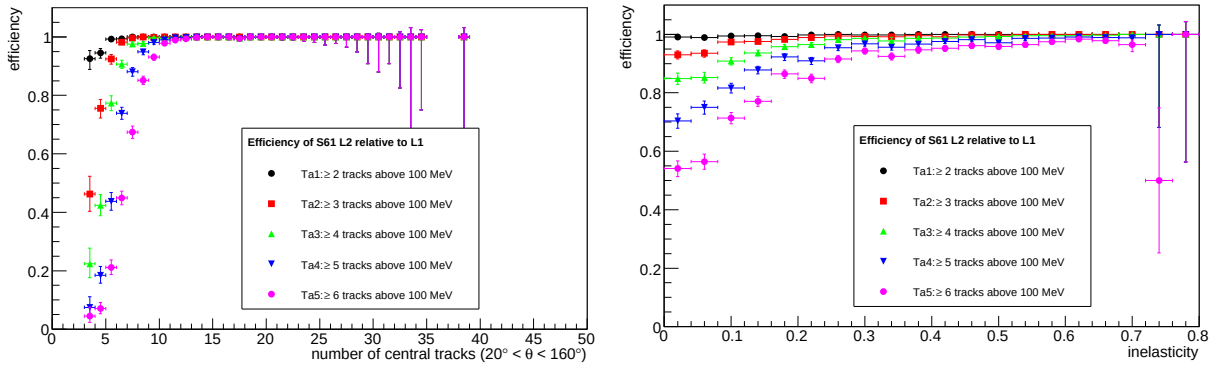


a) relative efficiency of S61 Level 2 as function of the number of central tracks and ...

b) ... as function of $y$, when varying the multiplicity trigger condition

Figure 6.9: Efficiency of additional Level 2 conditions to S61: The efficiency of S61 with different additional L2 conditions, which vary in the number of tracks above the 100 MeV threshold, is depicted as function of the number of central tracks and $y$ for DIS data.

fig. 6.9). Furthermore, the use of the $P_T$ thresholds 2500 and 5000 MeV can be excluded as possible TEs for the selection of $D^*$ mesons due to their low overall efficiencies. These studies show, which impact variations in the multiplicity requirement as well as in the $P_T$ threshold have on the efficiency of a $D^*$ meson trigger in different regions of phase space. They allow to estimate roughlz, which alternative trigger setups might be possible or usefull to implement.

A conclusion on the the threshold behaviour can also be drawn from the $P_T$ distributions of events, where in this case it is required, that in the FTT exactly one track was reconstructed and **no** $D^*$ meson selection is applied. The $P_T$ distribution of all the analysis tracks, passing the cuts specified in tab. 5.1, were plotted by filling the $P_T$ for each track of an event into a histogram. The result of this investigations is shown in fig. 6.11, where the $P_T$ distributions are depicted for events with only one track detected in the FTT above the different trigger thresholds of 100, 170, 417, 710, 1000, 2500 and 5000 MeV. The $P_T$ distributions for the different thresholds can be distinguished by the used marker, specified in the legend in fig. 6.11. In addition the nominal position of the thresholds is marked by dashed vertical lines. It can be seen, that especially in events, with exactely one track in the FTT above 2500 MeV and 5000 MeV there is a large fraction of low $P_T$ tracks. The main reason for this is, that the low $P_T$ tracks passing the analysis selection are not detected in the FTT, while the high $P_T$ tracks detected in the FTT do not pass the analysis cuts for tracks. It can also happen, that tracks are reconstructed falsely in the FTT with a too large $P_T$, because they stem from secondary vertices and are fitted by the FTT onto the primary vertex, which of course changes their transverse momentum dramatically. Both cases can occur, as can be verified by comparing on an event to event basis. Apart from the peak due to the pollution by low $P_T$ tracks, also the distributions for the high $P_T$ thresholds peak just above their respective thresholds, which can be observed also for the other thresholds. In general, the plot shows, that there is indeed a considerable fraction of undetected low $P_T$ tracks, which amounts to ≈15% (≈32%), when comparing the number of tracks below 3 (5) GeV with the number of tracks above 3 (5) GeV. 3 GeV and 5 GeV were chosen, because the distribution for

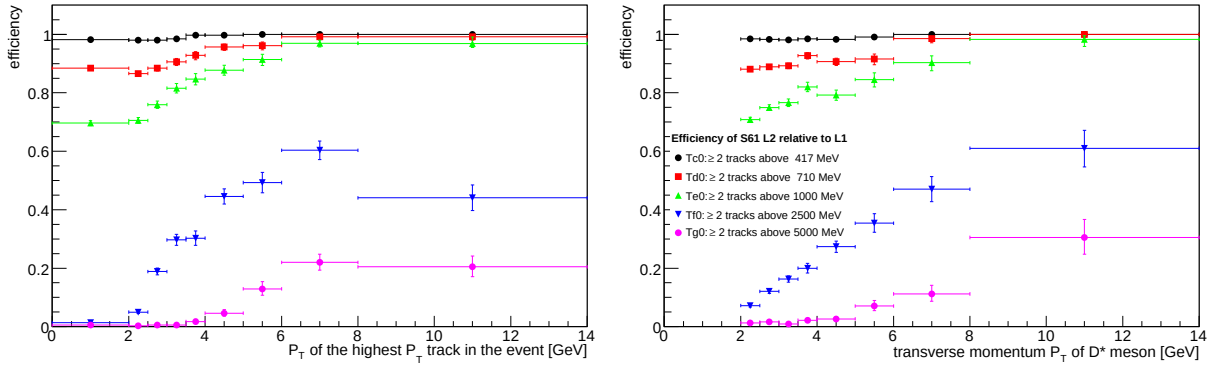


a) relative efficiency of S61 Level 2 as function of the transverse momentum of the highest $P_T$ track and ...

b) ... as function of the $P_T$ of the $D^*$ meson, when varying the $P_T$ trigger condition

Figure 6.10: Efficiency of additional Level 2 conditions to S61: The efficiency of S61 for DIS data with different additional L2 conditions, which vary in the transverse momentum threshold applied, is depicted as function of the transverse momentum of the highest $P_T$ track in the event and of the $P_T$ of the $D^*$ meson. The respective conditions are the same for both plots and are explained in the legend of the illustration on the right hand side.

the 5000 MeV threshold starts to rise at 3 GeV, while the nominal threshold is situated at 5 GeV. These studies show, that the general performance of the FTT Level 2 trigger threshold is good, the threshold are situated at their nominal values and apart from the higher thresholds there is no significant fraction of undetected tracks.

## 6.3 Triggering $D^*$ mesons in photoproduction

Due to the $1/Q^4$ dependence of the cross section, the photoproduction sample of $D^*$ mesons has a higher statistical yield compared to the DIS sample. In addition photoproduction samples cover a larger range in inelasticity compared to DIS samples, where due to the SpaCal selection the DIS sample is restricted to inelasticities $y$ <0.7. In the following section different possibilities to select $D^*$ mesons in photoproduction are analysed and discussed.

### 6.3.1 Event selection and trigger setup

The basic event selection for all of the investigations undertaken in this chapter is the same like the one for DIS, see table 6.2. The only exception is, that there is required to be no candidate for a scattered electron with an energy above 8 GeV. Normally, for an analysis, one would try to optimise the cuts in order to obtain a better signal to background ratio and, for example, cut on the $\frac{dE}{dx}$ of a particle. As the main goal presented herein is to analyse strategies to select $D^*$ mesons with the help of trigger algorithms, no sophisticated cuts are used.

As a starting point, subtrigger 56 was studied. It is dedicated to trigger $D^*$ mesons in photoproduction using FTT L1 and L2 conditions as well as L2 NN conditions. It was run as test trigger in the first half of 2006, its setup is summarised in table 6.6. In consequence

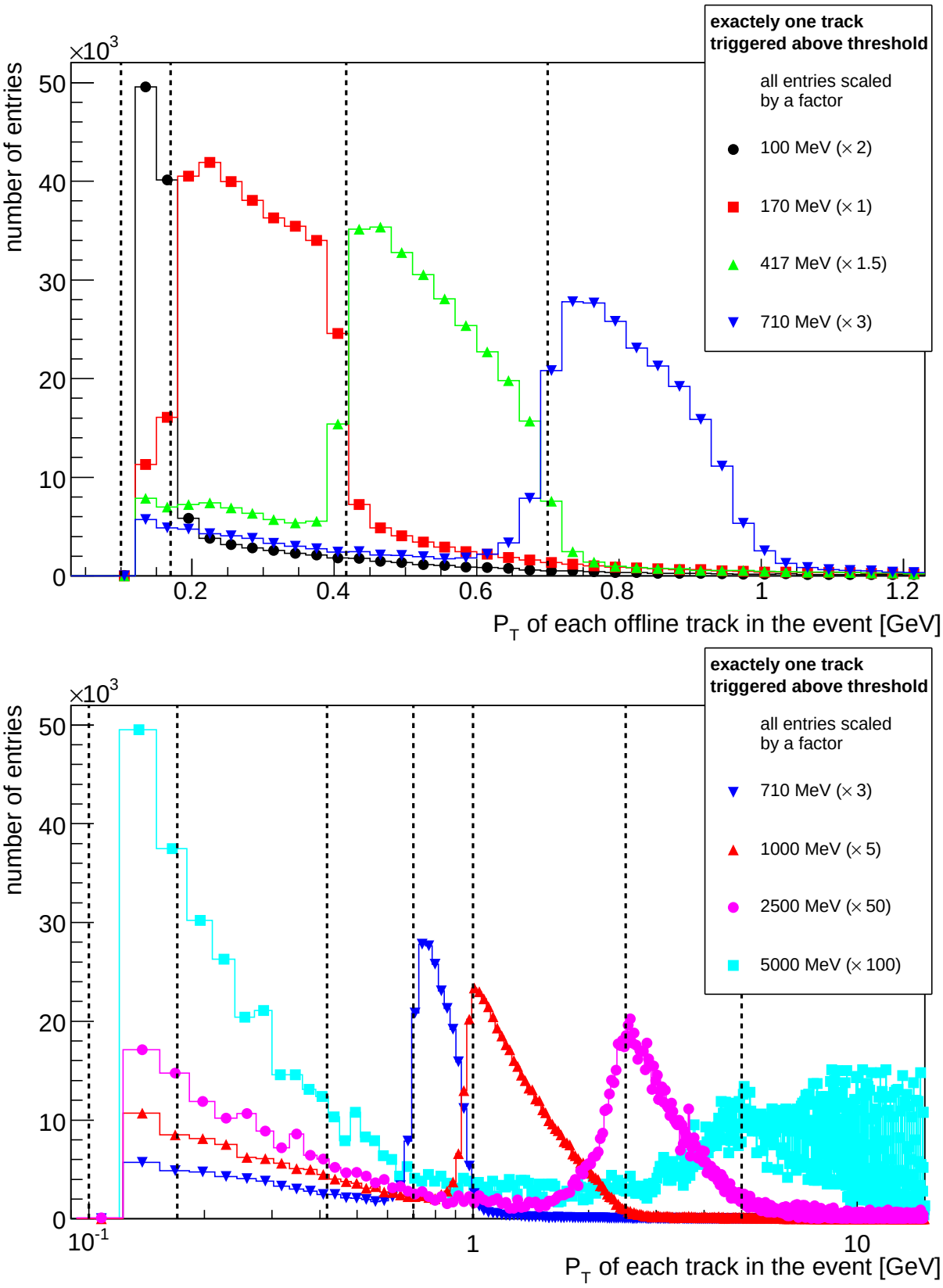


Figure 6.11: The transverse momentum distributions of events, which were triggered with exactly one track above a certain threshold and with **no** $D^*$ meson and **no** trigger selection applied. The vertical dashed lines indicate 170, 417, 710, 1000, 2500 and 5000 MeV.

| S56 original setup | explanation |
|---|---|
| CIP_sig>2 && | significance of the z-vertex |
| FTT_mul_Ta>5 && | more than 5 tracks with $P_T > 100$ MeV |
| FTT_mul_Tc>2 && | more than 3 tracks with $P_T > 417$ MeV |
| FTT_mul_Td>0 && | more than one track with $P_T > 900$ MeV |
| **Additional L1 conditions** | **explanation** |
| CIP_mul_4 && | more than 10 tracks seen in CIP chamber |
| FTT_mul_Td>2 && | more than 2 tracks with $P_T > 900$ MeV |
| FTT_mul_Te>1 && | more than one track with $P_T > 1800$ MeV |
| **L2 conditions** | **explanation** |
| L2 NN untagged $D^*$ && | neural network trained with a $D^*$ meson photoproduction sample |
| FTT E_Tot_5 | total transverse energy > 5 GeV |

Table 6.6: The setup of subtrigger S56. The L1 conditions were tightened as a consequence of the results presented in this thesis and are identical to the one of S53 and S120.

of the findings presented in this thesis, additional trigger conditions were applied on Level 1 to improve the performance of S56. The additional conditions are also listed in table 6.6.

In the following, the Level 1 conditions of S56 will be analysed and improved. In addition to its absolute L1 efficiencies, also its total absolute efficiencies, including Level 1 and 2, will be presented. The study of the L2 efficiencies of S56 includes a discussion of the single TEs as well as an investigation of alternatives. One of these alternatives could be the usage of a FTT L3 based resonance finder algorithm. This alternative will be thouroughly discussed in a separate section, covering the resolution of the invariant masses and the performance of the momentarily implemented finder algorithm on L3. These alternative trigger setups are used for further untagged $D^*$ subtriggers, namely S53 and S120. They were implemented in the course of 2006, and employ the same conditions like S56 on Level 1, but different conditions on the subsequent trigger levels. Thus they can be used to complement and to monitor each other. The goal is to be able to run them without prescales as well.

### 6.3.2 Improvements to Level 1 untagged photoproduction triggers

As the L1 rate of S56 was still at 1000 Hz and the L2 rate at 10 Hz at the beginning of 2006, with a prescale factor of up to 8 [89], there was an urgent need to reduce the output rate of the subtrigger by imposing additional conditions. Especially the rate of L1 had to be tamed, since the high output of L1 and the low keep rate of these events on L2 affected seriously the data taking [90]. In order to find a solution, an investigation of possible additional L1 trigger elements was performed. Fig. 6.12 shows estimations for the rate reductions and efficiencies of various tightened setups of S56. Four different setups were analysed, which built upon one another, each required one trigger condition additional to the setup analysed preceedingly. The first setup required additionally to S56 one track with a transverse momentum above 1800 MeV, marked by a square, while the second alternative setup required additional to the previous setup two tracks with a $P_T$ above

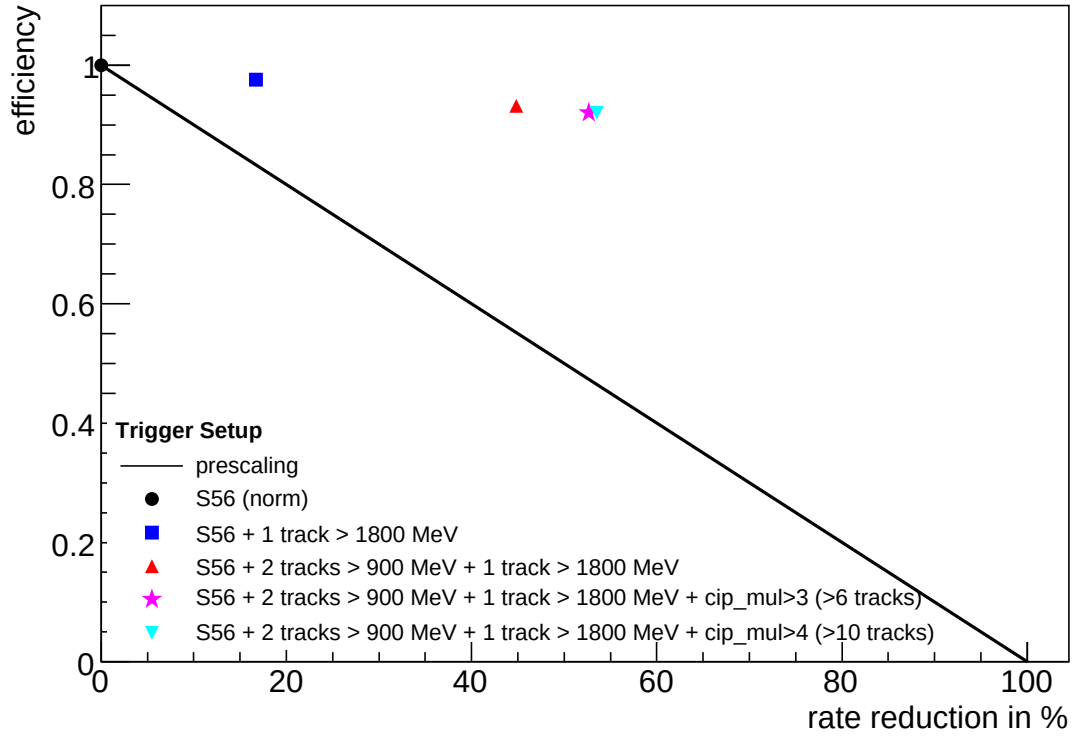


Figure 6.12: Impact of additional trigger conditions on the L1 rate of S56. The original setup of S56 is used as reference, indicated by a black dot at no rate reduction (reduction factor =1) and 100 % efficiency.

900 MeV, its performance indicated by a triangle. Trigger setups 3 and 4 were varied in the multiplicity required in the CIP chamber, indicated by a triangle pointing down and a star. For comparison, a black line indicates, what would be achieved using prescales.

These estimates were retrieved by comparing the rates and efficiencies of the tightened setups with those of the original setup of S56. For the estimate of the rate reduction only those runs were regarded, in which the L2 and L4 triggers were switched off. The figure clearly shows, that there is the possibility to gain at least a factor 2 in rate reduction with no dramatic loss in efficiency, that is with an efficiency which is significantly better than what would be achieved using prescaling.

The efficiencies for the different L1 setups were then compared as functions of different variables. This was done in order to check whether the slight decrease in efficiency due to the tightened L1 conditions leads to systematic inefficiencies or, in the worst case, to zero efficiency in regions of interest, which would be then cut out totally already at trigger level. It was found that this is not the case for the tightening of the S56 Level 1. Fig. 6.13 shows exemplarily the efficiencies as function of the inelasticity of an event as well as for the $P_T$ of the $D^*$ meson: For both variables and all examined trigger setups the efficiencies were more or less flat. No dramatic decrease of efficiency could be detected for a specific kinematic region. The integrated efficiency of the original setup of S56 amounts to 0.84±0.01, while the efficiency of the tightest setup investigated and

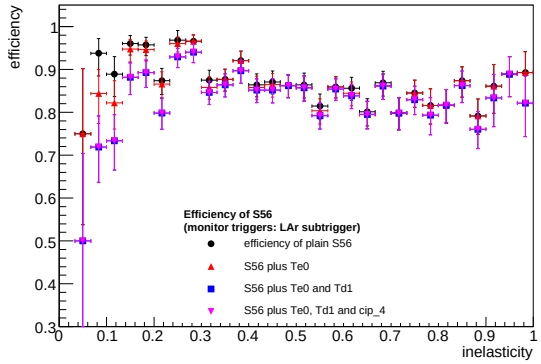


a) as function of inelasticity $y$ (LAr monitor triggers)

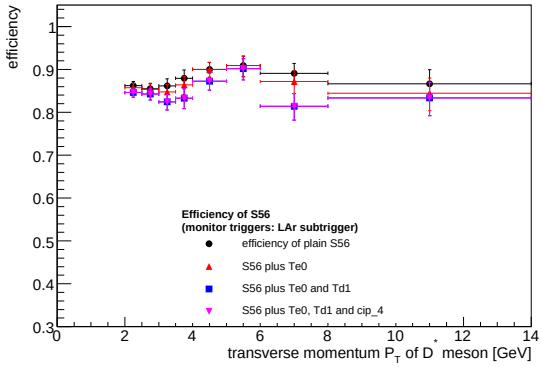


b) as function of the $P_T$ of the $D^*$ meson (LAr monitor triggers)

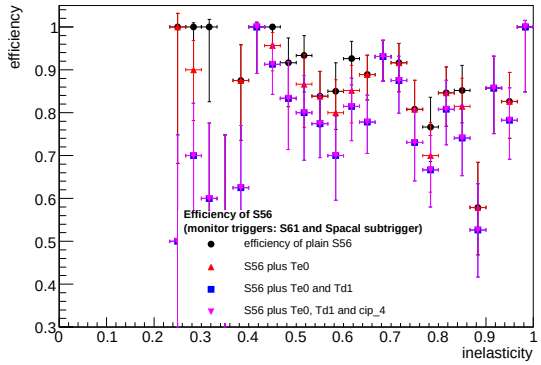


c) as function of inelasticity $y$ (SpaCal monitor triggers)

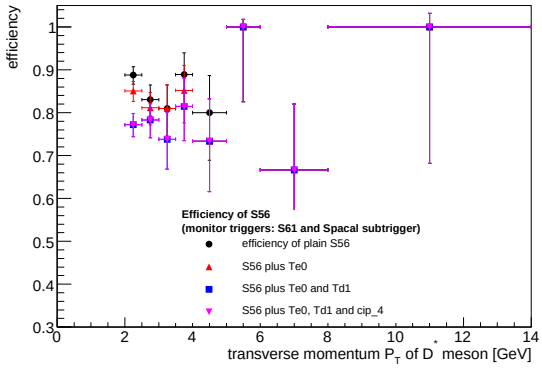


d) as function of the $P_T$ of the $D^*$ meson (SpaCal monitor triggers)

Figure 6.13: Efficiencies for the first level of S56. While a) and b) show the efficiencies for LAr monitor trigger, c) and d) show the efficiencies for SpaCal and S61 as monitor triggers.

finally implemented measures 0.79±0.01. The resulting loss in efficiency of 0.05±0.02 is rather small – compared to the loss of 50%, when using prescales to cut down the rate by a factor of 2. As a consequence of this study, the L1 setup of S56 was tightened so that it could be run without almost any prescales after this change [91], [92]. Also the other $D^*$ meson untagged photoproduction triggers, S53 and S120, profited from these changes, as they use the same L1 conditions as S56, starting with run 453524 and with all conditions specified in table 6.6.

### 6.3.3 Efficiency of S56 on Level 2

On level 2, S56 employs two trigger elements, namely a neural network (NN) and a FTT trigger condition, requiring the total energy of an event to be larger than 5 GeV. It is interesting to compare their respective rate reductions and efficiencies. This is done in fig. 6.14, where the FTT $E_{tot}$ trigger element (triangles), the NN trigger element (squares) and the complete L2 trigger (dots) are compared. While the dark markers represent the rate reductions and efficiencies relative to L1 after its conditions were tightened, the light markers depict the rate reductions and efficiencies relative to L1 before its change.

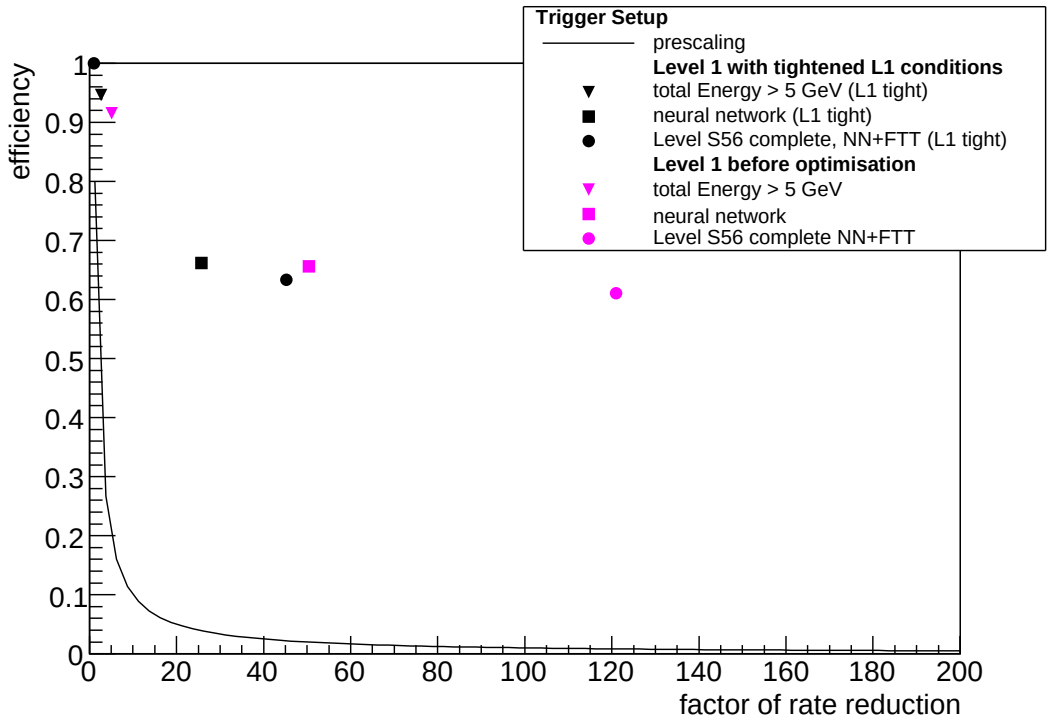


Figure 6.14: Efficiencies of L2 trigger elements plotted against their respective rate reductions with regard to Level 1, which is investigated before its optimisation (light marks) and after the application of additional trigger elements on Level 1 (dark marks, referred to as L1 tight in the legend).

Before the change of the L1 conditions, the rate reductions on the second trigger level were quite high, they amounted to a factor of 50 (NN), 5 (FTT $E_{tot}$) and 120 for the full L2 trigger using both L2 TEs. However, after the change of L1, these values dropped significantly to 25 (NN), 2.5 FTT $E_{tot}$) and to 45 (full trigger), with L2NN still having the largest share in the overall rate reduction of S56 Level 2. The drop in the efficiency after the tightening of Level 1 points to the fact, that the additional rate reduction on Level 1 does not affect the total rate of the trigger, but only the rate of L1. The additional rate reductions and efficiency losses due to the changing of the trigger are compensated at L2, where less events can be thrown away. This is nevertheless an important improvement, as it is desired to reject events at the earliest trigger level possible, because it reduces the deadtime of the detector.

The efficiencies of the respective L2 TEs were again also studied in detail. Fig. 6.15 depicts them in comparison as functions of the $P_T$ of the $D^*$ meson, of the inelasticity and the total transverse energy of the event. The FTT $E_{tot}$ efficiencies are shown as black dots, while the NN TE efficiencies are marked with light markers. The comparison reveals that FTT $E_{tot}$ with an integrated efficiency relative to L1 of $0.812\pm0.005$ performs better than the neural network with an integrated efficiency of $0.570\pm0.004$. However, both trigger elements have their disadvantages. For FTT $E_{tot}$ this is the fact, that the trigger cut at 5 GeV produces a very soft trigger threshold for the efficiency as a function of the total transverse energy. Only for $E_{tot} > 25$ GeV the efficiency becomes flat, but however, never rises to 100%. On the other hand, the NN trigger condition has the problem, that it has

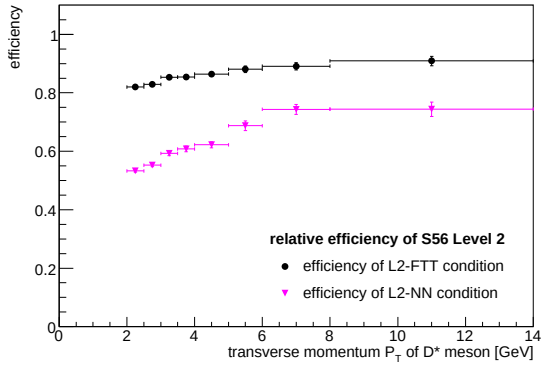


a) as function of the $P_T$ of the $D^*$ meson

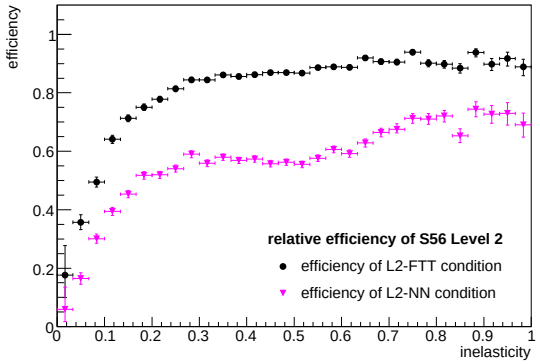


b) as function of inelasticity $y$

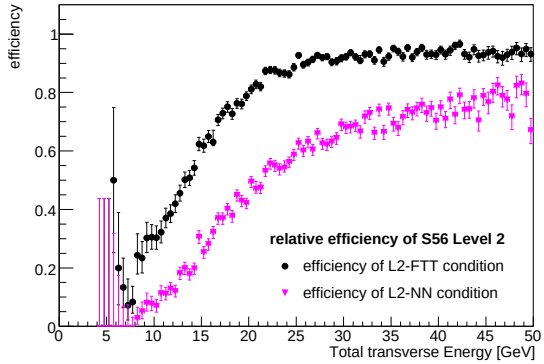


c) as function of total transverse energy

Figure 6.15: Relative efficiencies for the second level of S56 as function of transverse momentum of the $D^*$ meson, inelasticity and total transverse energy. While the FTT $E_{tot}$ TE is depicted as black dots, the NN condition is indicated by light triangles.

a strange dependence on the inelasticity. As can be seen in fig. 6.15 the efficiency rises steadily until $y \approx 0.2$, then it stays more or less constant, maybe with a slight tendency to decline, until at $y \approx 0.6$ it starts to rise again. This is an undesired behaviour for a trigger efficiency as its nature is so far unexplained. An investigation of this dependence was not possible in further detail due to the time limit of this thesis. The behaviour of FTT $E_{tot}$ has been studied in more detail, but the findings of this analysis will be presented later. First, the absolute efficiency of the total S56 subtrigger will be presented.

Fig. 6.16 shows the total absolute efficiency of S56, including its tightened L1 and L2 conditions, as functions of the $P_T$ of the $D^*$ meson, the inelasticity $y$ and total transverse energy of the event. There is no independent photoproduction subtrigger, that could be used as monitor trigger in this analysis, as L2 NN uses e.g. information from LAr. Therefore S61 as well as the set of SpaCal monitor triggers, as defined in table 6.1, are used as monitor trigger. In order to be able to do so, the cut that there should be no scattered electron candidate in the sample, was dropped. S61 (black markers) has the advantage of having more photoproduction related events, as it is not validated on Level 2 with a radius cut of 20 cm as the SpaCal triggers (light markers). Both yield comparable results for the integrated absolute efficiency of S56-L1/L2. These are 0.403±0.004 for SpaCal and 0.412±0.004 for S61 as monitor trigger. The slightly higher integrated efficiency of S61 arises for two different reasons: First of all, S61 does not have a radius cut on its SpaCal TE condition. Thus the S61 trigger can access smaller polar angles $\theta_e$ and thus events, which are closer to untagged photoproduction than the reference sample triggered by SpaCal. Secondly, S61 and S56 are not totally independent, both employ the FTT L1

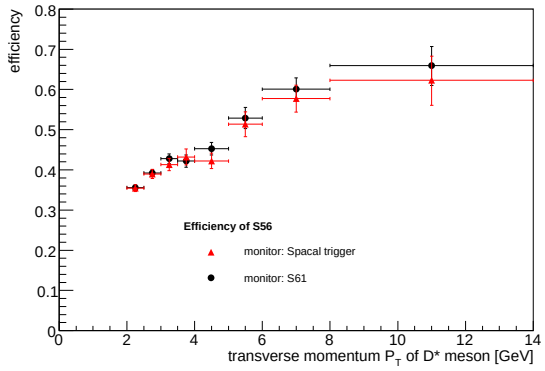


a) as function of the $P_T$ of the $D^*$ meson

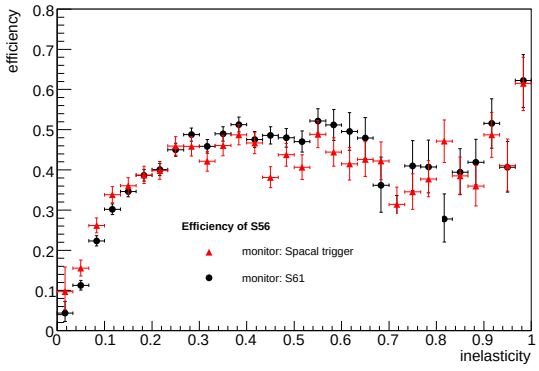


b) as function of inelasticity $y$

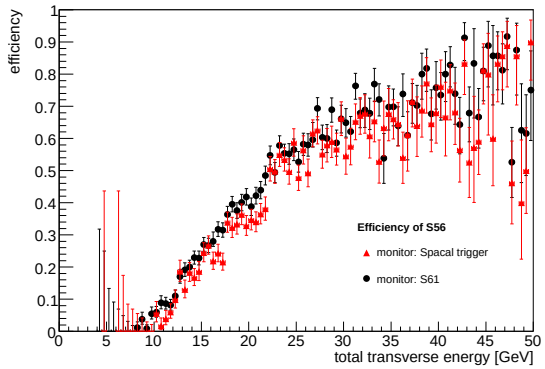


c) as function of total transverse energy

Figure 6.16: Absolute efficiencies for the full subtrigger S56, including all its improved L1 and L2 conditions for different variables. Compared are the efficiencies for two different sets of monitor triggers, S61 marked with black dots and SpaCal triggers as monitors marked with lighter triangles.

trigger condition, that there should be tracks above 900 MeV. Even though, this overlapp is not too significant, taking into account that S56 requires more tracks with a higher $P_T$, it might be the other reason why S56 is more efficient, when using S61 as a monitor trigger. However more important is the fact, that both unwanted features of the L2 TEs are still preserved in the absolute efficiency of the full S56 trigger: There is a strange behaviour for large inelasticities and the trigger thresholds are expand over a large range of $E_{tot}$.

The reason for this, caused by the behaviour of FTT $E_{tot}$ and its unprecise trigger threshold, can however easily be understood. Fig. 6.17 shows the relation between the FTT reconstructed $E_{tot}$ and the offline reconstructed $E_{tot}$ for a sample triggered with S56 and for the same sample with the additional requirement of a $D^*$ meson. First of all, it is quite obvious, that there is a correlation, but nevertheless it is not a 1:1 correlation and it also exhibits huge sidebands. Secondly, when taking a closer look at the $D^*$ meson sample, it becomes clear, that offline, there are indeed no events with a total energy below $E_{tot}$ of 5 GeV. But on the other hand, there are plenty of events with an FTT reconstructed $E_{tot}$ smaller than 5 GeV, but with an offline reconstructed $E_{tot}$ being much larger than 5 GeV, even up to the highest values of $E_{tot}$. Taking into account, that the offline reconstructed $E_{tot}$ is calculated using also energy measurements from the calorimeter, it is not surprising, that the correlation between FTT and offline quantity is not perfect. Nevertheless it was not expected, that the FTT $E_{tot}$ trigger element never reaches full efficiency[3], but reaches

[3]Note that no significant upper cut has been made for the efficiencies shown: The overflows for the histograms used for calculating the efficiency in $E_{tot}$ amount to 87 and 110 for the triggered sample

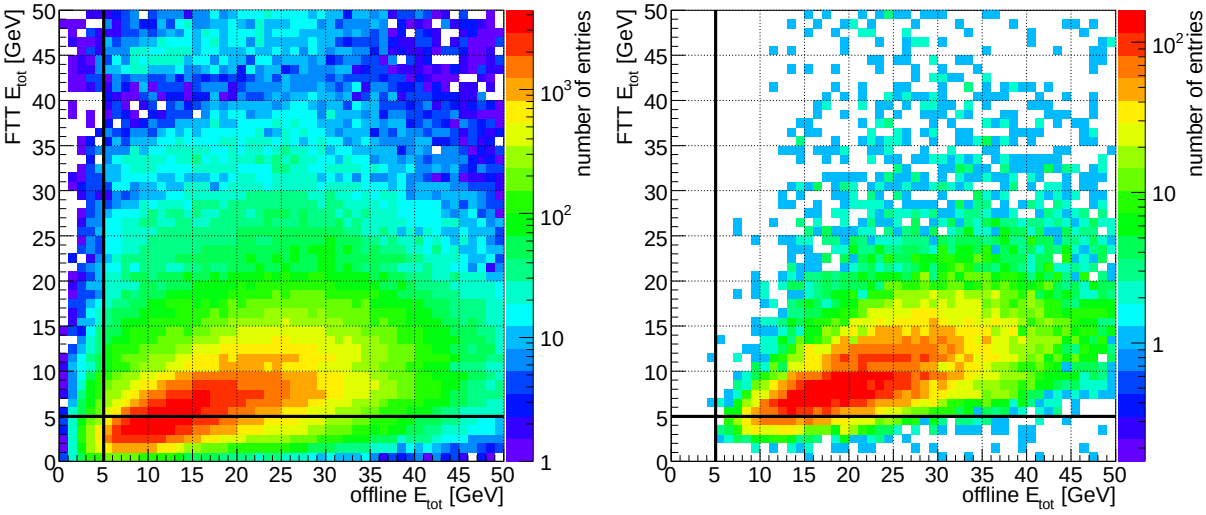


a) S56 triggered sample

b) S56 triggered sample $D^*$ meson sample

Figure 6.17: The correlation between the FTT reconstructed $E_{tot}$ and the offline reconstructed $E_{tot}$ shown for a sample triggered with S56 and for the same sample with the additional requirement of a $D^*$ meson. The thick black lines indicate the applied trigger cut at 5 GeV.

only a plateau of ≈92%.

### 6.3.4 Alternative implementations of a photoproduction trigger on Level 2

Because of the disadvantages of the level 2 trigger for the selection of $D^*$ mesons in untagged photoproduction, an investigation was carried out in order to find other possibilities to reduce the rate of an untagged photoproduction trigger on the second trigger level, before reducing it further on Level 3. As the maximum number of tracks that can be counted on Level 2 (not fitted) above 100 MeV using the FTT amounts to 31, possible cuts on the minimum and maximum number of tracks in order to reduce the rates on Level 2 will be explored in the following. Fig. 6.18 shows the correlation between the number of FTT reconstructed tracks and offline reconstructed tracks for an "inclusive" S56 triggered sample (left hand side) and a S56 triggered $D^*$ meson sample (right hand side). The thick black lines indicate, where the number of tracks equals five. The broad band at 32 FTT tracks is explained by the fact, that this is the maximal number of FTT tracks that can be reconstructed above 100 MeV. The correlation between the number of tracks is very good, even though this does not imply, that the same tracks are reconstructed. Below five tracks there are almost no entries for the $D^*$ meson sample, while there are quite some few for the sample triggered by S56. The situation is different for high FTT multiplicities (above 30 FTT tracks), their fraction overall tends to rise when comparing the S56 triggered and the $D^*$ meson sample.

Indeed, when plotting the efficiency against the rate reduction for conditions using the FTT multiplicity, there is not much gained. Fig. 6.19 shows the efficiencies and rate reduction for various FTT L2 trigger elements in comparison to the "tight" S56 on level

and the reference sample respectively. Thus they are of no importance for the discussion of the performance of the FTT $E_{tot}$ TE.

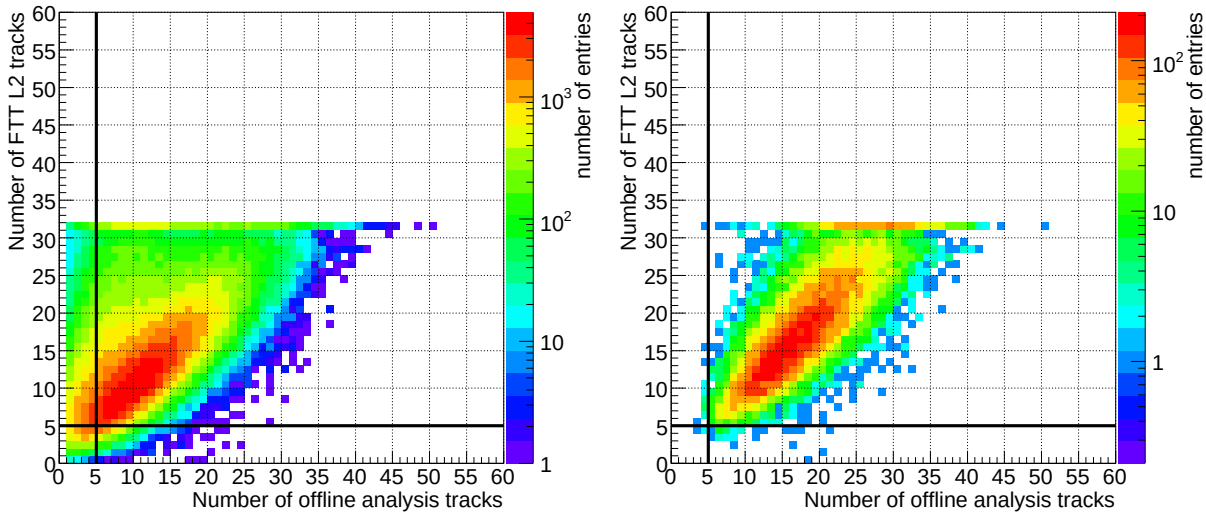


a) S56 triggered sample

b) S56 triggered sample $D^*$ meson sample

Figure 6.18: The correlation between the number of FTT reconstructed track and offline reconstructed tracks having passed the analysis cuts, specified in tab. 5.1, shown for a S56 triggered sample (left hand side) and a $D^*$ meson sample (right hand side). The thick black lines indicate, where the number of tracks equals five.

1. Additionally to conditions on the multiplicities of all tracks above 100 MeV, also the consequences of requiring at least two tracks above 800 MeV and of requiring the multiplicity conditions, at least two tracks above 800 MeV and at least one track above 1500 MeV are depicted. It can be seen, that the multiplicity requirements do not contribute much to the rate reductions, neither the upper nor the lower cut achieve significant rate reductions. However it has to be taken into account, that the L2/L4 transparent runs, with which these estimations were obtained were not taken at the beginning of a lumi fill, where data taking suffers mostly from background events, characterised by high multiplicities. Therefore it might be possible, that there is actually a higher rate reduction of the upper multiplicity cut at the beginning of a fill. However, the requirement of tracks above $P_T$ thresholds might be a good chance to achieve rate reductions needed on level 2. The fact, that the validation of the FTT-L1 trigger conditions might be usefull in case of S56 in order to reduce the rates on level 2 further, show the enhanced accuracy of level 2 in comparison to level 1. It would be indeed interesting to carry out a comparative study of FTT level 1 and level 2 independently of the physics process in order to quantify differences and in order to be able to judge the need to validate on level 2 for certain trigger setups.

Fig. 6.20 shows for the trigger elements discussed above also their efficiencies as functions of several variables, including the $P_T$ of the $D^*$ meson and of the highest momentum track in the event, the number of central tracks, the inelasticity and the total transverse energy. Compared are a trigger condition requiring at least 5 FTT tracks (black dots), another with an upper cut at 31 FTT tracks (lighter triangles) and a third condition requiring at least two tracks above 800 MeV (yellow triangles upside down). A fourth trigger setup is shown, using the former three conditions plus at least one track above 1500 MeV (magenta squares). It can be seen, that the cut on the upper multiplicity very

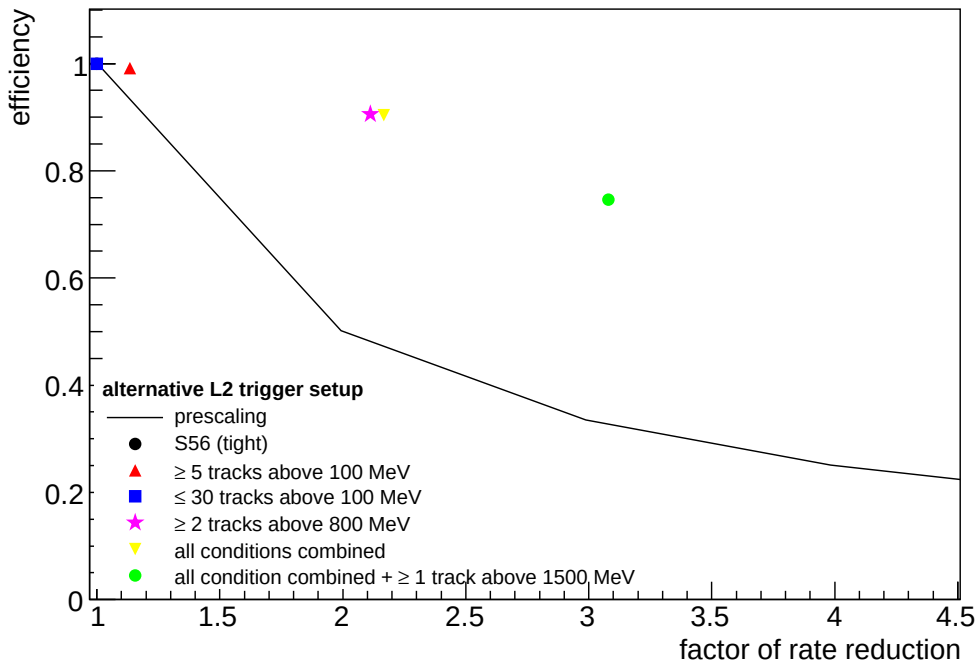


Figure 6.19: Efficiencies of alternative L2 trigger elements plotted against their respective rate reductions with regard to Level 1. The line marks the prescale. The circle, marking the original S56 setup, cannot be seen as it is hidden under the rectangle marking the trigger condition with an upper cut on the multiplicity.

much affects higher values of $y$ as well as high transverse energies. The lower multiplicity cut on the contrary affects the lower $y$ region. The combined effect of these two conditions can be seen in the fourth trigger setup, whose efficiency as a function of the inelasticity shows a similar behaviour to the L2 NN trigger. When comparing the upper and lower multiplicity cuts with the TEs requiring tracks above higher $P_T$ thresholds, it seems, that there is more to gain with a validation of FTT L1 trigger elements on level 2 instead of cutting on multiplicities. In addition, the multiplicity trigger conditions tend to cut out high $P_T$ events. Even though, these events do not contribute to the unexplored regions of low $x_g^{obs}$, one still wants to keep them, in order to be able to cover a large range of $P_T$ in analysis. Therefore it is better to use a trigger with a low efficiency for low $P_T$ events and one with a high efficiency for high $P_T$ events, as the later occur only very rarely due to the $\frac{1}{P_T^4}$ dependence of the $P_T$ distribution [93]. Moreover, the efficiency as function of the total energy of an event has a lower threshold than the FTT $E_tot$ condition. However, as there are only moderate rate reductions achievable on Level 2 without L2NN there is still the need to select $D^*$ mesons online with the help of the FTT L3 systems. This will be described in the next section.

## 6.4 Online selection of $D^*$ mesons using FTT Level 3

Another alternative to the online selection of $D^*$ mesons with the help of L2 NN and FTT $E_{tot}$, would be to use the third level of the FTT in order to reconstruct $D^0$ and $D^*$ mesons online from the FTT-L2 tracks. The information on the invariant masses of the particles can then provide a basis for an online trigger decision. FTT Level 3 is currently in the commission phase. In the following the capability of L3 to select $D^*$ mesons online will be analysed. First of all, an overview of the reconstruction method is given, followed by a short description of the implemented algorithm. Then the L3 performance is analysed considering the track finding efficiency, the resolution of the tracks used in the algorithm and the resolutions of the invariant masses. This section is ended with estimations of the rate reductions and the efficiencies that can be obtained using L3.

### 6.4.1 Online reconstruction of the $D^*$ meson

As already described in the introduction, the $D^*$ meson is reconstructed via its decay $D^{*\pm} \rightarrow D^0\pi^{\pm}_{slow} \rightarrow K^{\mp}\pi^{\pm}\pi^{\pm}_{slow}$. The reconstruction algorithm will be described briefly in the following.

When reconstructing a $D^*$ meson, a loop over all measured tracks is performed, be it offline reconstructed or be it FTT reconstructed tracks on level 3. The first track with $P_T$ >250 MeV is assumed to be a kaon originating from a $D^*$ meson decay. This requirement along with the other cuts is listed in table 6.7 as implemented in level 3 and in table 6.2 as used for offline $D^*$ meson analysis. When a possible kaon candidate is found in the first loop, a pion candidate is searched for in a second loop. When a track is found having the minimal $P_T$ >250 MeV required for a pion candidate and having its charge opposite to the kaon, the scalar sum of their transverse momenta is calculated[4] . In case the sum exceeds a lower limit of 1.5 GeV, the four-vectors of the two tracks are calculated with the respective particle mass assumptions and added. If the invariant mass of this

[4] $|\vec{P}_T| = |\vec{P}_T^1| + |\vec{P}_T^2|$

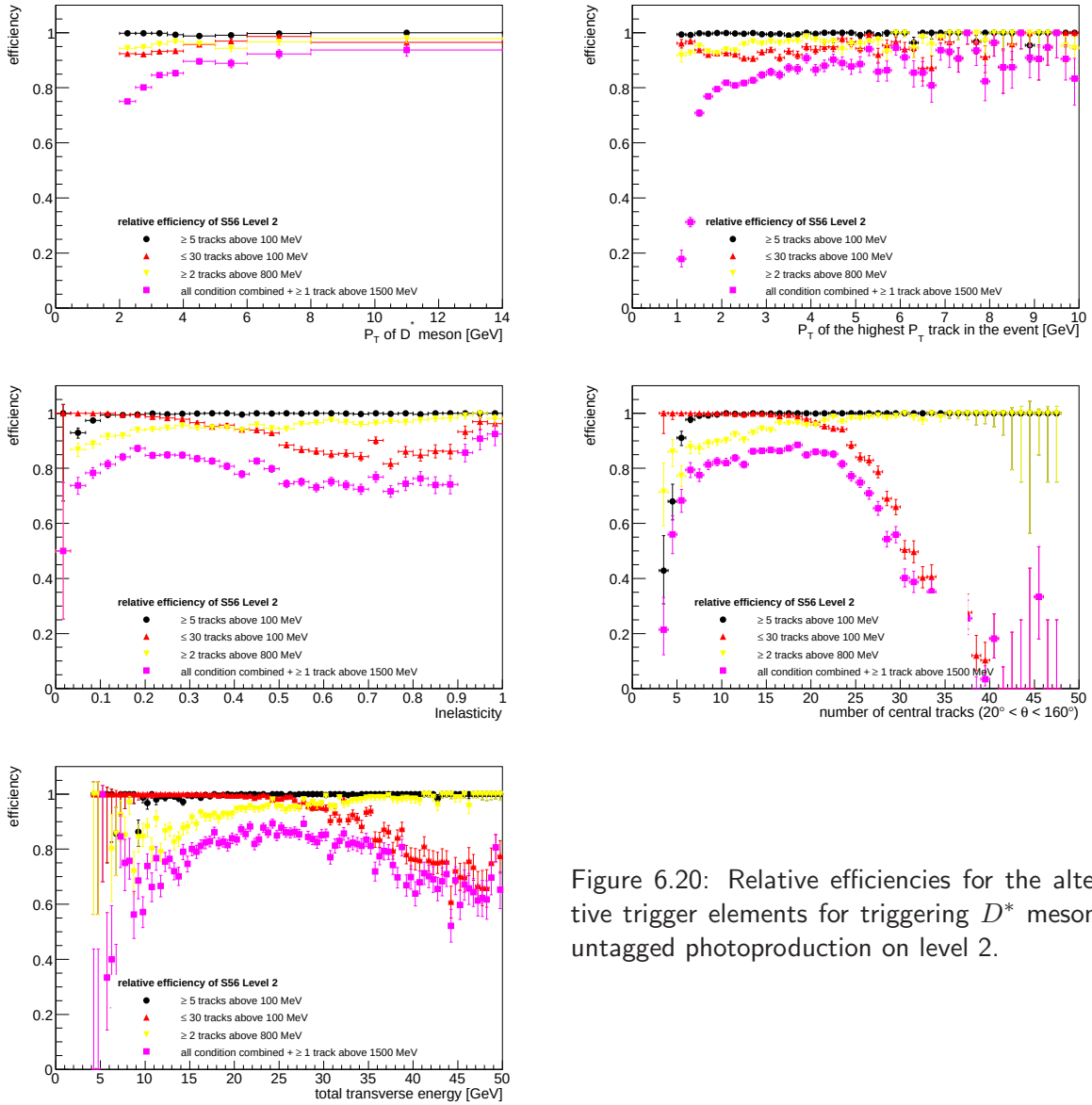


Figure 6.20: Relative efficiencies for the alternative trigger elements for triggering $D^*$ mesons in untagged photoproduction on level 2.

| Variable | Cut |
|---|---|
| **$D^0$ reconstruction** | |
| Transverse momentum of the first track (Kaon) | $P_T^{Kaon} > 0.25$ GeV |
| Transverse momentum of the second track (Pion) | $P_T^{Pion} > 0.25$ GeV |
| charge of second track (Pion) | opposite sign to first track |
| Mass of the $D^0$ meson | $\lvert m_{D^0}^{rec} - m_{D^0}^{nominal} \rvert < 0.25$ GeV |
| Scalar sum of $P_T$ (Kaon and Pion) | $P_T^{Kaon} + P_T^{Pion} > 1.5$ GeV |
| **$D^*$ reconstruction** | |
| Transverse momentum of the third track (slow Pion) | $P_T^{slowPion} > 0.1$ GeV |
| charge of third track (slow Pion) | opposite sign to first track |
| Transverse momentum ($D^*$ meson) | $P_T^{D^*} > 1.5$ GeV |
| Difference of $m(K\pi\pi_{slow}) - m(K\pi)$ | $\Delta M < 0.18$ GeV |

Table 6.7: Cuts currently applied during the online reconstruction of the $D^*$ meson on level 3.

two-track-system is found to be lying within a certain window around the nominal mass of the $D^0$ meson, it is henceforth assumed to be a $D^0$ meson. In a third loop a search for a candidate for a slow pion is started. If a track with the same charge as the already found pion and with a transverse momentum higher than the lower limit of $P_T$ >100 MeV is found, the four-vector of this track is calculated, using the pion mass assumption, and added to the four-vector of the already reconstructed $D^0$ meson candidate. In case the $P_T$ of this three-track-system[5] is larger than the minimal $P_T$ >1.5 GeV required for a $D^*$ meson candidate, the difference $\Delta$M of the invariant masses of $D^*$ and $D^0$ meson candidate is calculated. In case it is smaller than $\Delta M < 0.18$ GeV, the three tracks are likely to be due to a $D^*$ meson decay. In case of L3, the fullfillment of these conditions would trigger a L3 KEEP signal, while in case of an offline physics analysis, this $D^*$ meson candidate would be included in the analysis sample.

There is however still an important difference between the offline reconstruction algorithm and the code that is used online: In order to optimise the algorithm in speed, it was tried to avoid time consuming calculations like the calculation of square roots. Therefore the L3 finder algorithm does not calculate the actual invariant masses, but rather uses derived squared quantaties, which should yield the same results. The explicit formulas and their derivation are given in [70].

### 6.4.2 Level 3: Resolution of invariant masses

When using the L2 tracks in order to calculate invariant masses for triggering purposes, it is important to be aware of the intrinsic resolution power of the system for the respective invariant mass. Therefore, for each offline reconstructed $D^*$ meson a FTT $D^*$ meson was reconstructed from the corresponding FTT L2 tracks. This was done with the help of the track matching procedure, described in sec. 5.1.1, with the only difference that track matches were only searched for the decay particles of the $D^*$ meson. Then a loose cut on the maximal distance parameter $\mathcal{D}$ was applied in order to use only FTT tracks, which can be associated with the respective track of the decay particle with a probability, that is not too small. This procedure allows to reduce the influence of random combinations. The FTT tracks were combined to a $D^0$ meson under kaon and pion mass hypothesis, and with the addition of a slow pion track to a $D^*$ meson.

The differences of the offline and FTT reconstructed $D^0$ mass and $\Delta$M value were calculated and fitted. The double gaussian fit yields a resolution of $\sigma_{D^0 mass}$ =146±5 MeV (see fig. 6.21) for an offline reconstructed $D^0$ meson candidate with a mass within 80 MeV around the nominal $D^0$ mass. The modified Gaussian fit delivers a resolution of $\sigma_{D^0 mass}$=135±1 MeV. For an offline reconstructed $\Delta$M value lying in the primary peak region of 0.143 < $\Delta$M< 0.148 GeV/c$^2$ the double Gaussian fit yields a resolution of $\sigma_{\Delta M}$ =9.1±8 MeV (see fig. 6.22), the modified Gaussian gives a resolution of $\sigma_{\Delta M}$ =9.1±0.2 MeV. The resolution of the transverse momentum of the $D^*$ meson amounts to $\sigma_{P_T^{D^*}}$ =3.8±0.1% (double Gaussian) and $\sigma_{P_T^{D^*}}$ =3.2±0.02% (modified Gaussian) (see fig. 6.23). All these resolutions are again obtained relative to the offline resolution, which is dominated by detector effects and thus correlated with the FTT resolution. This could already be observed in section 5.2.2, when comparing theoretical predictions and mea-

[5] $|\vec{P}_T| = |\vec{P}_T^1 + \vec{P}_T^2 + \vec{P}_T^3|$

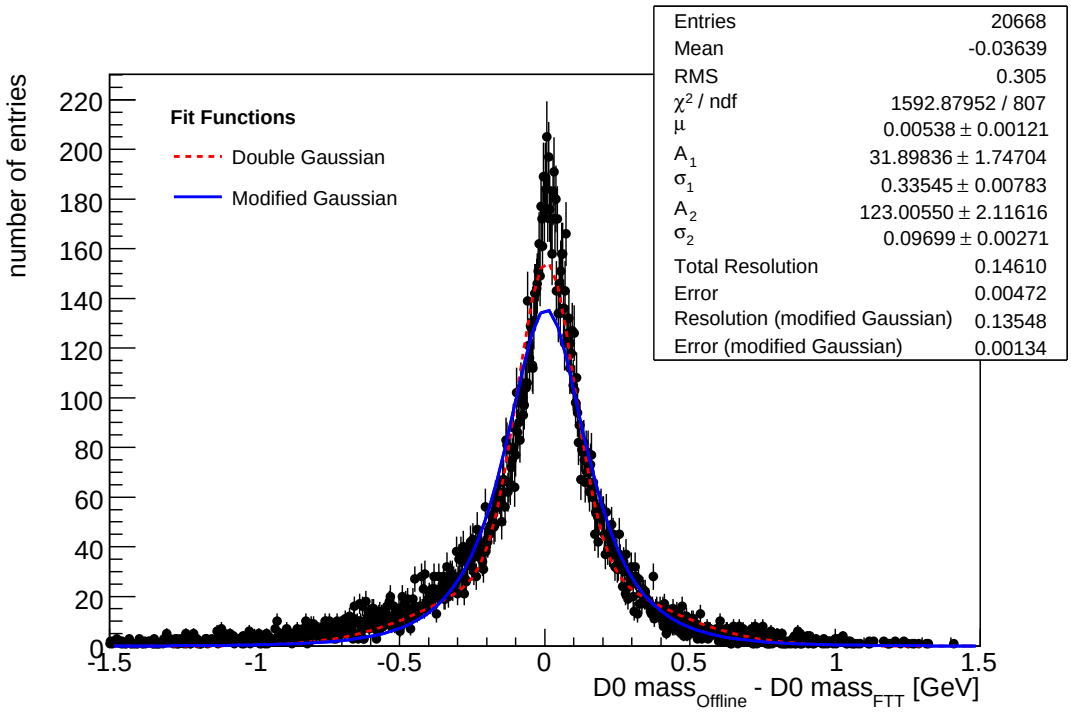


Figure 6.21: The resolution of the L3 system, when reconstructing the $D^0$ mass from L2 tracks.

sured FTT resolutions. The resolutions of the H1 detector for the invariant masses were determined to be $\sigma_{D^0 mass}$ =27.7±2.7 MeV and $\sigma_{\Delta M}$ =8.5±0.7 MeV [29].

What is also striking is the asymmetry of the ΔM distribution, which arises from the fact, that there is the upper cut $\Delta M_{FTT}$ <180 MeV and that the ΔM distribution is per construction limited to values above the nominal pion mass. However, there is also a tail on the left hand side of the ΔM distribution, which arises from tracks, that actually do not correspond to the offline tracks that were used in order to reconstruct the $D^*$ meson. These FTT tracks were matched anyway to the offline tracks of the $D^*$ meson, because there were obviously no other, better fitting tracks found. This is already an indication that apart from the resolution of the invariant mass, the single track finding efficiency might impose limitations to the efficiency of the FTT as well.

### 6.4.3 Rate reductions and efficiencies

In order to estimate the rate reductions and efficiencies feasible with FTT L3, the online code used on the Power-PCs was run offline on FTT Level 2 tracks. Beforehand it was checked, that this FTT simulation and the online L3 finder bit delivered the very same results, which was true for two independent samples, which differed from one another in the run period covered and in the exact implementation of the code.

Fig. 6.24 shows the expectations for rate reductions and efficiencies with various cuts of the invariant masses which varied from one to four $\sigma$. Also varied were the $P_T$ cuts on the particles, being $P_T^{\pi,Kaon}$ >250 MeV, $P_T^{D^*}$ >1.5 GeV, $P_T^{Kaon}$+$P_T^{\pi}$ >1.5 GeV for the

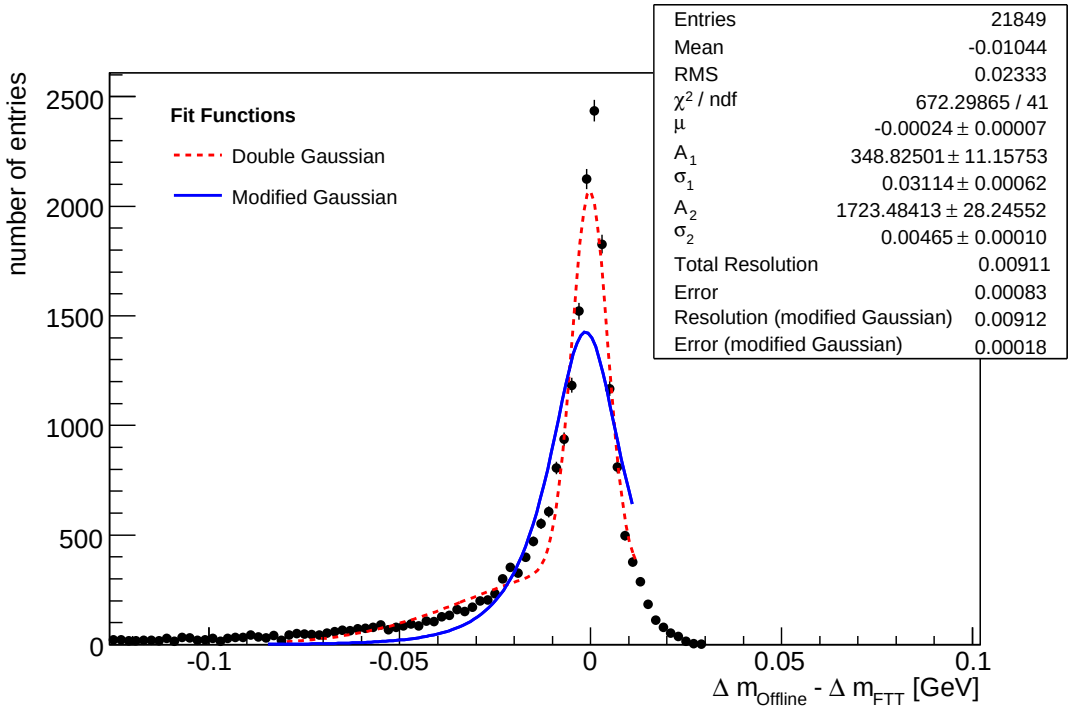


Figure 6.22: The resolution of the L3 system, when reconstructing the $\Delta$M distribution from L2 tracks.

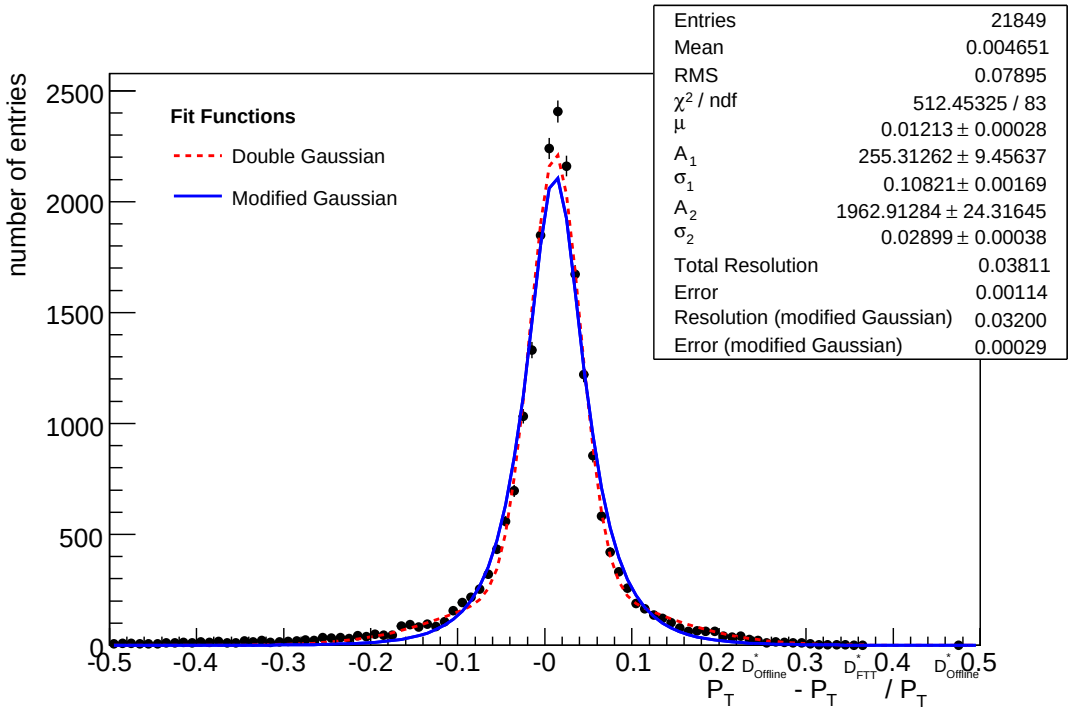


Figure 6.23: The resolution of the L3 system in reconstructing the $P_T$ of a $D^*$ meson from L2 tracks.

| Variable | harsh cut scenario | wide cut scenario |
|---|---|---|
| **$D^0$ reconstruction** | | |
| $P_T^{Kaon}$ | $> 0.45$ GeV | $> 0.4$ GeV |
| $P_T^{Pion}$ | $> 0.25$ GeV | $> 0.25$ GeV |
| $\lvert m_{D^0}^{rec} - m_{D^0}^{nominal} \rvert$ | $< 0.14$ GeV | $< 0.25$ GeV |
| $P_T^{Kaon} + P_T^{Pion}$ | $> 1.75$ GeV | $> 1.5$ GeV |
| **$D^*$ reconstruction** | | |
| $P_T^{slowPion}$ | $> 0.1$ GeV | $> 0.1$ GeV |
| $P_T^{D^*}$ | $> 1.75$ GeV | $> 1.5$ GeV |
| $\Delta M$ | $< 0.18$ GeV | $< 0.25$ GeV |

Table 6.8: Cuts currently applied for the variated cut scenarios for the L3 finder on level 3.

upper plot and $P_T^{\pi}$ >250 MeV, $P_T^{Kaon}$ >400 MeV, $P_T^{D^*}$ >1.75 GeV, $P_T^{Kaon}$+$P_T^{\pi}$ >1.75 GeV for the lower plot. The latter $P_T$ cuts fall still within a region of three $\sigma$ of the respective resolutions, determined earlier for the $P_T$ of the $D^*$ meson and for FTT tracks in general. The light markers show rate reductions and efficiencies for the cuts on the $D^0$ meson only ($D^0$ finder), while the darker markers show efficiencies and rate reductions including the cuts on the slow pion, the $D^*$ meson and $\Delta$M ($D^*$ finder). The rate reduction was determined relative to L1 using L2/L4 transparent runs. The rate reductions span from a factor of 1 ($D^0$ finders) to almost 30 (cut within $3\sigma$ for the $P_T$s, but only $1\sigma$ for the invariant masses). However, these rate reductions are of course accompanied by losses in efficiencies as one would expect when cutting on standard deviations. The currently implemented finder algorithm is not depicted in this picture, its rate reduction can be estimated based on the data of fig. 6.24a to be around 12 with an efficiency of approximately 60%.

Fig. 6.25 shows the relative efficiencies for FTT Level 3 for three scenarios: Besides the currently implemented cuts there were also two implementations tested, where the cuts for some of the parameters were set to approximately one and three $\sigma$ of the resolutions determined in the preceeding sections, some of the cuts however were not varied because, like the cut on slow pion for instance, they were already at the threshold. The actual values of the former two scenarios are summarised in table 6.8, those for the current L3 implementation can be found in table 6.7.

The result of these efficiency studies is shown in fig. 6.25, where the efficiencies for the different cut scenarios are plotted as function of $P_T$ of the $D^*$ mesons, the number of central tracks and of the offline determined $\Delta M$ mass. Their total relative efficiencies amount to 0.707±0.006 for the wide cut scenario, 0.366±0.003 for the harsh cut scenario and 0.616± 0.006 for the online finder currently implemented. When looking at their efficiencies as function of $P_T$ of the $D^*$ meson and of the multiplicity of an event, it becomes evident, that there is still a certain fraction of events, that are triggered accidentally. This is reflected in the steady rise for the efficiencies as function of multiplicity and in the drop in efficiency for the transverse momentum of the $D^*$ meson. Whereas for a rising number of tracks the combinatorial background also increases, it tends to decrease with increasing $P_T$. When a $D^*$ meson possesses a very high $P_T$, it is very unlikely that it

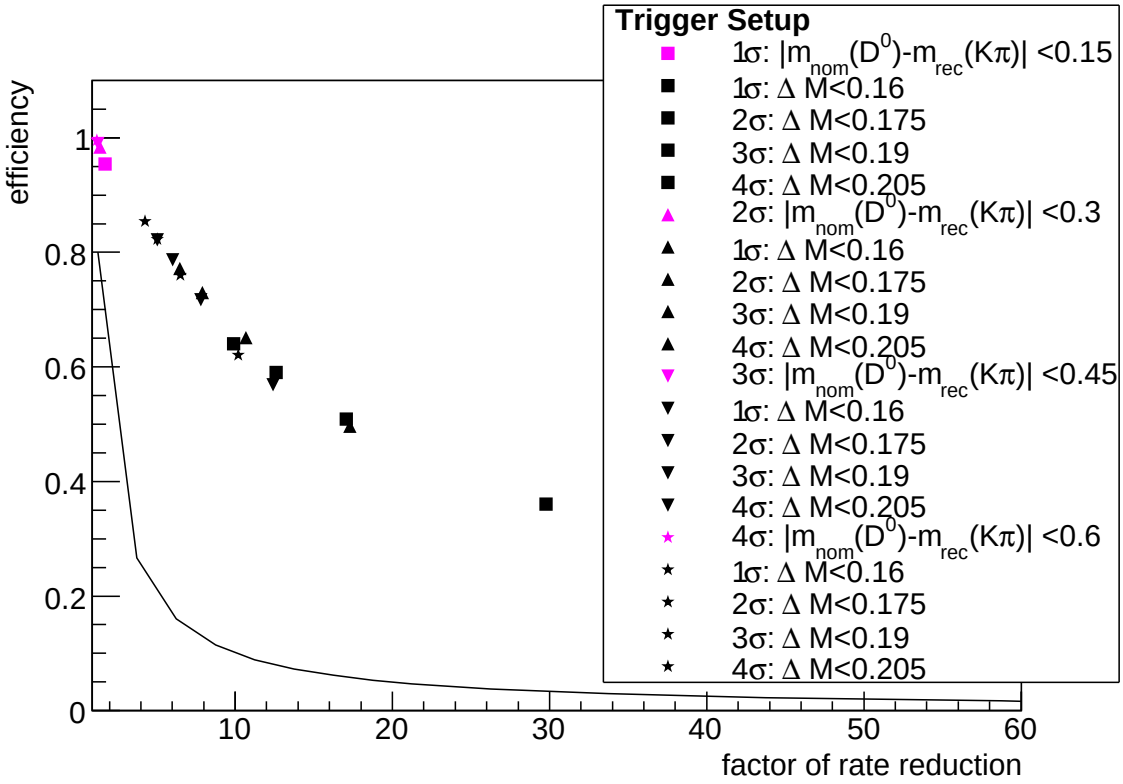


a) $P_T^{\pi,Kaon}$ >250 MeV, $P_T^{D^*}$ >1.5 GeV, $P_T^{Kaon}$+$P_T^{\pi}$ >1.5 GeV
$|m_{nom}(D^0) - m_{rec}(K\pi)|$ denotes the difference between nominal and reconstructed $D^0$ meson mass.

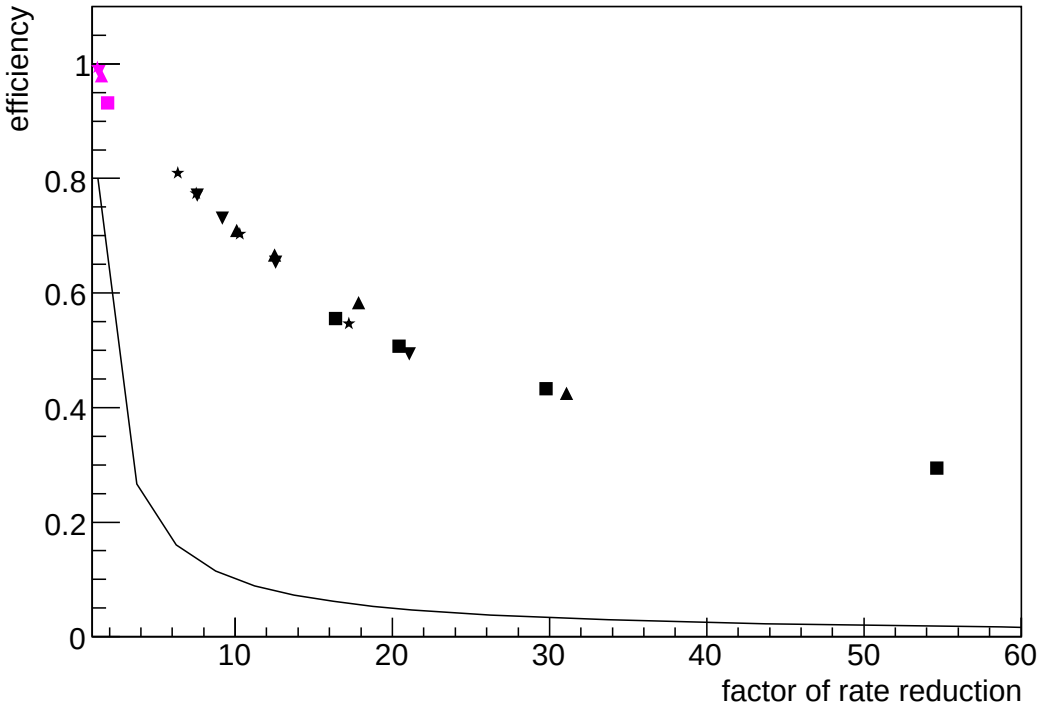


b) $P_T^{\pi}$ >250 MeV, $P_T^{Kaon}$ >400 MeV, $P_T^{D^*}$ >1.75 GeV, $P_T^{Kaon}$+$P_T^{\pi}$ >1.75 GeV

Figure 6.24: Estimated rate reductions for the FTT Level 3 system.

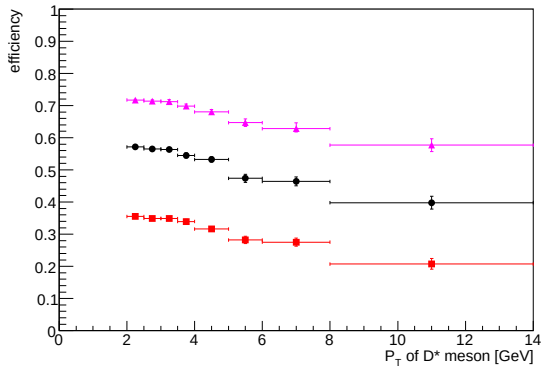


a) as function of the $P_T$ of the $D^*$ meson

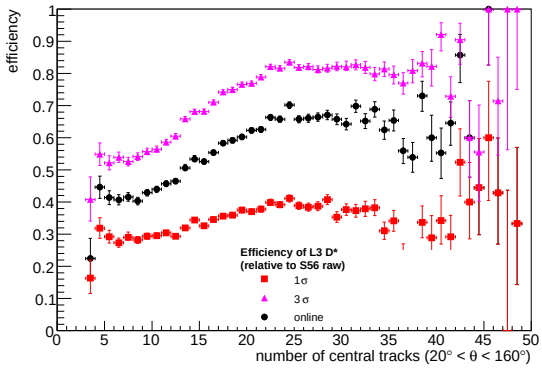


b) as function of the multiplicity

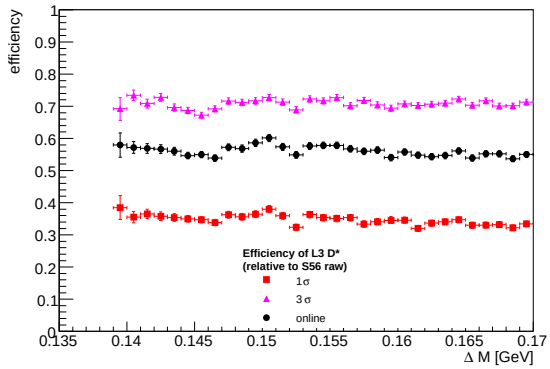


c) as function of ΔM

Figure 6.25: Relative efficiencies of the FTT Level 3 finder with regard to Level 1 S56.

originates from a fragmentation process, in which a large number of further particles were produced. The energy and the transverse momentum that went into the hadronisation process was more or less fully transfered to that high $P_T$ $D^*$ meson [94]. Therefore the $D^*$ meson and its decay particles are more or less isolated, which reduces the number of possible particles that could be used in the reconstruction of the $D^*$ meson instead of the genuine decay particles. There is still most probably another hadronic final states (HFS), which balances the momentum of the $D^*$ meson and its decay particles respectively. But it is quite unlikely, that the FTT L3 finder could accidentally reconstruct a $D^*$ meson candidate out of three of these HFS tracks not at all connected to the $D^*$ meson candidate. Therefore, the probability of reconstructing a $D^*$ meson out of two of its decay particles and a false assigned third track decreases with increasing momentum. On the other hand, L3 uses also cuts on the charges of the particles. Tracks with a $P_T$ above 5 GeV are already quite likely to be assigned a wrong charge during the track finding on L2. This is yet another reason, why the L3 efficiency decreases for high momenta of the $D^*$ meson. The distribution for $\Delta M$ is however flat for all trigger setups, there are no losses in efficiency visible for the distribution on its upper limit of 0.17 GeV. Hence, the $\Delta M$ cut could potentially be tightened.

It is worth noting, that even for the harsh cut scenario, the efficiency rises with the event multiplicity. This tendency is not as pronounced as for the other setups, but it indicates nevertheless, that even in this setup, there is some accidental background collected. However, there is still room for improvements and for the optimisation of both, cuts on the event selection as well as cuts of the L3 finder. Investigations into these problems are

on their way and will contribute to the future FTT L3 trigger [95].

# 7 Summary

After the successful upgrade of HERAII, new detector subsystems at the H1 experiment have successfully been put into operation. In order to make use of the gained yield in luminosity and inclusive *ep* scattering rate, it is crucial to be able to select those events which are of special importance to the physics programme of the H1 collaboration among the occuring total physics and background events. The Fast Track Trigger (FTT), one of the newly commissioned detector components of the H1 experiment, is dedicated to supply the central data aquisitions system with fast signals, based upon which an online selection of events can be carried out.

The FTT uses information from the central jet chambers of the experiment and reconstructs from this information track parameters. It is subdivided into three levels, which deliver signals to the respective first three levels of the four level trigger system of H1. While on the first level the track reconstruction is based on masks, on the second level more precision is gained by carrying out a track fit from more refined mask information. The third level is based on commercial power PCs, on which track finder algorithms are run, which use the level 2 track as well as information from other detector subsystems.

In the scope of this thesis the general performance of the level 2 system was analysed. The resolution of all relevant track parameters, namely $\kappa$, $\phi$ and $\theta$, was determined for data collected in the years 2005 and 2006. Also, the effect of several influences on the resolutions was investigated. The analysed effects are multiple scattering, the number of linked segments and the missing energy loss corrections as influence parameters. The resolutions were found to be of the expected order of magnitude. Furthermore, these resolutions and also other parameters of the FTT L2 system were analysed for each run as function of time. The resolutions were found to have much improved during the run period 2005/06 due to an improved calibration of the drift time and the usage of the nominal z-vertex for each run. With the help of the investigation tools, developed in this thesis, periods of bad FTT performance, e.g. due to the usage of wrong masks, could be excluded from further analyses.

Another part of this thesis covered the online selection of $D^*$ mesons, which are produced in *ep* scattering via boson gluon fusion processes. These processes are sensitive to the gluon densitiy of the proton and thus represent an important possibility to measure the gluon density of the proton. In order to detect the production of $D^*$ mesons in boson gluon fusion or other production channels, its "golden" decay channel ($D^{*\pm} \rightarrow D^0 \pi^{\pm}_{slow} \rightarrow K^{\mp}\pi^{\pm}\pi^{\pm}_{slow}$) was chosen, where three charged particles are detectable in the final state.

The analysis of the performance of trigger mechanism employing FTT track information covered the kinematical regions of both DIS and photoproduction. The DIS subtrigger S61 was analysed and found to be working with a high efficiency on level 1. Possible trigger setups for a second level DIS trigger were investigated in terms of efficiencies and rate

reductions. The photoproduction trigger S56 was examined in terms of rate reductions and efficiencies on the first and second trigger level. A proposal for tightened conditions on the first level is made, that was finally implemented. It was shown, that subtrigger S56 works quite successfully, too, although there might improvements still be possible.

The third trigger level of the FTT was investigated by determining the resolution of the invariant masses of the $D^0$ mesons and the mass difference $\Delta M = m_{D^*} - m_{D^0}$ obtainable with the FTT level 2 tracks. With the start of positron running in 2006, the third trigger level will be fully made use of.

# Bibliography


[1] Dietrich B. Wegener. *Vorlesung Einführung in die Kern- und Elementarteilchenphysik*. Dortmund, Germany: (2002/2003) 5th edition.

[2] F. Halzen and Alan D. Martin. *Quarks and Leptons: An Introductory Course In Modern Particle Physics*. New York, USA: Wiley (1984).

[3] B. Povh, C. Scholz, K. Rith, and F. Zetsche. *Teilchen und Kerne*. Berlin, Germany: Springer (1993).

[4] D. H. Perkins. *Introduction to high energy physics*. Reading 1972.

[5] Murray Gell-Mann. Symmetries of baryons and mesons. *Phys. Rev.*, 125:1067–1084, 1962.

[6] Murray Gell-Mann. A schematic model of baryons and mesons. *Phys. Lett.*, 8:214–215, 1964.

[7] J. D. Bjorken and Emmanuel A. Paschos. Inelastic electron proton and gamma proton scattering, and the structure of the nucleon. *Phys. Rev.*, 185:1975–1982, 1969.

[8] Eidelman, S. and others. Review of Particle Physics. *Physics Letters B*, 592:1+, 2004.

[9] D. H. Perkins. Review of neutrino experiments. In *Stanford 1975, Symposium On Lepton and Photon Interactions At High Energies*, Stanford 1975, 571-603.

[10] C. Adloff et al. Measurement and QCD analysis of neutral and charged current cross sections at HERA. *Eur. Phys. J.*, C30:1–32, 2003.

[11] V. Chekelian. Gluon density and strong coupling from structure functions and measurement of $f_L$. Prepared for Ringberg Workshop on New Trends in HERA Physics 2003, Ringberg Castle, Germany, 28 Sep - 3 Oct 2003.

[12] S. Alekhin et al. HERA and the LHC - A workshop on the implications of HERA for LHC physics: Proceedings Part A and Part B. 2005.

[13] Arafat Gabareen Mokhtar. Recent electroweak measurements from the H1 and ZEUS experiments. 2004.

[14] C. Adloff et al. Measurement of D* meson cross sections at HERA and determination of the gluon density in the proton using NLO QCD. *Nucl. Phys.*, B545:21–44, 1999.

[15] Cathrin Adloff. *Open Charm Production in Deep Inelastic Electron-Proton Scattering with the H1 Detector at HERA*. PhD thesis, Universität Wuppertal, 2001.

[16] Yuri L. Dokshitzer. Calculation of the structure functions for deep inelastic scattering and e+ e- annihilation by perturbation theory in quantum chromodynamics. (in russian). *Sov. Phys. JETP*, 46:641–653, 1977.

[17] Guido Altarelli and G. Parisi. Asymptotic freedom in parton language. *Nucl. Phys.*, B126:298, 1977.

[18] E. A. Kuraev, L. N. Lipatov, and Victor S. Fadin. The pomeranchuk singularity in nonabelian gauge theories. *Sov. Phys. JETP*, 45:199–204, 1977.

[19] I. I. Balitsky and L. N. Lipatov. The pomeranchuk singularity in quantum chromodynamics. *Sov. J. Nucl. Phys.*, 28:822–829, 1978.

[20] Marcello Ciafaloni. Coherence effects in initial jets at small $\frac{Q^2}{s}$. *Nucl. Phys.*, B296:49, 1988.

[21] S. Catani, F. Fiorani, and G. Marchesini. QCD coherence in initial state radiation. *Phys. Lett.*, B234:339, 1990.

[22] Hannes Jung. Qcd and collider physics. Lecture, https://www.desy.de/ jung/qcd_collider_physics_2005/welcome.html, 2005/6.

[23] Katja Krüger. *Photoproduction of J/Ψ Mesons at Medium and Low Elasticities at HERA*. PhD thesis, Universität Hamburg, April 2001.

[24] A. Aktas et al. Elastic J/$\psi$ production at HERA. 2005.

[25] A. Aktas et al. Inclusive production of $D^+$, $D^0$, $D_s^+$ and $D^{*+}$ mesons in deep inelastic scattering at HERA. *Eur. Phys. J.*, C38:447–459, 2005.

[26] A. Aktas et al. Measurement of charm and beauty photoproduction at HERA using $D^*$ $\mu$ correlations. *Phys. Lett.*, B621:56–71, 2005.

[27] Sebastian Schmidt. *Messung charminduzierter Zweijetereignisse in tief-inelastischer ep-Streuung mit dem H1-Detektor bei HERA*. PhD thesis, Technische Universität München, August 2004. DESY-THESIS-2004/043.

[28] Jeannine Wagner. *Charm and Beauty Production at HERA with $D^*$-Muon Events*. PhD thesis, Universität Hamburg, 2004. DESY-THESIS-2004-022.

[29] Gero Flucke. *Photoproduction of $D^*$ Mesons and $D^*$ Mesons associated with Jets at HERA*. PhD thesis, Universität Hamburg, March 2005. DESY-THESIS-2005/06.

[30] Adrian Perieanu. *The Structure of Charm Jets and the Dead Cone Effect in Deep-Inelastic Scattering at HERA*. PhD thesis, Universität Hamburg, January 2006. DESY-THESIS-2006-002.

[31] A. Aktas et al. Search for a narrow baryonic resonance decaying to K0(s) p or K0(s) anti-p in deep inelastic scattering at HERA. hep-ex/0604056, 2006.

[32] Florian Bechtel. Cross Section Measurements of $D^*$ Production in the Decay Channel $D^* \to K\pi\pi\pi$ and Search for a Charmed Pentaquark with the H1 Detector at HERA. Diploma thesis, Humboldt Universität zu Berlin, August 2005.

[33] Marc-Oliver Bönig. *$D^*$ Mesons in Deep Inelastic Scattering*. PhD thesis, Universität Dortmund, in preparation.

[34] Klaus Urban. *$D^*$ Mesons in Photoproduction*. PhD thesis, Ruprecht-Karls-Universität Heidelberg, in preparation.

[35] I. Abt et al. The H1 detector at HERA. *Nucl. Instrum. Meth.*, A386:310–347, 1997.

[36] I. Abt et al. The tracking, calorimeter and muon detectors of the H1 experiment at HERA. *Nucl. Instrum. Meth.*, A386:348–396, 1997.

[37] B. List. The H1 silicon tracker. *Nucl. Instrum. Meth.*, A549:33–36, 2005.

[38] H. Henschel and R. Lahmann. The backward silicon tracker of the H1 Experiment at HERA. *Nucl. Instrum. Meth.*, A453:93–97, 2000.

[39] W. Braunschweig. A forward silicon tracker for H1. DESY PRC 99-01, 1999.

[40] D. Pitzl et al. The H1 silicon vertex detector. *Nucl. Instrum. Meth.*, A454:334–349, 2000.

[41] M. Urban, J. Becker, S. Schmitt, and U. Straumann. The CIP2k first-level trigger system at the H1 Experiment at HERA. *IEEE Trans. Nucl. Sci.*, 50:903–908, 2003.

[42] Max Christoph Urban. *The new CIP2k z-vertex trigger for the H1 experiment at HERA*. PhD thesis, Universität Zürich, 2004. DESY-THESIS-2004-044.

[43] C. Niebuhr. Aging in the central jet chamber of the H1 Experiment. *Nucl. Instrum. Meth.*, A515:43–49, 2003.

[44] T. Nicholls et al. Performance of an electromagnetic lead / scintillating fiber calorimeter for the H1 Detector. *Nucl. Instrum. Meth.*, A374:149–156, 1996.

[45] R. D. Appuhn et al. H1 backward upgrade with a SpaCal calorimeter: The hadronic section. DESY-96-013.

[46] B. Andrieu et al. The H1 liquid argon calorimeter system. *Nucl. Instrum. Meth.*, A336:460–498, 1993.

[47] Christoph Wissing. Bestimmung der Charakteristika des Flugzeitsystems des H1-Detektors zur Messung des Strahluntergrundes – Triggerstudien für eine Messung der Protonstrukturfunktion $F_2$ bei H1. Diploma thesis, Universität Dortmund, March 1998.

[48] Armen Beglarian et al. Proposal for an upgrade of the H1-TOF system. not published.

[49] H1 Collaboration. Contributed paper to the 28th International Conference on High Energy Physics, Warsaw, Poland. Paper pa17-026, July 1996.

[50] T. Ahmed et al. Experimental study of hard photon radiation processes at HERA. *Z. Phys.*, C66:529–542, 1995.

[51] Katja Krüger. Der neue e-Tagger des H1 Experimentes. Vortrag bei Science@KIP, 19.1.2006.

[52] M. Fleischer et al. Performance and upgrade of H1 calorimeters: LAr calorimeter, SpaCal and VLQ. Includes three talks given at 7th International Conference on Calorimetry in High-Energy Physics (ICCHEP 97), Tucson, AZ, 9-14 Nov 1997 (See also DESY-98-005A, B, and C).

[53] R. D. Appuhn et al. Hadronic response and e/$\pi$ separation with the H1 lead/fibre calorimeter. *Nucl. Instrum. Meth.*, A382:395–412, 1996.

[54] Christoph Wissing. *Entwicklung eines Simulationsprogramms und Implementierung schneller Spurfitalgorithmen für den neuen H1-Driftkammertrigger*. PhD thesis, Universität Dortmund, February 2003.

[55] Andreas Jung. Inbetriebnahme der dritten Stufe des schnellen Spurtriggers für das H1-Experiment. Diploma thesis, Universität Dortmund, September 2004.

[56] Jens Zimmermann. *Statistical Learning in High Energy and Astrophysics*. PhD thesis, Ludwig-Maximilians-Universität München, June 2005.

[57] J. K. Kohne et al. Realization of a second level neural network trigger for the H1 Experiment at HERA. *Nucl. Instrum. Meth.*, A389:128–133, 1997.

[58] A. Baird et al. A fast track trigger for the H1 Collaboration. *Nucl. Instrum. Meth.*, A461:461–464, 2001.

[59] A. Baird et al. A fast high resolution track trigger for the H1 Experiment. *IEEE Trans. Nucl. Sci.*, 48:1276–1285, 2001.

[60] A. Schoning. A fast track trigger for the H1 Collaboration. *Nucl. Instrum. Meth.*, A518:542–543, 2004.

[61] J.-C. Bizot et al. Strategy studies for the H1 topological L2-trigger (l2TT). H1 internal note, H1-IN-508(01/1997), January 1997.

[62] Marie Jacquet. The steering of the H1 Level 2 Topological Trigger. H1 internal note, H1-IN-519(06/1997), June 1997.

[63] H. C. Schultz-Coulon, E. Elsen, T. Nicholls, J. Coughlan, and H. Rick. A general scheme for optimization of trigger rates in an experiment with limited bandwidth. *IEEE Trans. Nucl. Sci.*, 46:915–919, 1999.

[64] H1 Central Trigger group. Trigger strategy definition. internal web ressource, https://www-h1.desy.de/h1/iww/itrigger/TrigSetup/strategy.in, 2006.

[65] Olaf Behrendt. Entwicklung von Algorithmen zur Identifikation von Vektormeson-Ereignissen mit dem neuen H1-Spurtrigger. Diploma thesis, Universität Dortmund, March 2002.

[66] Martin zur Nedden, Burkard Reisert, and Thomas Schörner. H1 liquid argon trigger: Overview, simulation and performance. H1 internal note, H1-IN-592(04/2001), July 2001.

[67] Dirk Hoffmann. *Zwei-Elektron-Ereignisse im H1-Detektor*. PhD thesis, Universität Hamburg, July 2000.

[68] Thomas Krämerkämper. *Messung der Gluondichte im Photon und Entwicklung eines neuronalen Triggers*. PhD thesis, Universität Dortmund, January 1998.

[69] H1 Neural Network group. Definition of NN-L2 trigger elements. H1 internal web ressource, June 2006.

[70] Jürgen Naumann. *Entwicklung und Test der dritten H1-Triggerstufe*. PhD thesis, Universität Dortmund, 2003.

[71] Veikko Karimaki. Fast code to fit circular arcs. HU-SEFT-1991-10.

[72] H1 Fast Track Trigger group. Definition of FTT-L1 trigger elements. H1 internal web ressource, June 2006.

[73] H1 Fast Track Trigger group. Definition of FTT-L2 trigger elements. H1 internal web ressource, June 2006.

[74] H1 Fast Track Trigger group. Definition of FTT-L3 trigger elements. H1 internal web ressource, June 2006.

[75] H1 Collaboration. Addendum to the proposal "a fast track trigger with high resolution for h1". H1 internal ressource, H1-09/99-576, September 1999.

[76] Rene Bruns. Root class documentation. Online Class Index for ROOT, July 2006.

[77] S. Chekanov et al. Measurement of charm fragmentation ratios and fractions in photoproduction at HERA. *Eur. Phys. J.*, C44:351–366, 2005.

[78] S. Chekanov et al. Measurement of $D^{*+}$-production in deep inelastic $e^+$-p scattering at HERA. *Phys. Rev.*, D69:012004, 2004.

[79] Gerhard Bohm and Günter Zech. *Einführung in Statistik und Messwertanalyse für Physiker*. Verlag Deutsches Elektron Synchrotron, 2005.

[80] R. K. Bock and A. Vasilescu. *The particle detector briefbook*. Springer, 1998.

[81] R. L. Gluckstern. Uncertainties in track momentum and direction, due to multiple scattering and measurement errors. *Nucl. Instrum. Meth.*, 24:381–389, 1963.

[82] Dirk Dodt. Analysis of the data quality of the FTT. Diploma thesis, Universität Dortmund, March 2005.

[83] Marc Paterno. Calculating efficiencies and their uncertainties. Online document, http://home.fnal.gov/ paterno/probability/localresources.html, May 2003.

[84] J. Stiewe. HERA (and non-HERA) kinematics for pedestrians. Version 1.13, Ruprecht-Karls-Universität Heidelberg, 2004.

[85] Jozef Ferencei. SpaCal status based on SPACKIN tapes 587->613 (8.7.->12.7.2005). private communication, 2005.

[86] Kristin Lohwasser. Trigger studies. Talk at the Heavy Flavour Meeting, H1 internal web ressource, 13/09 2005.

[87] Martin Wessels. Heavy flavour triggers. Talk at the H1 Trigger Meeting, H1 internal web ressource, 14/02 2006.

[88] Martin Wessels. Trigger rates/new triggers. Talk at the H1 Trigger, Data Quality and Tracking Meeting, H1 internal web ressource, 25/05 2006.

[89] H1 Central Trigger group. Trigger rate plots. H1 internal web ressource, https://www-h1.desy.de/h1/iww/itrigger/TrigRates/, May 2006.

[90] Andreas Meyer. Subtrigger s56. private communication, March 2006.

[91] Andreas Meyer. Heavy flavour triggers. Talk at the H1 Trigger Meeting, H1 internal web ressource, 05/04 2006.

[92] Kristin Lohwasser. Triggering D*s in untagged gp. Talk at the H1 Trigger Meeting, H1 internal web ressource, 05/04 2006.

[93] W. M. Geist, D. Drijard, A. Putzer, R. Sosnowski, and D. Wegener. Hadronic production of particles at large transverse momentum: Its relevance to hadron structure, parton fragmentation and scattering. *Phys. Rept.*, 197:263–374, 1990.

[94] H. Albrecht et al. Production and decay of the charged D* mesons in e+ e- annihilation at 10-GeV center-of-mass energy. *Phys. Lett.*, B150:235, 1985.

[95] Daniel Beneckenstein. FTT Level 3 performance (in preparation). Diploma thesis, Ruprecht-Karls-Universität Heidelberg, 2007.

# Acknowledgements – Danksagung

Hiermit möchte ich in meiner Muttersprache all jenen danken, die zum Gelingen dieser Arbeit auf die eine oder andere Weise beigetragen haben:

Allen voran natürlich Herrn Prof. Dr. Dietrich Wegener, der mir die Gelegenheit gegeben hat, in der sehr konstruktiven Arbeitsatmosphäre eines internationalen Forschungszentrums meine Diplomarbeit schreiben zu können (und stets bereit war, auszutesten, *wie* schreckhaft ich eigentlich wirklich bin – sehr schreckhaft). Außerdem möchte ich mich herzlich für die Vermittlung meiner anschließenden Doktorarbeit und die immense Unterstützung bei den dafür erforderlichen Bewerbungsverfahren bedanken. Genereller Dank für Ihre Gastfreundschaft geht an Herrn und Frau Wegener!

Herrn Prof. Dr. Bernhard Spaan danke ich für seine Bereitschaft, die Rolle des Zweitgutachters zu übernehmen und die Gastfreundschaft, die er und seine Arbeitsgruppe mir bei meinen Besuchen am Lehrstuhl E5 in Dortmund erwiesen haben. Dankeschön an Eva, Matthias, Enrico, Armin, Heiko, Jesko, Mirco, Magnus und Klaus. Vielen Dank auch an Frau Lorenz und Frau Schwertfeger, die stets hilfsbereit und freundlich waren!

Ein gesondertes und spezielles Dankeschön geht an die Dortmund-Heidelberg Arbeitsgruppe am DESY: 1000 Dank für Geduld und Spucke und fürs Beruhigen. Im Einzelnen: Christoph und Andy, die mir beim Zumüllen unserer drei Schreibtische behilflich waren, und mir ansonsten stets mit Rat und Tat bei Computerproblemen (Christoph) oder beim Vernichten von Schokolade (Andy) beistanden. Danke auch an die diversen anderen Bewohner unseres Büros für gute Laune und Unterstützung: Dirk (Scrubs), Jörg (auch immer am Quasseln), Moritz (Klettern), Daniel (Ruhe und Gelassenheit), Menkse (kein Champagner), Herrn Prof. Dr. Stiewe (Bildung) und Filip (Eishockey und Babyfotos). Außerdem noch Stephan (fürs Lernen, ernsthaft!), Victor (krimmige Tipps) und Herrn Prof. Dr. Schultz-Coulon (immer gut gelaunt, eine echte Aufmunterung).

Ein riesengroßer Dank geht an Frau Doktor Katja Krüger, die mit geschultem Auge Unstimmigkeiten in Plots sofort aufdecken kann, ungefähr alles über Heavy Quarks und H1 weiß und immer eine Idee parat hat, was man noch ausprobieren könnte. Für ihre kompetente Betreuung möchte ich auch Marc-Oliver Bönig und Olaf Behrendt danke (ich verspreche, ich werde NOCH mehr Beruhigungstechniken erlernen und praktizieren). Außerdem danke ich den anderen aus ihrem Büro: Michael (aus Kasachstan), Andrea (aus Mexiko, gegen die wir im nächsten WM-Finale spielen werden!!!! Ich freue mich auf mein erstes E5-Wasserbomben-Festival zu deinen Ehren!), und last but not least Klaus (-Peter).

Herzlichen Dank auch an die assoziierten Schweizer für Tipps, Tricks und Kaffee: André Schöning (FTTMASTER2006), Benno List, Nick, Ronny, Tobias, Volker, Michel und Lea. Plus an die Physics&Cookies-Gruppe: Hannes Jung (danke für alles!), Lluis, Zlatka, Axel, Tobias. Andreas Meyer für Motivation.

Plus an die offsite-Aktivisten für die nötige Ablenkung: Franziska, Daniela (klein&gross), Lena (ebenfalls klein&gross), Nancy, Tania (in Hamburg) und fernmündlich Nadine, Sonja, Jana, Nicola, Chris, Wiebke&Tobias, Rita&Andreas, Ingo (schwarz&rot). Plus alle, die ich vergessen habe (ihr seid immer eingeladen, wohin es mich auch verschlägt).

Vielen Dank an meine Eltern und Großeltern, die mich all die Jahre unterstützt haben. Sowie an Björn, mein Bruderherz!

Diese Arbeit wurde mit Mitteln des Bundesministeriums für Bildung & Forschung unter der Projektnummer 05 H1 4PEA /6 gefördert.